

**RELIABILITY-LIMITING DEFECTS IN GaN/AlGaN HIGH ELECTRON MOBILITY
TRANSISTORS**

By

Tania Roy

Dissertation

Submitted to the Faculty of the
Graduate School of Vanderbilt University
in partial fulfillment of the requirements

for the degree of

DOCTOR OF PHILOSOPHY

in

Electrical Engineering

December, 2011

Nashville, Tennessee

Approved:

Professor Daniel M. Fleetwood

Professor Ronald D. Schrimpf

Professor Sokrates T. Pantelides

Professor Norman H. Tolk

Professor Robert A. Reed

Report Documentation Page				Form Approved OMB No. 0704-0188	
Public reporting burden for the collection of information is estimated to average 1 hour per response, including the time for reviewing instructions, searching existing data sources, gathering and maintaining the data needed, and completing and reviewing the collection of information. Send comments regarding this burden estimate or any other aspect of this collection of information, including suggestions for reducing this burden, to Washington Headquarters Services, Directorate for Information Operations and Reports, 1215 Jefferson Davis Highway, Suite 1204, Arlington VA 22202-4302. Respondents should be aware that notwithstanding any other provision of law, no person shall be subject to a penalty for failing to comply with a collection of information if it does not display a currently valid OMB control number.					
1. REPORT DATE DEC 2011		2. REPORT TYPE		3. DATES COVERED 00-00-2011 to 00-00-2011	
4. TITLE AND SUBTITLE Reliability-Limiting Defects in GaN/AlGaN High Electron Mobility Transistors				5a. CONTRACT NUMBER	
				5b. GRANT NUMBER	
				5c. PROGRAM ELEMENT NUMBER	
6. AUTHOR(S)				5d. PROJECT NUMBER	
				5e. TASK NUMBER	
				5f. WORK UNIT NUMBER	
7. PERFORMING ORGANIZATION NAME(S) AND ADDRESS(ES) Vanderbilt University, Department Electrical Engineering, Nashville, TN, 37240				8. PERFORMING ORGANIZATION REPORT NUMBER	
9. SPONSORING/MONITORING AGENCY NAME(S) AND ADDRESS(ES)				10. SPONSOR/MONITOR'S ACRONYM(S)	
				11. SPONSOR/MONITOR'S REPORT NUMBER(S)	
12. DISTRIBUTION/AVAILABILITY STATEMENT Approved for public release; distribution unlimited					
13. SUPPLEMENTARY NOTES					
14. ABSTRACT					
15. SUBJECT TERMS					
16. SECURITY CLASSIFICATION OF:			17. LIMITATION OF ABSTRACT Same as Report (SAR)	18. NUMBER OF PAGES 111	19a. NAME OF RESPONSIBLE PERSON
a. REPORT unclassified	b. ABSTRACT unclassified	c. THIS PAGE unclassified			

ACKNOWLEDGEMENTS

I would like to thank Professor Daniel M. Fleetwood, for allowing me to work on the project on GaN. He has always supported me, and helped me out of troublesome situations. Long hours in the lab when experimental results were difficult to obtain would have been more painful without the positive outlook and appreciation for hard work of Prof. Fleetwood.

I am extremely grateful to Professor Ronald D. Schrimpf, for teaching me device physics, and for all the guidance he has provided during my stay at Vanderbilt. His calm demeanor, his incisive understanding of devices has always inspired me during my work. He has been extremely patient with me, and spent hours before submission deadlines to help me analyze experimental results.

I would like to thank Professor Sokrates T. Pantelides, for agreeing to serve on my committee, for being extremely helpful throughout my PhD work. Without the calculations done by his group, this thesis would lose half its worth. I thank Professor Robert Reed for being on my committee. Professor Norman Tolk's class on Condensed Matter Physics has been crucial in helping me develop concepts of device physics.

I thank the Office of Naval Research for financially supporting this work through DRIFT MURI grant N-00014-08-100655. I am extremely thankful to our collaborators at University of California, Santa Barbara, for providing us with the GaN HEMTs, without which this work could not have been performed.

The contributions of Dr. Yevgeniy Puzyrev and Dr. En Xia Zhang deserve special mention in the thesis. Yevgeniy has tirelessly performed DFT calculations for all the defects in GaN that have been mentioned in this work. He has always been excited to find theoretical results to explain the experiments I have performed. Without his help, my work would be incomplete. I can never thank En Xia enough, for being my friend, my advisor in all situations of life. From giving me driving lessons in late evenings, to teaching me how to use lab equipment, and bonding devices for noise experiments, she has always been there to help me out. She has stood by me during any trouble I had, and shared with me her experiences in her research life to help me make decisions. Without En Xia, graduate life would have been extremely difficult. I thank Dr. Xiao Shen for his DFT calculations and insightful discussions to complete the understanding of noise in GaN HEMTs.

I am thankful to Jonathan Felbinger and Professor Lester F. Eastman for hosting us at Cornell University, and allowing us to do the RF measurements on GaN HEMTs. The week at their laboratory had been extremely fruitful in terms of helping me understand GaN device physics better.

I would like to thank all my friends at Radiation Effects and Reliability group at Vanderbilt University, for making the slow life of a graduate student look less arduous. Ashley and Cher have always made me look forward to being in the Characterization lab. David, despite his unending complaints, has always been warm and generous, reminding me of people from home. I would like to thank Lakshmi, Srikanth, Vishwa, Farah, Nihaar, Jugantor, Indranil, Elizabeth, Jon, Sarah, Nelson, Mike, Pierre and Nadia, and all other members of RER who were always there to talk to in between and outside research. These long years in graduate school would have been frustrating had I not had Sandeepan, Aritra and Gaurav to share all complaints and anxieties with.

I owe this work to my parents and RM for having shelved the little luxuries for later, for all the unslept nights, for embracing the ennui of workplace just so that I could attend one of the best universities in India. I owe this work, and much more, to troubled times, laughable loves, impressionist's palettes, surreal words, Calcutta's cobblestones, Durga pujas which went missed year after year, coffee cups to measure life, intellectualism on bookshelves – mostly unread, liquid nitrogen and blisters, babbling brooks flowing by roads, Christmas snow and high fever, almost drowning in deep green waters when PhD never existed, Prnbs for seasoning it all.

TABLE OF CONTENTS

	Page
ACKNOWLEDGEMENTS	ii
LIST OF FIGURES	vi
1. INTRODUCTION	1
1.1 Reliability issues for GaN HEMTs	1
1.2 Overview of dissertation	2
2. BACKGROUND	5
2.1 Growth techniques for GaN HEMTs	5
2.2 Summary	16
3. DC AND AC CHARACTERISTICS OF GaN HEMTs	17
3.1 Introduction	17
3.2 DC and AC characteristics of GaN HEMTs used in the thesis	17
3.3 Summary	25
4. HOT ELECTRON-INDUCED DEGRADATION IN GaN HEMTs	26
4.1 Introduction	26
4.2 Experiments	27
4.3 Threshold voltage and peak g_m shifts after stress	27
4.3 Point defects responsible for $V_{pinch-off}$ shift	30
4.4 Conclusion	34
5. RF STRESS INDUCED DEGRADATION IN GaN HEMTs	35
5.1 Experiments	35
5.2 DC and small signal performance	35
5.3 DC vs. RF transconductance degradation	42
5.4 Large signal performance	44
5.5 Conclusions	46
6. LOW FREQUENCY $1/f$ NOISE AT ROOM TEMPERATURE	47
6.1 Introduction	47
6.2 Experiments	47
6.3 Gate voltage dependence of S_{vd}	48
6.4 S_{vd} vs. gate leakage	50
6.5 S_{vd} vs. frequency	52
6.6 Point defects responsible for $1/f$ noise	53
6.7 Conclusion	56
7. NOISE SPECTROSCOPY ON GaN HEMTs	57
7.1 Introduction	57
7.2 Experiments	58
7.3 Temperature-dependence and microscopic origin of pre-stress $1/f$ noise	58

7.4 Noise spectroscopy under low current conditions	66
7.6 Conclusions.....	75
8. PROTON-INDUCED DEGRADATION IN GaN HEMTs	77
8.1 Introduction.....	77
8.2 Experimental results.....	77
8.3 Discussion	85
8.4 Summary and Conclusions	88
9. CONCLUSIONS.....	90
REFERENCES	94

LIST OF FIGURES

Figure	Page
2.1. Typical GaN/AlGaIn HEMT structure.....	5
2.2. Schematic diagram of metal organic chemical vapor deposition (MOCVD) growth.	7
2.3. Schematic illustration of molecular beam epitaxy (MBE) growth.	12
3.1. Epitaxial structure of HEMTs.....	17
3.2. (a) I_D - V_D and (b) I_D - V_G and I_G - V_G curves for a Ga-rich HEMT.....	18
3.3.(a) I_D - V_D and (b) I_D - V_G and I_G - V_G curves for a N-rich HEMT.	19
3.4.(a) I_D - V_D and (b) I_D - V_G and I_G - V_G curves for an NH ₃ -rich HEMT.	20
3.5. Comparison of DC transconductance with transconductance at 10 GHz for (a) Ga-rich, (b) N-rich, and (c) NH ₃ -rich HEMTs.....	21
3.6. f_T and f_{MAX} vs. V_G for a Ga-rich device.....	22
3.7. f_T and f_{MAX} vs. V_G for a N-rich device.	22
3.8. f_T and f_{MAX} vs. V_G for an NH ₃ -rich device.	23
3.9. Load-pull measurements showing large signal performance of (a) Ga-rich, (b) N-rich and (c) NH ₃ -rich HEMTs when operated as class AB power amplifiers.	24
4.1 g_m - V_{GS} for the (a) Ga-rich, (b) N-rich, and (c) NH ₃ -rich samples at $V_D = 2$ V, before and after stress for 8 hours. Ga-rich device: $V_{pinch-off} = -5.1$ V, $V_{g\ stress} = -4$ V. N-rich device: $V_{pinch-off} = -4.1$ V, $V_{g\ stress} = -3.6$ V, NH ₃ -rich device: $V_{pinch-off} = -5$ V, $V_{g\ stress} = -4$ V. $V_{g\ stress}$ values were chosen such that power dissipation during stress was the same in all three cases, keeping thermal effects the same in all three sample types. [45]	28
4.2. Change in pinch-off voltage as a function of stress time, for MBE-grown GaN HEMTs. [45].....	29
4.3. Change in pinch-off voltage as a function of stress time for MOCVD-grown GaN HEMTs. [46]	29
4.4. Formation energy of hydrogenated Ga-vacancies in bulk GaN. [46]	30
4.5. Formation energy of hydrogenated Ga-vacancies in Al _{0.3} Ga _{0.7} N. [47]	31

4.6. Formation energy of hydrogenated N-anti-sites in GaN bulk. [46].....	31
4.7. Formation energy of hydrogenated N-anti-sites in $\text{Al}_{0.3}\text{Ga}_{0.7}\text{N}$. [47]	32
4.8. Energy band diagram showing E_c and E_f in the AlGa N barrier and the Ga N bulk during stress conditions. [47]	33
5.1. I_D - V_D curves for a Ga-rich HEMT, before and after RF stress.	36
5.2. I_G - V_G curves for a Ga-rich HEMT, before and after RF stress.	36
5.3. I_D - V_G curves for a Ga-rich HEMT, before and after RF stress.	37
5.4. f_T and f_{MAX} for a Ga-rich device.	37
5.5. I_D - V_D curves for a N-rich HEMT, before and after RF stress.	38
5.6. I_D - V_G curves for a N-rich HEMT, before and after RF stress.	38
5.7. I_G - V_G curves for a N-rich HEMT, before and after RF stress.	39
5.8. f_T and f_{MAX} for a N-rich device.	39
5.9. I_D - V_D curves for an NH_3 -rich HEMT, before and after RF stress.	40
5.10. I_D - V_G curves for an NH_3 -rich HEMT, before and after RF stress.	40
5.11. I_G - V_G curves for an NH_3 -rich HEMT, before and after RF stress.	41
5.12. f_T and f_{MAX} for an NH_3 -rich device.	41
5.13. g_m drop-off before and after RF stress for Ga-rich device.	42
5.14. g_m drop-off before and after RF stress for N-rich device.	43
5.15. g_m drop-off before and after RF stress for NH_3 -rich device.	43
5.16. Load-pull measurement results on Ga-rich HEMT before and after stress.	44
5.17. Load-pull measurement results on N-rich HEMT before and after stress.	45
5.18. Load-pull measurement results on NH_3 -rich HEMT before and after stress.	45
6.1 Cross-section of a Ga N HEMT, showing the gated and ungated portion of the channel.	48
6.2. Gate voltage dependence of excess drain voltage low frequency noise in Ga N HEMTs.	

The noise originates from the channel. [47]	49
6.3. S_{vd} vs. leakage current for Ga-rich, N-rich, and NH_3 -rich devices before stress. [47]	50
6.4. S_{vd} vs. leakage current for Ga-rich, N-rich, and NH_3 -rich devices after stress. [47]	50
6.5. Excess drain-voltage low-frequency noise-power spectral density as a function of gate leakage, after stress. The increase in noise with increasing leakage current shows that traps formed in AlGa N barrier are responsible for the noise. [47]	51
6.6. Post-stress vs. pre-stress noise for Ga-rich, N-rich, and NH_3 -rich devices, $f = 10$ Hz. Noise measurements are performed at $V_G - V_{\text{off}} = 0.2$ V, $V_{DS} = 0.02$ V.	52
6.7. S_{vd} vs. frequency for (a) Ga-rich, (b) N-rich, and (c) and (d) NH_3 -rich HEMTs. [47]	53
6.8. Formation energy of hydrogenated Ga-N-divacancies in (a) Ga N and (b) $\text{Al}_{0.3}\text{Ga}_{0.7}\text{N}$. [47]	54
6.9. Formation energy of substitutional carbon in N-site as a function of Fermi energy in AlGa N . The dashed line shows the position of the Fermi level in the AlGa N barrier during the stress and during noise measurement. [57]	55
7.1. Temperature dependence of the I_D - V_G curves for a Ga-rich MBE-grown HEMT. [63]	59
7.2. S_{vd} vs. f for a N-rich MBE-grown HEMT. [63]	59
7.3. Frequency exponent of noise power spectral density as a function of temperature for N-rich MBE-grown devices. [63]	60
7.4. Frequency exponent of noise power spectral density as a function of temperature for Ga-rich MBE-grown devices. [63]	61
7.5. Frequency exponent of noise power spectral density as a function of temperature for MOCVD-grown devices.[63]	61
Fig. 7.6. Scattering rate of an electron is dominated by an emission of the optical phonon from a typical defect in a Ga N crystal. The scattering rates correspond to phonon frequency of $f=360$ meV and $f=425$ meV for singly and doubly hydrogenated Ga vacancy (V_{Ga}) respectively. [66]	63
7.7. Noise vs. temperature for N-rich and Ga-rich MBE and MOCVD-grown devices. $f = 10$ Hz. [63]	64
7.8. Defect energy of substitutional O in AlGa N as a function of the distance from the ideal lattice site, showing the existence of a DX configuration. Black squares represent transition points between the charge states of O_N during the electron emission. The dashed line shows	

that the energy barrier to emit one electron from a negatively charged O DX center is ~ 0.25 eV. The inset schematically illustrates the capture of one electron by the positively charged oxygen O_N^{+1} , which involves thermally excited tunneling (red arrow) of an electron from GaN Fermi level to the empty level of O_N^{+1} defect in AlGaIn. The energy level drops significantly in energy upon capture of two electrons. [63]	65
7.9. Calculated and experimental γ , and noise power spectral density as a function of temperature for (a) Ga-rich MBE-grown, (b) N-rich MBE-grown, and (c) MOCVD-grown devices. $f = 10$ Hz.	67
7.10. Noise vs. temperature for Ga-rich, N-rich and MOCVD-grown samples. Noise was measured for Ga-rich and N-rich MBE-grown devices at $V_G - V_{off} = 0.1$ V, $V_D = 0.02$ V, and for MOCVD-grown device at $V_G - V_{off} = 0.1$ V, $V_D = 0.05$ V.	68
7.11. Noise as a function of temperature for two Ga-rich MBE-grown devices; $f = 10$ Hz. Noise decreases after stress. Noise is measured at $V_G - V_{off} = 0.1$ V, and for (a) $V_D = 0.05$ V, for (b) $V_D = 0.02$ V.	69
7.12. Comparison of calculated and observed values of frequency exponent γ of $1/f^\gamma$ noise, as a function of temperature for two different Ga-rich MBE-grown devices.	70
7.13. Noise before and after stress as a function of temperature for an MOCVD-grown device; $f = 10$ Hz. After stress $\Delta V_{pinch-off} = -0.1$ V. Noise is measured at $V_G - V_{off} = 0.1$ V, $V_D = 0.05$ V.	71
7.14. γ vs. T , (a) before stress, and (b) after stress, for a MOCVD-grown device. Both experimental and calculated values are shown.	72
7.15. Noise before and after stress as a function of temperature for an NH_3 -rich MBE-grown device; $f = 10$ Hz. After stress $\Delta V_{pinch-off} = -1.1$ V. The noise is measured at $V_G - V_{off} = 0.1$ V, $V_D = 0.05$ V.	72
7.16. γ vs. T , (a) before stress, and (b) after stress, for NH_3 -rich MBE-grown device. Both experimental and calculated values are shown.	73
7.17. Noise before and after stress as a function of temperature for an N-rich MBE-grown device; $f = 10$ Hz. After stress $\Delta V_{pinch-off} = -0.3$ V. The noise is measured at $V_G - V_{off} = 1.8$ V, $V_D = 0.15$ V.	74
7.18. γ vs. T , (a) before stress, and (b) after stress, for a N-rich MBE-grown device. Both experimental and calculated values are shown.	74
8.1. $I_D - V_G$ curves for devices grown using (a) Ga-rich, (b) N-rich MBE, and (c) MOCVD, before and after irradiation. The transfer characteristics after annealing for several weeks at room temperature are also shown in (a) for the Ga-rich devices. [64]	78

8.2. I_G - V_G curves for devices grown using (a) Ga-rich MBE, (b) N-rich MBE, and (c) MOCVD, before and after irradiation.[64].....	79
Fig. 8.3. (a) $\Delta V_{pinch-off}$ is shown as a function of 1.8 MeV proton fluence for devices grown by MBE under N-, Ga-rich, and NH_3 -rich conditions, and by MOCVD. Device to device variation in pinch-off voltage shift as a function of proton fluence for devices grown by (b) Ga-rich MBE, and (c) MOCVD. [73]	80
8.4. S_{vd} vs. frequency before and after irradiation for (a) Ga-rich MBE, (b) N-rich MBE, and (c) MOCVD-grown devices. [62]	81
8.5. Gate voltage dependence of S_{vd} before and after irradiation for (a) Ga-rich, (b) N-rich, and (c) MOCVD-grown devices. [64]	82
8.6. (a) S_{vd} vs f , and (b) $S_{vd}/V_d^2 \times f/T$ vs. T for a Ga-rich MBE device before and after 1.8 MeV proton irradiation; the fluence is $1 \times 10^{14} \text{ cm}^{-2}$. [73]	84
8.7. $S_{vd}/V_d^2 \times f/T$ vs. T for a N-rich MOCVD device before and after 1.8 MeV proton irradiation; the fluence is $1 \times 10^{14} \text{ cm}^{-2}$. [73]	84
8.8. Formation energy of (a) Ga-N divacancies and (b) N vacancies as a function of the position of the Fermi level in the band gap of $Al_{0.3}Ga_{0.7}N$. [64]	86

CHAPTER 1

INTRODUCTION

GaN-based high electron mobility transistors (HEMTs) have gained popularity in high-frequency, high-power electronics owing to the high breakdown voltage and high mobility of GaN. The reliability of GaN-based devices is still an issue, and a lot of research is under way in order to bring GaN to parity with SiC in high-power application areas. In this work, we study the various reliability issues of GaN/AlGaN HEMTs that were fabricated under different conditions using molecular beam epitaxy (MBE) and metallorganic chemical vapor deposition (MOCVD). We propose physics-based models to predict the reliability of GaN HEMTs, and extrapolate the techniques used to other semiconductor material systems. First, the devices are characterized electrically and then subjected to stress – DC and RF electrical stress and exposure to radiation. The defects that cause stress-induced degradation are identified using density functional theory calculations. The generation rate of these defects are helpful in order to predict the failure rate of these devices during their operation.

1.1 Reliability issues for GaN HEMTs

Despite impressive performance of GaN HEMTs in high power applications, the reliability of these devices impedes their deployment in the field. Hot electron-induced degradation in peak transconductance and saturation current may occur during operation under high electric fields. During operation under high-current conditions, self-heating of these devices dominates, leading to negative output conductance. Self-heating occurs due to the low thermal

conductivity of the substrate on which the devices are grown. Electrical stress may also cause the degradation of RF performance of the devices, by means of degradation in the unity gain frequency, f_T . The power added efficiency (PAE) and the gain of the transistors may also degrade during the long term operation of the HEMTs. Recently, it has been shown that RF stress is more severe than DC stress at the same bias point. At high power levels, RF stress creates new traps and causes an increase in source resistance, whereas DC stress causes drain current degradation under similar conditions [1]. A new degradation mechanism is shown in [2] through step-stressing the devices. The degradation is brought about by crystallographic defect formation due to inverse piezoelectric effects. On the other hand, GaN-based transistors are relatively immune to radiation damage, as opposed to Si-based devices, due to the relatively large band gap of GaN and the reduced probability of current transport via trapping and other defects.

1.2 Overview of dissertation

The PhD thesis examines the major reliability issues in GaN/AlGaIn high electron mobility transistors, and identifies the defects responsible for their degradation. The techniques used in identification of the defects are not restricted to GaN-based systems, and can be used in any semiconductor material.

We subjected HEMTs grown by MOCVD and MBE under Ga-rich, N-rich, and NH_3 -rich conditions to hot electron stress (DC stress, under high field conditions) and found that while Ga-rich and N-rich devices show a positive shift in pinch-off voltage after stress, ammonia-rich MBE-grown and MOCVD-grown devices undergo a negative shift. The dehydrogenation of hydrogenated Ga-vacancies is responsible for the positive shift in pinch-off voltage and the dehydrogenation of hydrogenated N-anti-sites is responsible for the negative shift. Since

MOCVD requires the presence of ammonia, similar defects are seen in NH_3 -rich MBE-grown and MOCVD-grown devices. RF stress performed on Ga-rich, N-rich, and NH_3 -rich MBE-grown devices do not cause a substantial shift in DC or RF characteristics of these devices. The presence of a change in charge state of a defect near the Fermi level in the material accounts for a trap energy level which can contribute to the $1/f$ noise in a device. Ga-vacancies do not show a change in charge state around the Fermi level in GaN or AlGaN. However, N-antisites, Ga-N-divacancies and C substitutional impurities in an N-site show a change in charge state around the Fermi level in GaN and AlGaN, thus serving as defects which contribute to the noise. Low frequency $1/f$ noise measurements across a wide range of temperature give us the energy distribution of the thermally-assisted process causing the noise. We obtain a peak in the energy spectrum at 0.2 eV for all device types, which corresponds to the reconfiguration of an oxygen DX center in AlGaN. A second peak is observed in N-rich MBE-grown devices above 1 eV, which corresponds to the reconfiguration of a nitrogen antisite. While irradiating the devices with 1.8 MeV protons, all device types show a positive shift in pinch-off voltage. Ga-rich devices show a larger shift in pinch-off voltage than N-rich and NH_3 -rich devices. Ga-N-divacancies created by proton-induced displacement damage are defects responsible for the increase in $1/f$ noise after irradiation.

In the remainder of this document, we discuss these findings in detail. Chapter II gives the background of this work, by describing the fabrication processes for the devices used in this study. This is important because we have chosen four different kinds of devices for our study, based on their processing. Chapter III shows the DC characteristics and RF performance parameters of the different kinds of MBE-grown devices used for all the experimental work.

We have performed DC stress on the HEMTs, and explained the shift in DC characteristics observed using density functional theory calculations, as detailed in Chapter IV. Chapter V shows the RF stress results on MBE-grown HEMTs. In Chapter VI, low frequency $1/f$ noise measurements at room temperature are shown, and the change in noise following stress is described. Again, DFT calculations are used to identify defects limiting the reliability of the HEMTs.

In Chapter VII, we discuss the noise spectroscopy of GaN HEMTs, and identify defects which contribute to noise. Defect energy distributions are obtained from the noise measurements done over the temperature range from 85 K to 450 K. We also show noise measurement results under both low current and high current conditions. The effect of DC stress on the defect energy distributions is also shown.

In Chapter VIII, we discuss the 1.8 MeV-proton-induced degradation of GaN HEMTs grown using MBE and MOCVD. The defects created by protons are discussed, and the differences in the nature of degradation induced by protons and hot electrons are illustrated.

Chapter IX concludes the dissertation, outlining the essential contributions of this work to the existing literature.

CHAPTER 2

BACKGROUND

GaN HEMTs are grown by metal organic chemical vapor deposition (MOCVD) and molecular beam epitaxy (MBE) techniques. In this chapter, the growth techniques are discussed in order to understand the differences in the fabricated samples that were used in the experiments reported here, and also to compare the techniques in terms of reliability.

2.1 Growth techniques for GaN HEMTs

Fig. 2.1 shows the structure of a typical GaN/AlGaN HEMT. The GaN and AlGaN layers are either deposited (MOCVD) or grown epitaxially (MBE). Epitaxy is a core process for the production of III-N devices. Here we review growth by MOCVD and MBE. In general, MOCVD growth of GaN is performed at much higher temperatures ($>1000\text{ }^{\circ}\text{C}$) than MBE growth, which is typically performed at temperatures of about $700\text{ }^{\circ}\text{C}$. MBE growth enables the growth of precise interfaces, which improve transport properties.

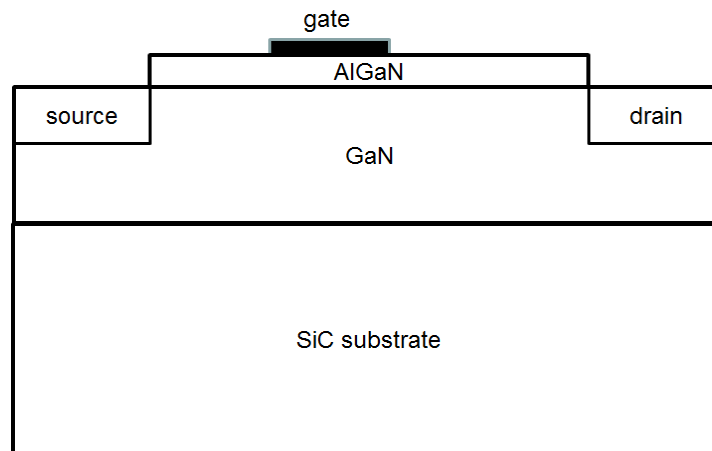


Fig. 2.1. Typical GaN/AlGaN HEMT structure

2.1.1 Surface preparation

Specific surface preparation methods have been developed to improve the surface roughness prior to epitaxial deposition. These procedures also assure that the reactor spaces are not contaminated by extrinsic pollution. Standard surface-polishing techniques are based on plastic deformation by an abrasive, such as diamond. The electrochemical-mechanical polishing (ECMP) procedure improves the reproducibility of the epitaxial growth and is preferred to purely chemical-mechanical polishing (CMP), as the induced subsurface damage is reduced. A two-step ECMP process for SiC includes (a) a balance of anodic oxidation and oxide removal to obtain a defect-free surface of the substrate, and (b) a high temperature hydrogen etching process to further smooth the surface to atomic levels [3]. An increased defect concentration in the substrate leads to increased gate leakage [4].

Further wafer preparation includes the deposition of a Ti layer on the backside of the transparent substrate prior to growth to provide effective heat transfer, typically for MBE growth only [5]. A sputtered Mo thermal contact is used in ammonia-MBE [6].

There are various cleaning conditions and sequences with prebake and flush for moisture removal prior to growth. A potential reaction is the formation of H_2O from a reaction of Al_2O_3 and hydrogen. Incorporation of oxygen, which serves as a shallow donor, is a major obstacle for producing semi-insulating GaN. The optimized cleaning procedure involves both the prebake in situ and no flush, and is critical in obtaining semi-insulating GaN buffers.

2.1.2 Metal-Organic Chemical Vapor Deposition

MOCVD is the name of the growth technique that involves a dynamic flow in which gaseous reactants pass over a heated substrate and react chemically to form a semiconductor layer. III-N MOCVD has a higher growth rate than MBE.

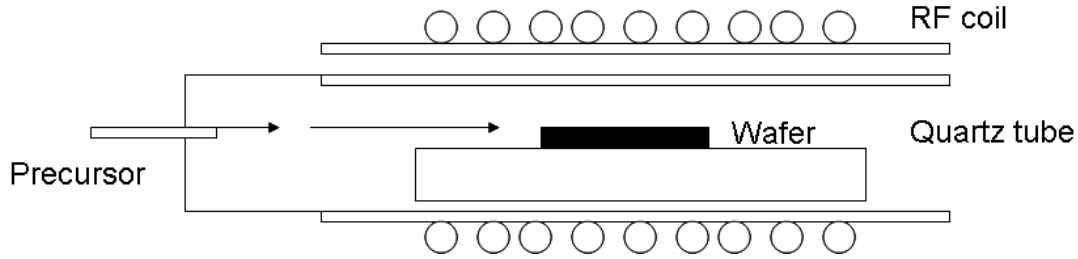
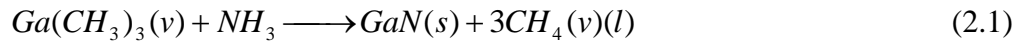


Fig. 2.2. Schematic diagram of metal organic chemical vapor deposition (MOCVD) growth.

The precursors, TriMethyl-Gallium (TMGa) and TriMethyl-Aluminium (TMAI) react with ammonia (NH_3) on the hot substrate surface to form semiconductor layers. Additional sources, such as nitrogen, silane (SiH_4), disilane (Si_2H_6) and Bis(cyclopentadienyl) magnesium (Cp_2Mg) sources are needed. The principal reaction to form GaN is:



A similar reaction occurs for AlN(s) replacing Ga by Al. The chemistry is governed by strong reactions of the precursors at room temperature. Further, ammonia requires pyrolysis, which is not very efficient. Thus, high growth temperatures beyond $1000^\circ C$ are used along with high V/III ratios (>1000) and high gas velocities.

The complete range of solid solutions from GaN to pure AlN is available by MOCVD growth, which is one of the key advantages of the AlGaIn/GaN system. Typical growth rates for GaN are $\sim 2 \mu m/h$. The aluminum mole fraction x in an $Al_xGa_{1-x}N/GaN$ heterostructure is varied between 0 and 0.6. The defect density in the $Al_xGa_{1-x}N$ layer on GaN increases significantly for $x \geq 0.3$, with the barrier thickness typically being 18 nm for HFETs. The mobility in GaN channels

along GaN/AlGaIn interfaces decreases with decreasing barrier-layer thickness. Sheet carrier concentrations of $1.8 \times 10^{13} \text{ cm}^{-2}$ are reached for $x = 0.44$. The critical growth parameters are discussed below.

i. Growth temperature

The growth temperatures determine the properties of the semiconductor layers. An AlN nucleation layer is grown at a temperature of 500-700 °C on sapphire substrates. A GaN nucleation layer is grown at 550 °C on sapphire. AlGaIn nucleation layers have to be grown at a higher temperature (>1000 °C) on SiC or sapphire. The minimum Al content is 6% for SiC and 15% for nucleation on sapphire. The subsequent growth of GaN buffer layers on the nucleation layer is performed at >1000 °C.

The channel and barrier layers are grown at >1000 °C. The growth temperature is chosen accordingly for Al-, In-, and Ga-based binary and ternary semiconductors within the interlayer. Hot growth of the AlGaIn layer is promising with respect to the output power considerations, while a termination of the growth in the cool-down using nitrogen is most suitable for AlGaIn/GaN HEMTs grown on SiC.

ii. MOCVD gas flow and Group V/III ratios

Nitrogen-rich growth is necessary for MOCVD in general because of the differences in chemical bindings and atomic weights of the constituent N and group III-elements. The absolute and relative gas pressures depend on the susceptor and reactor geometries. TMG flows of 32 $\mu\text{mol/min}$ and NH_3 flows of 0.09 mol/min for N-rich growth are reported for GaN growth. The V/III ratio is 2775 [7].

iii. Growth pressure

Pressure determines the incorporation of the various constituents, including group V and group III materials, plus group IV dopants like Si and C. For a very low pressure of 40 Torr, the GaN layers are highly resistive and yield very low carrier mobility, nearly independent of the growth temperatures. At very high pressure of > 200 Torr, the resistive nature of GaN is lost. In an intermediate pressure range, both high mobility and high resistivity (i.e., low unintentional doping) can be obtained in GaN layers. Optimized growth pressures are 65-130 Torr [8]. The critical pressure, at which pressure pre-reactions occur, depends on the reactor geometry. The pressure dependence for the growth of AlGaN is modified by the Al mole fraction. The partial pressures of Al and Ga and their deviation from the equilibrium partial pressures influence the Al mole fraction, for a given V/III ratio and growth temperature. Thus, lower pressures than for optimized GaN layers are needed for good Al-incorporation in the AlGaN layers [9]. $\text{Al}_{0.15}\text{Ga}_{0.85}\text{N}$ is formed at a medium growth pressure of 76 Torr, due to the tendency of TMAI to form adducts with ammonia [9,10]. At higher growth pressures, increased incorporation of unintentional doping such as Si and C takes place.

iv. Crystal misorientation

GaN is grown on both on-axis and off-axis 6H-SiC substrates. MOCVD-grown GaN epitaxial layers show a good morphology for on-axis 4H-SiC and 6H-SiC [11], but the crack density increases with increasing misorientation [12]. This effect can be compensated by other parameters, such as growth temperature [11]. A slight misorientation of 3.5° compared to the on-axis layer causes an increase in mobility and carrier reduction in Si-doped GaN films. Positron

annihilation spectroscopy shows that, with increasing misorientation on 4H-SiC, the concentration of nitrogen vacancies in GaN increases, while the number of shallow traps decreases [13]. This can potentially have an impact on device isolation in the buffer layer, if the misorientation is not controlled. The morphology of GaN grown on 4H-SiC (0001) with a strong misorientation of 8° is strongly affected by undulations, but this is not the case with misorientations $\leq 0.3^\circ$. Thus a controlled misorientation can be useful for the electronic device performance, if the growth parameters are properly matched.

v. Nucleation layer

The conditions for the growth of the nucleation layer are critical for the defect concentration, residual conduction, and the distribution of defects and traps in all layers grown on top of it [10,11]. The nucleation layer depends naturally on the choice of the substrate. The grain orientation can be improved with increased nitridation temperature. Further, the quality of the epitaxial GaN is improved by increases in growth temperature and pressure.

vi. Buffer isolation

The growth of the buffer layer in an AlGaIn/GaN heterostructure is a trade-off between high isolation and surface morphology. Buffer isolation values range from 10^5 to 10^{11} $\Omega\cdot\text{cm}$ [8,14,15].

vii. Buffer layer thickness

Thin buffer layers promise reduced thermal impedance and low growth time, while the growth of thicker layers reduces the effects of threading dislocation density and residual strain

from the lattice mismatch [16]. Surface morphology improves for buffer layer thicknesses of 2-3 μm [14]. Thicker buffer layers promise smoother growth fronts with improved interface roughness, reduced dislocation density, and further removal of the active region from the defective nucleation layer.

viii. Co-doping of buffer layers

Unintentional co-doping is a major problem for non-optimized growth conditions. Co-doping introduces unintentional background carrier concentration and thus persistent unintentional conductivity. N-vacancies and oxygen act as shallow donors [9]. Carbon is a contaminant in MOCVD reactors due to methyl precursors [17]. Mg and Fe are intentional dopants, which can be residual from reactor memory effects. Fe and C are used to control isolation in buffer layers by pinning the Fermi level in the buffer, and to overcome the need of a second heterojunction. Fe doping improves the stability of semi-insulating GaN layers, and reduces dispersion, especially drain-lag. At the same time, Fe doping does not modify the good structural quality of the layer. Thus, improved isolation is achieved without a high threading dislocation density (TDD).

Low pressure growth at 76 Torr, compared to 760 Torr, leads to increased carbon incorporation in the GaN layers at 1040 °C [18]. Carbon supplies both shallow and deep acceptor levels in n-type GaN. It contributes to the compensation of free carriers. C-doped samples are found to be highly resistive, while co-doping with both Si and C leads to highly compensated layers. This finding is of great importance, because C and O are typically present in all MOCVD reactor chambers. Higher growth temperatures of 1150 °C lead to reduced oxygen and carbon incorporation. Co-doping with indium suppresses the formation of native acceptor-like defects.

2.1.3 Molecular Beam Epitaxy

MBE is another attractive growth method for III-N semiconductors. The growth of semiconductors by MBE occurs via reactions between thermal-energy molecular, atomic, or ionized beams of the constituent elements on a heated substrate in an ultrahigh vacuum. The advantages of MBE lie in the precise definition of interfaces and the increased polarity of the interfaces. The disadvantage is the reduced growth rate relative to MOCVD growth. The growth rate of III-N MBE is 0.5-1 $\mu\text{m/h}$ [16].

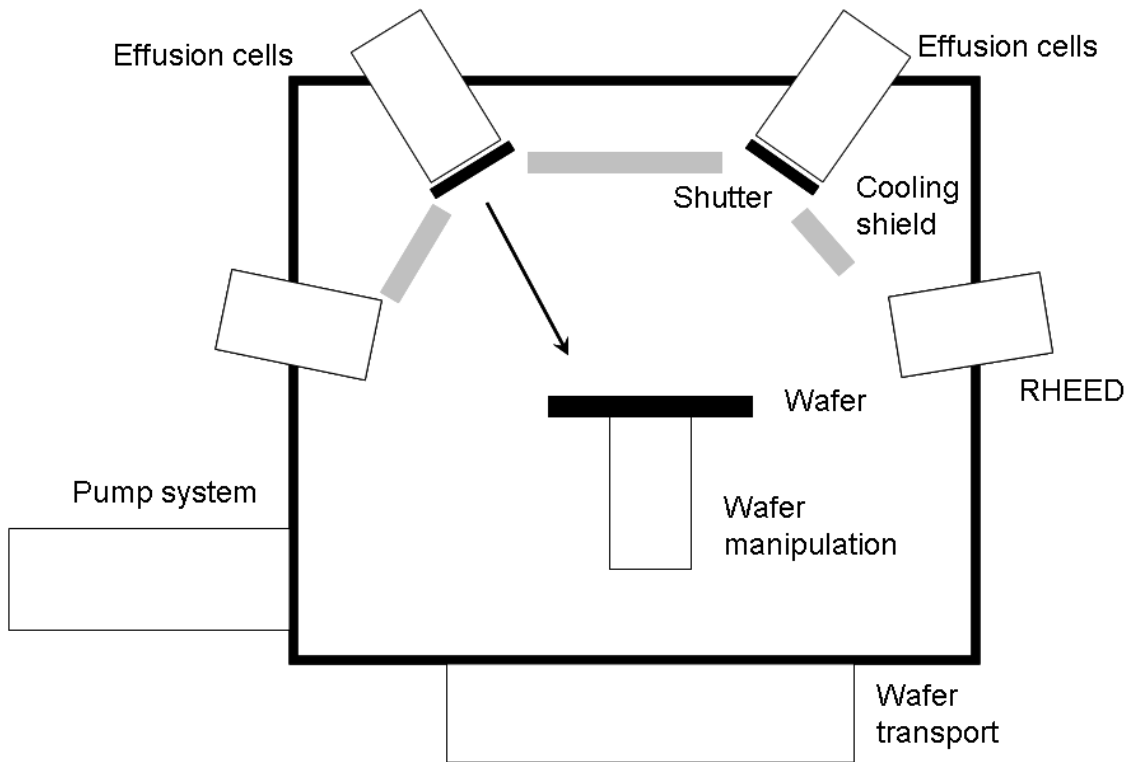


Fig. 2.3. Schematic illustration of molecular beam epitaxy (MBE) growth.

The molecular beams of Ga and Al originate from effusion cell sources. An elemental group-V N-source is not practical to develop due to the very high binding energy of the N_2 . N radicals are generated either by a RF-plasma source, or by an ammonia source. The background pressure amounts to $\leq 10^{-11}$ mbar during the MBE growth. The substrates are typically rotated

during the growth. The growth temperature is around 800 °C for GaN. AlN is typically used as a nucleation layer in MBE. The optimized conditions for MBE growth are described below.

i. Growth temperature

The substrates are typically inserted into the growth chamber via a preparation chamber, before the actual growth procedure. The substrates are out-gassed in the preparation chamber. A typical substrate outgas temperature in the preparation chamber is 700 °C [19]. The temperature reaches 1000 °C for oxide removal. The nucleation temperature for AlN on sapphire substrate is ~800 °C. The growth of the insulating GaN buffer layer on top of a nucleation layer is performed at 745 °C, for Ga-rich conditions [19,20]. The GaN channel layers are usually grown at 800 °C using atomic nitrogen [14]. The nominal growth temperatures for ammonia-rich MBE growth are 910-920 °C for GaN and 880 °C for AlN [21,22].

ii. N-Group-III ratio for MBE growth

As in MOCVD growth, the V/III ratio is critical for MBE growth as well, but for a different reason. The V/III ratio determines the quality of the epitaxial layers. Three characteristic growth regimes are N-stable, intermediate, and Ga-droplet [23,24]. Within the Ga-droplet regime, excess Ga accumulates on the surface during growth in the form of large droplets. Within the intermediate regime, excess Ga forms a steady-state adlayer of metallic Ga on the surface without the formation of Ga droplets. Films grown in the N-stable regime are Ga deficient so that the growth rate is limited by the available Ga flux. N-stable-grown GaN films are semi-insulating. GaN layers grown with ratios in the intermediate regime yield fewer pits with atomically flat surfaces. At high Ga/N-ratio, the mobility decreases significantly. The best

material is thus grown in the intermediate regime. The best combination of surface morphology and material quality is obtained by a modulated technique varying Ga-rich and Ga-lean growths alternately.

For ammonia-MBE, carbon-doped insulating GaN MBE layers are grown on semi-insulating SiC at a temperature of 910 °C. The growth rates reach 1-2 $\mu\text{m/h}$ by adjusting the ammonia flow [22].

iii. Nucleation layer growth by MBE

The nucleation layer is of very high importance on various substrates, since this region contributes to the quality of the MBE-grown active semiconductor layers, and thus to the device performance. A 100 nm-thick AlN nucleation layer is normally grown at a temperature of 835 °C [25].

iv. Growth and isolation of buffer

The lower growth rate of MBE compared to MOCVD favors a reduced layer thickness for MBE growth, especially that of the buffer layer. The buffer-substrate interface is susceptible to isolation issues due to the high concentration of defects. The carrier concentration increases near the interface but the mobility decreases. This behavior can be explained by both interface conduction and impurity band conduction.

v. Co-doping in MBE material

Intentional co-doping is of great importance for the isolation of the nucleation and the buffer layers. Carbon and oxygen (unintentionally) are used for co-doping during MBE growth,

since Fe sources are unavailable. Carbon introduces a midgap state that helps to increase the isolation in the buffer layers. Unintentional incorporation of oxygen into GaN layers is a major problem in MBE growth. The background vacuum pressure, the nitrogen source, and the metal source are potentially sources of oxygen [26]. Ga-rich growth of AlGaN reduces the oxygen incorporation by a factor of three. Temperature reduction from 750 °C to 650 °C increases oxygen incorporation significantly. Intentional incorporation of oxygen is controllable and reproducible up to a doping level of 10^{18} cm^{-3} . Oxygen is an effective donor with low compensation and its incorporation also depends on the growth polarity. Plasma-assisted MBE(PAMBE)-grown layers with N-polarity incorporate about 50 times as much oxygen as Ga-face material [27].

vi. Channel and barrier layers grown by MBE

The growth conditions for the GaN channel layers are of primary importance for the material quality. GaN channel layers are grown by PAMBE at 735 °C at a growth rate of 0.37 $\mu\text{m/h}$ in Ga-rich conditions [25]. The AlGaN barrier can be grown at the same temperature and at the same nitrogen flow as GaN. For ammonia-MBE growth on semi-insulating SiC, the GaN channel layers are typically grown at $\sim 900 \text{ °C}$ [28].

vii. Dislocations in MBE material

The threading dislocation density (TDD) in MBE-grown layers can be reduced to densities similar to those achieved for MOCVD-grown materials. The TDD can be reduced to $\leq 10^9 \text{ cm}^{-2}$ on semi-insulating SiC, using PAMBE [29]. The leakage current has an exponential dependence on the threading dislocation density, suggesting either a trap-assisted tunneling or a

one-dimensional hopping mechanism [30,31]. Edge and mixed type dislocations have a negative charge, and have limited contribution to the leakage. Pure screw dislocations provide a conductive leakage path [32]. On resistive Si substrates, the TDD amounts to $5\text{-}7\times 10^9\text{ cm}^{-2}$ [33].

2.2. Summary

In this chapter, we discussed the details of MOCVD and MBE processes for the growth of GaN. This is important to put into perspective why we use these devices for our reliability studies, which are discussed in the subsequent chapters. MOCVD growth allows high temperatures and gives a higher growth rate compared to MBE processes. But MBE allows precise interfaces and better transport properties compared to MOCVD growth. The three kinds of MBE-grown devices studied here are those grown under Ga-rich, N-rich, and NH_3 -rich conditions. While growth in Ga-rich conditions ensures lower surface roughness than N-rich growth, there typically is a lower threading dislocation density in N-rich growth [34,35]. Ammonia-MBE, where ammonia is used as the nitrogen source, is considered to be a promising alternative growth method. Ammonia-MBE has several advantages over PAMBE. It allows a larger growth window and a potentially higher growth rate. Higher temperatures ($>750\text{ }^\circ\text{C}$) can be used, because of the metal-free surface, which may reduce defect densities in GaN buffer layers, improving two-dimensional electron gas (2DEG) mobilities [36,37]. MOCVD-growth occurs in the presence of ammonia, and hence the reliability of these devices may be compared to those grown using ammonia-rich MBE.

CHAPTER 3

DC AND AC CHARACTERISTICS OF GaN HEMTs

3.1 Introduction

AlGaN/GaN HEMTs were obtained from the University of California, Santa Barbara. These devices were grown by molecular beam epitaxy under Ga-rich, N-rich, and NH_3 -rich conditions. Devices grown using metallorganic chemical vapor deposition were also provided. In this chapter, the DC, small signal and large signal characteristics of the MBE-grown HEMTs, which have been used for experiments in the remainder of the thesis, are shown.

3.2 DC and AC characteristics of GaN HEMTs used in the thesis

The epitaxial structures of the GaN HEMTs are shown in Fig. 3.1. The HEMTs are $150\ \mu\text{m}$ wide, with a gate length of $0.7\ \mu\text{m}$; $L_{GD} = 1.2\ \mu\text{m}$, $L_{GS} = 0.7\ \mu\text{m}$. The MOCVD-grown devices have an AlN interlayer between the AlGaN barrier and GaN bulk for improved electron confinement and higher electron mobility in the 2DEG.

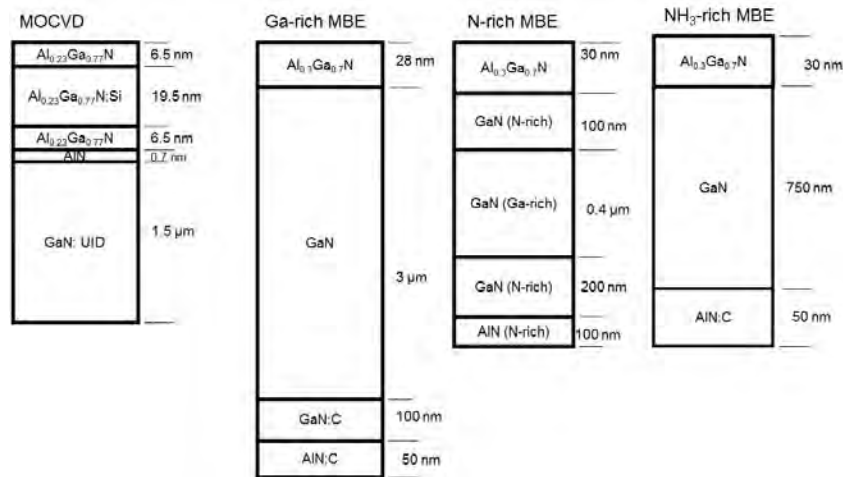


Fig. 3.1. Epitaxial structure of HEMTs.

Figures 3.2-3.4 show the DC characteristic curves for typical Ga-rich, N-rich, and NH_3 -rich devices. The Ga-rich devices show the highest saturation current, with $I_{D\text{max}}$ being ~ 1200 mA/mm. The gate leakage current is also minimum for Ga-rich devices. N-rich and NH_3 -rich devices show a high leakage current of ~ 1 mA/mm for $V_G = -5$ V, and $V_D = 7$ V.

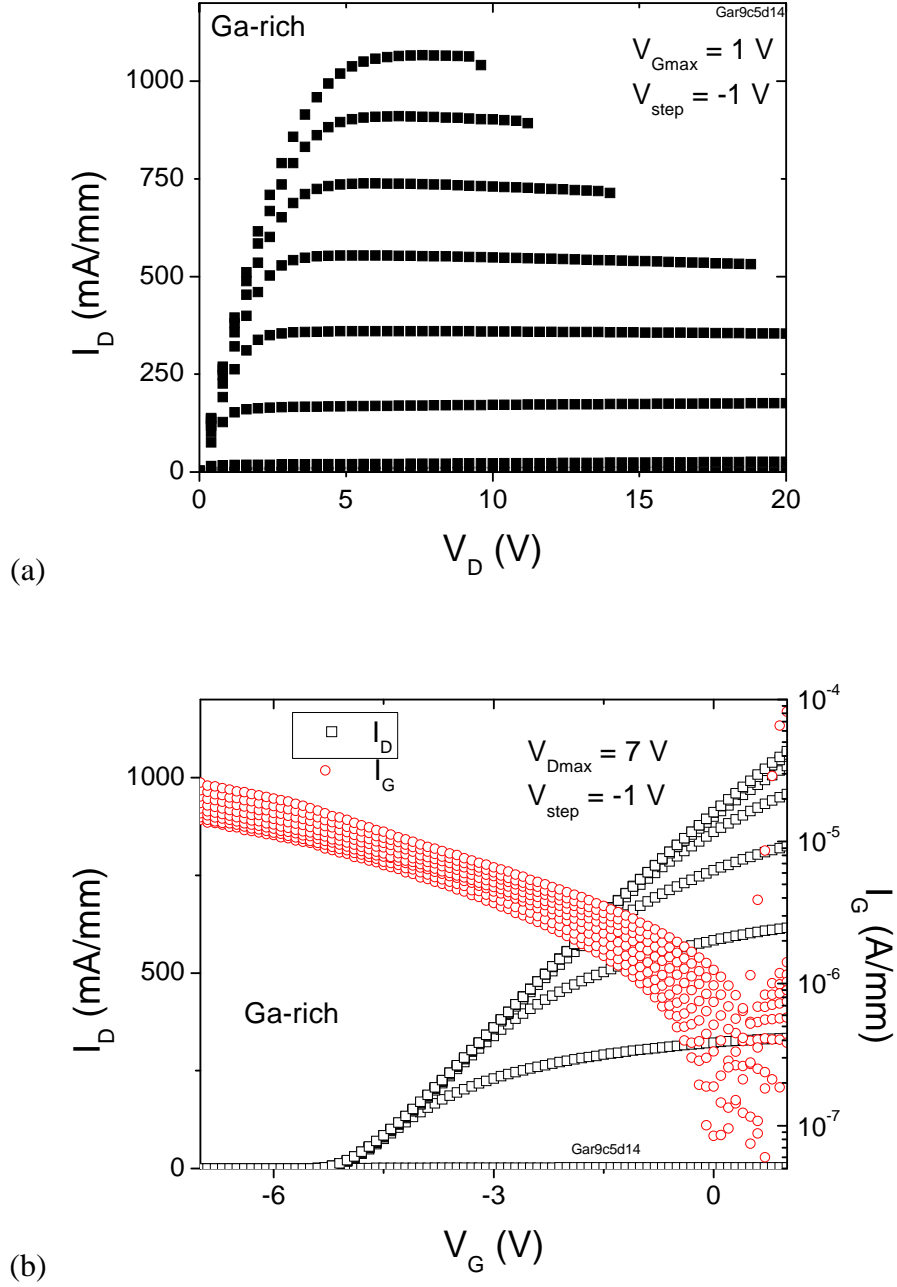
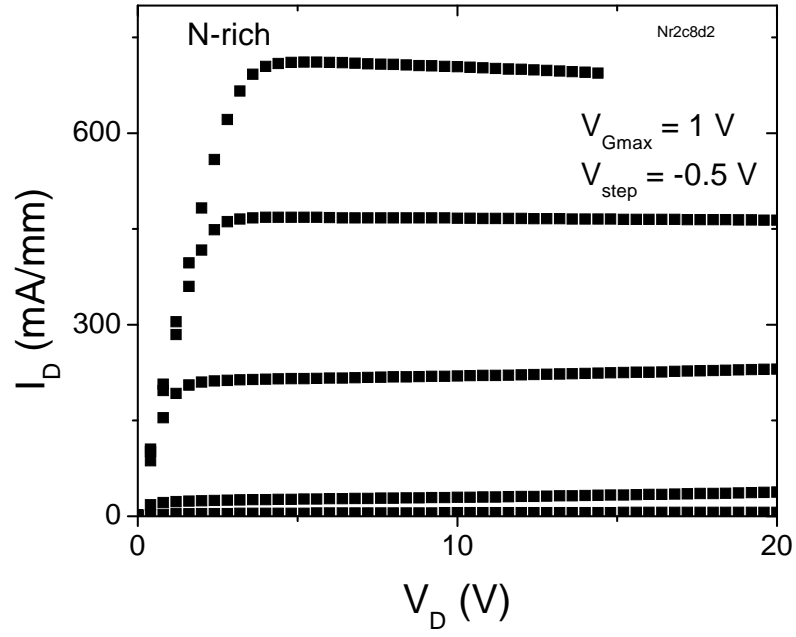
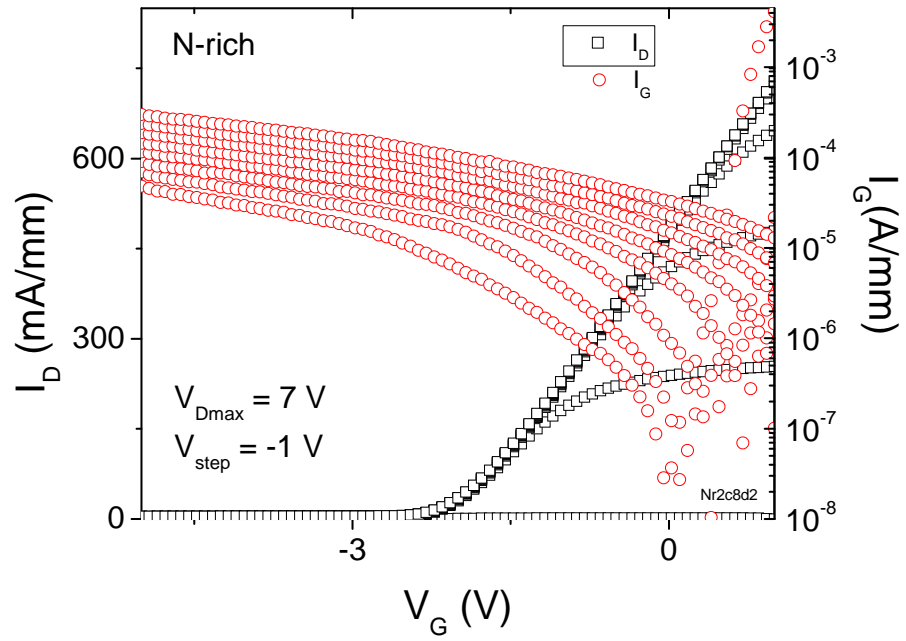


Fig. 3.2. (a) I_D - V_D and (b) I_D - V_G and I_G - V_G curves for a Ga-rich HEMT.

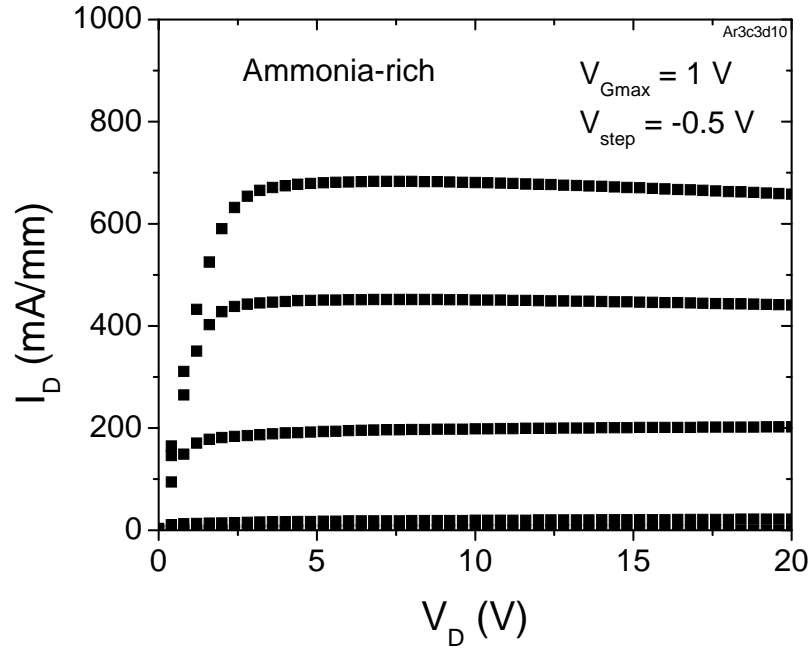


(a)

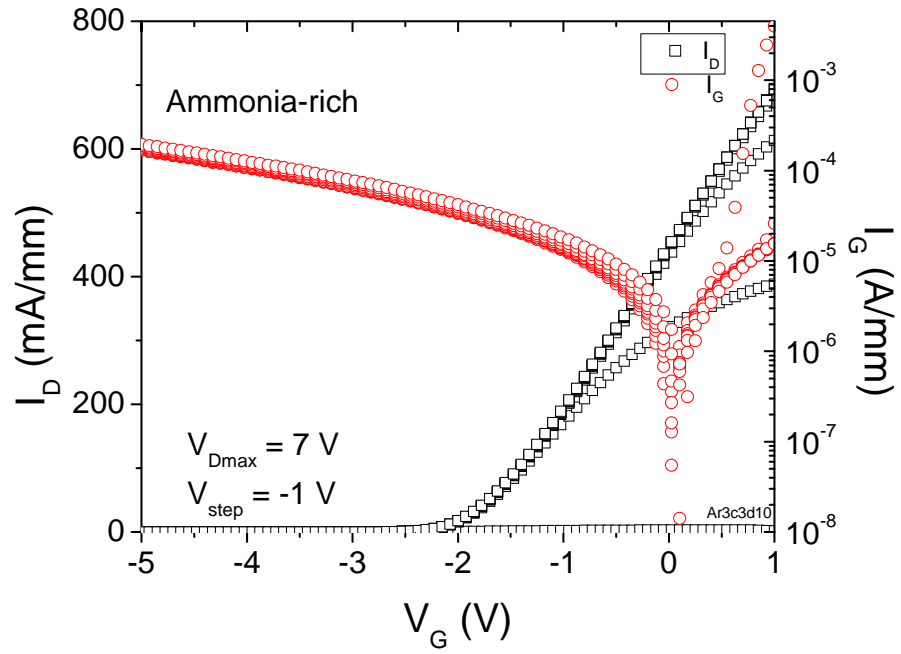


(b)

Fig. 3.3.(a) I_D - V_D and (b) I_D - V_G and I_G - V_G curves for a N-rich HEMT.



(a)



(b)

Fig. 3.4.(a) I_D - V_D and (b) I_D - V_G and I_G - V_G curves for an NH_3 -rich HEMT.

Figure 3.5(a)-(c) shows a comparison of DC transconductance with transconductance at 10 GHz. The peak DC transconductance is ~ 200 mS/mm. The transconductance clearly drops off at high frequencies, due to trapping effects in these devices. A similar observation is made in [38] for devices with 55 nm gate length. The g_m drop-off at high frequencies degrades the frequency performance of GaN devices, by causing f_T to be lower than what intrinsic material properties predict [38].

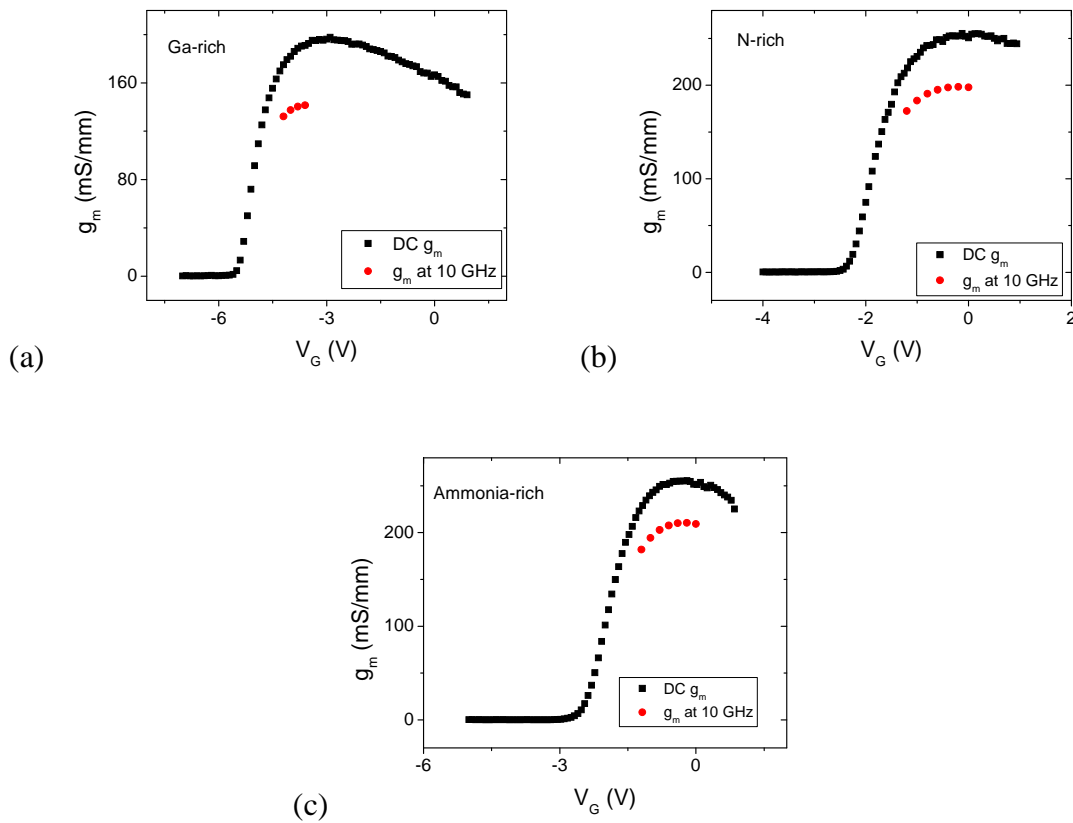


Fig. 3.5. Comparison of DC transconductance with transconductance at 10 GHz for (a) Ga-rich, (b) N-rich, and (c) NH_3 -rich HEMTs.

The small signal characteristics of the three kinds of MBE-grown HEMTs are shown in Figs. 3.6-3.8. The peak unity gain frequency f_T is in the range of 15-20 GHz for the devices. If we consider that carriers are moving at saturation velocity, the cutoff frequency is given by:

$$f_T = \frac{v_s}{2\pi L} \quad (3.1)$$

where $v_s = 2.5 \times 10^7$ cm/s, and $L = 0.7$ μm , the cutoff frequency is ~ 50 GHz. Thus, the values of f_T obtained for our devices emphasize the presence of significant trapping phenomena, limiting the high-frequency performance of these devices. The maximum oscillation frequency, f_{MAX} is in the range of 25-35 GHz.

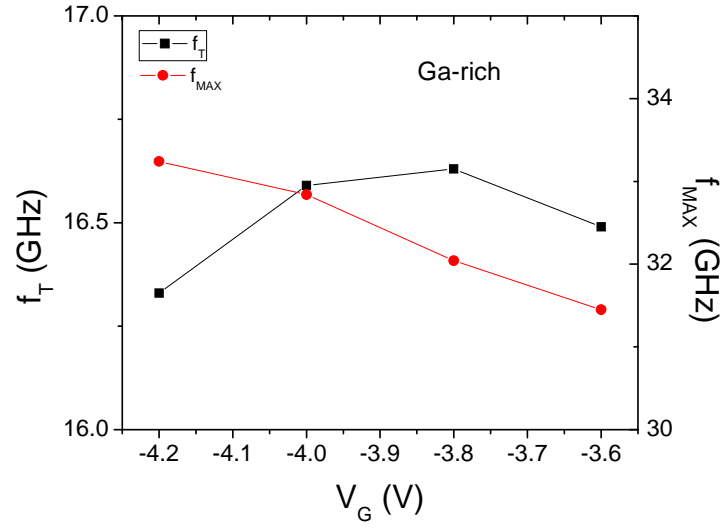


Fig. 3.6. f_T and f_{MAX} vs. V_G for a Ga-rich device.

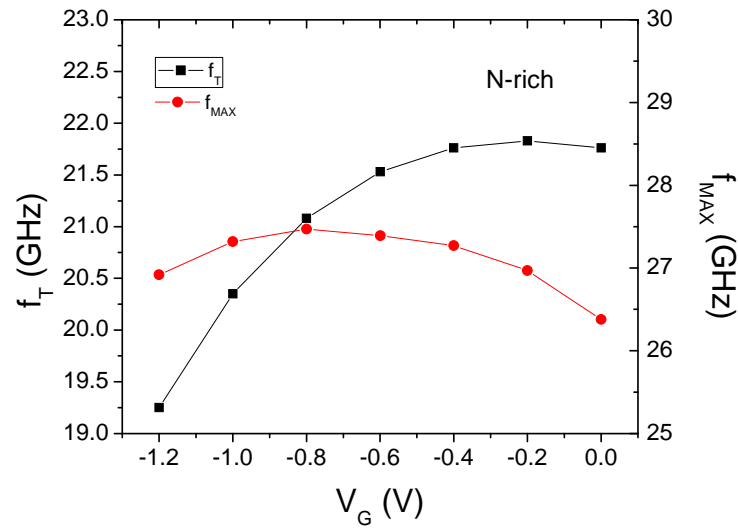


Fig. 3.7. f_T and f_{MAX} vs. V_G for an N-rich device.

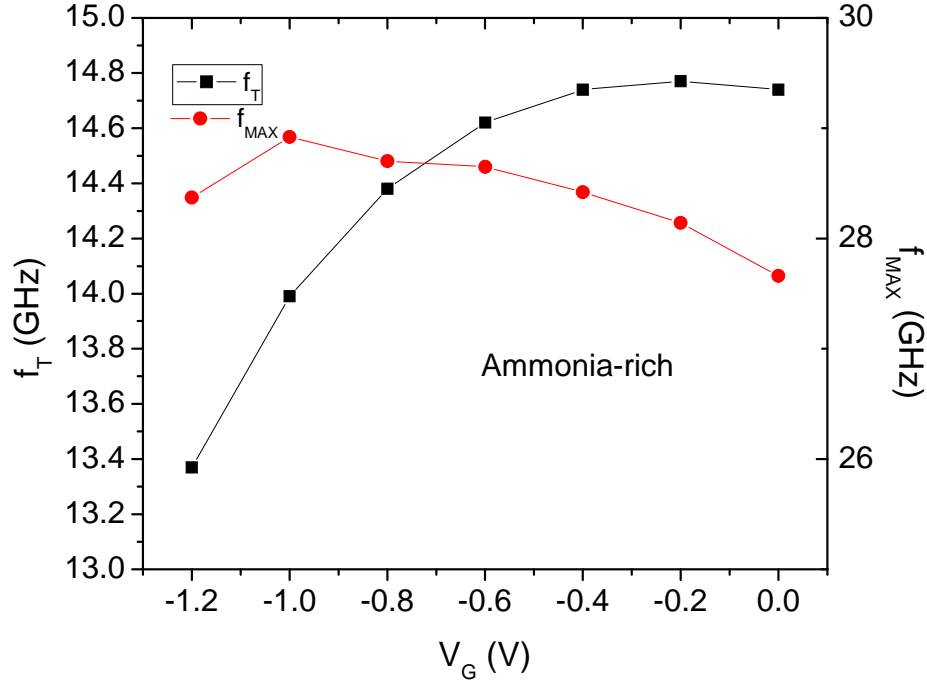


Fig. 3.8. f_T and f_{MAX} vs. V_G for an NH_3 -rich device.

In Fig. 3.9, the large signal performance of the GaN HEMTs is shown when operated as Class AB power amplifiers, using a load-pull measurement setup. The device is biased close to pinch-off in class AB mode, so that the device operates as an amplifier for half of the cycle and remains cut-off for the other half. This condition is of interest to us since hot electron-induced degradation occurs under such bias conditions. The quiescent drain voltage was fixed at 20 V during the large signal measurements. The quiescent gate voltage was -4.5 V, -1.5 V and -0.6 V for Ga-rich, N-rich, and NH_3 -rich devices, respectively. The frequency is 10 GHz. The input power P_{in} was swept till a gain compression of 4.5 dB was observed in the output power P_{out} . The power added efficiency P.A.E. is $<40\%$ in all devices, indicating rf dispersion due to trapping.

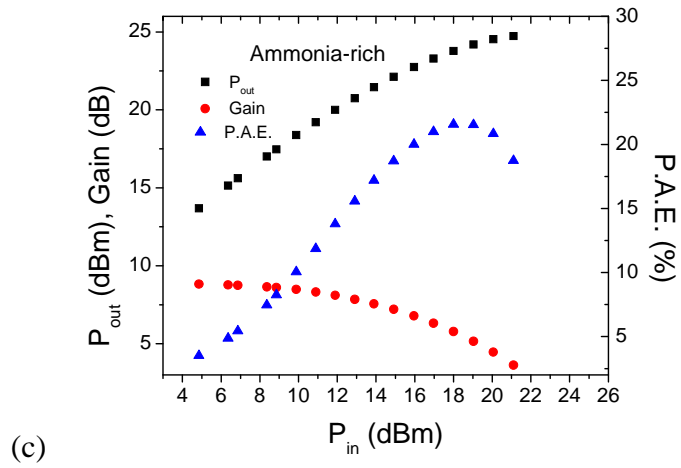
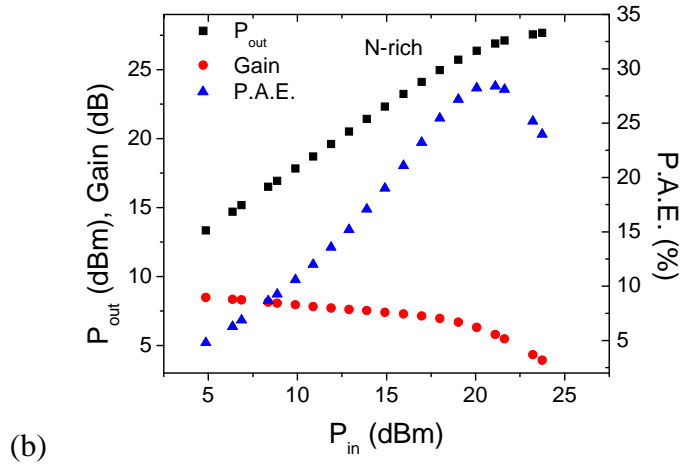
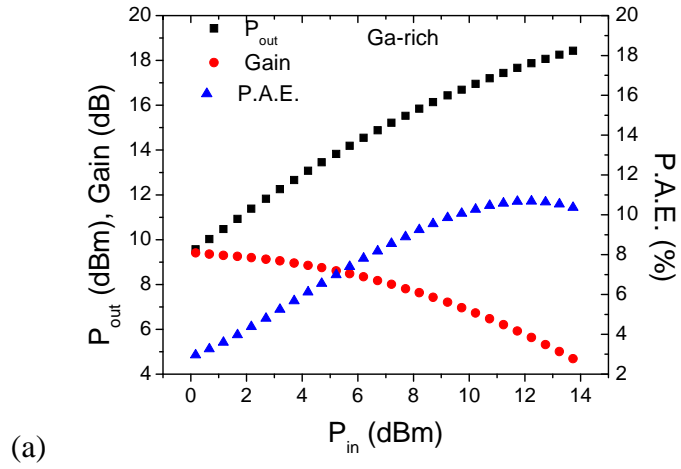


Fig. 3.9. Load-pull measurements showing large signal performance of (a) Ga-rich, (b) N-rich, and (c) NH_3 -rich HEMTs when operated as class AB power amplifiers.

3.3 Summary

DC, small signal and large signal measurements were performed on GaN HEMTs grown using MBE under Ga-rich, N-rich, and NH_3 -rich conditions. The f_T of these HEMTs is in the range of 20 GHz, which is less than the theoretical value. The peak transconductance drops off when the device is operated at high frequencies, indicating the presence of a large number of traps. Considerable rf dispersion is noticed through large signal measurements, since the power added efficiency is less than 40% for all kinds of devices, emphasizing the need for studying the reliability of these devices.

CHAPTER 4

HOT ELECTRON-INDUCED DEGRADATION IN GaN HEMTs

4.1 Introduction

The presence of native defects in GaN may cause drain current collapse – a decrease in the measured output power when the device is operated at microwave frequencies from the theoretical output power calculated using the $I_{D,max}$ and V_{knee} measured at DC, which is an impediment to the deployment of these devices in high-power, high-frequency applications [39]. Moreover, III-V HEMTs exhibit shifts in peak transconductance when devices are stored in an atmosphere containing substantial amounts of hydrogen gas [40]. In GaN-based structures, hydrogen accumulates in strained regions (e.g., near an interface) [41], and also interacts strongly with defects and impurities [42]. Atomic hydrogen readily permeates into GaN during the fabrication process, such as during boiling in solvents (including water), annealing in hydrogen or ammonia, and during wet etching in acid or base solutions. This naturally leads to hydrogenation of a significant number of defects in the devices. Previous investigations have not resolved the role of process-related defects in GaN/AlGaN reliability. Thus, it is important to determine the potential role of defects and hydrogen on the reliability of GaN/AlGaN HEMTs [43,44].

In this chapter, we report the effects of room-temperature electrical stress on AlGaN/GaN HEMTs grown under using MOCVD and MBE under Ga-rich, N-rich, and NH_3 -rich conditions. The stress-induced shift in $V_{pinch-off}$ is negative for the devices grown using MOCVD and MBE under NH_3 -rich conditions, while it is positive for the N-rich and Ga-rich MBE-grown devices.

This qualitatively different behavior suggests that different kinds of defects are responsible for the degradation of devices grown in NH_3 -rich conditions compared to the other two conditions. We report density functional theory calculations of the formation energy of defects under specific growth conditions, showing the critical importance of hydrogen to the degradation process and device reliability. In particular, hydrogenated Ga vacancies and N anti-site defects play key roles, with the dominant defect type determined by the details of the processing conditions. [45-47]

4.2 Experiments

The devices were all electrically stressed with a drain voltage of 20 V to keep the horizontal field along the channel the same for all cases. Each device was stressed at the same power dissipation level of 3.33 W/mm, so that the channel temperature remained the same for all the samples. The gate voltage during the stress was set near the pinch-off voltage, so the vertical field at the gate-drain edge of the channel was relatively high. The degradation under conditions of high electric field between the gate and the drain is caused by hot electrons [48].

4.3 Threshold voltage and peak g_m shifts after stress

The DC transconductance before and after 8 h of stress is shown in Fig. 4.1 for all three device types at a drain voltage of 2 V. The peak transconductance shifts positively for the Ga-rich and N-rich devices after stress, while the transconductance of the NH_3 -rich devices shifts negatively. Also, there is larger peak g_m degradation for the N-rich devices compared to the other two kinds of devices.

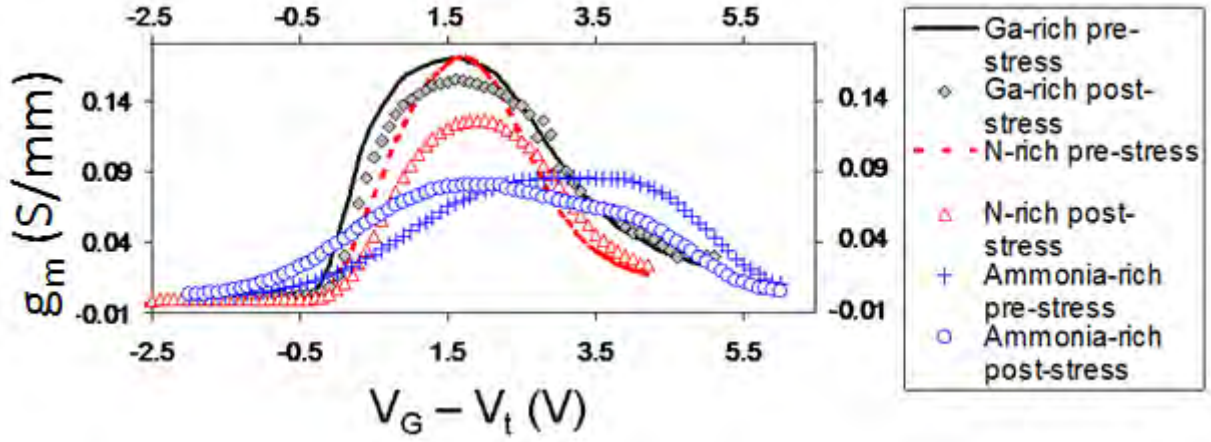


Fig. 4.1 g_m - V_{GS} for the (a) Ga-rich, (b) N-rich, and (c) NH_3 -rich samples at $V_D = 2$ V, before and after stress for 8 hours. Ga-rich device: $V_{\text{pinch-off}} = -5.1$ V, $V_{g \text{ stress}} = -4$ V. N-rich device: $V_{\text{pinch-off}} = -4.1$ V, $V_{g \text{ stress}} = -3.6$ V, NH_3 -rich device: $V_{\text{pinch-off}} = -5$ V, $V_{g \text{ stress}} = -4$ V. $V_{g \text{ stress}}$ values were chosen such that power dissipation during stress was the same in all three cases, keeping thermal effects the same in all three sample types. [45]

Fig. 4.2 shows the change in $V_{\text{pinch-off}}$ with stress time for all three sample types. $V_{\text{pinch-off}}$ shifts positively for the N-rich and Ga-rich samples, while it shifts negatively for the samples grown under NH_3 -rich conditions. This difference in the polarity of the shift strongly suggests that the nature of the traps created during stress is different in the NH_3 -rich devices than in the other two device types. The magnitude of the shift in the NH_3 -rich samples is greater than that of the other device types. Fig. 4.3 shows the shift in pinch-off voltage with stress time for devices grown using MOCVD. These are unpassivated devices. The shift in pinch-off voltage is negative, as in the ammonia-rich devices. As seen in Chapter II, ammonia is used in the MOCVD process. Thus, the negative shift in pinch-off voltage with stress in devices grown by ammonia-MBE and MOCVD strongly indicates that similar defects are created, which is facilitated by the presence of ammonia.

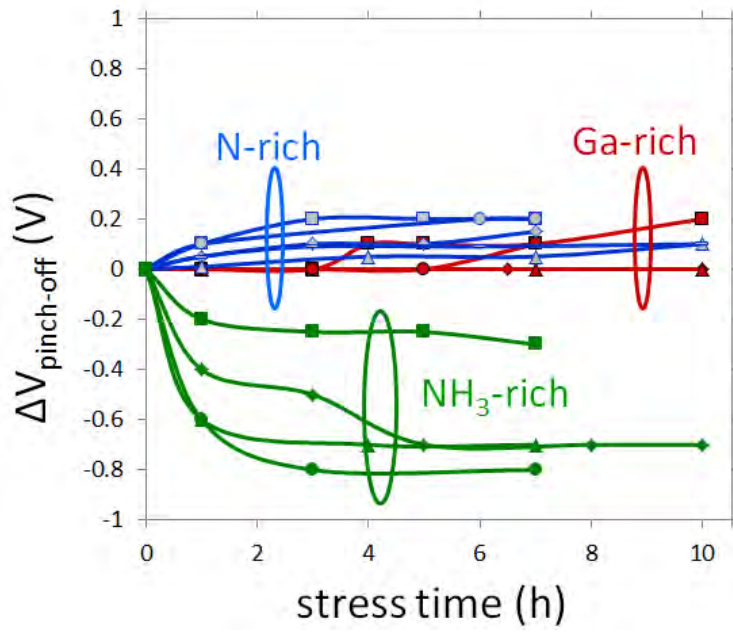


Fig. 4.2. Change in pinch-off voltage as a function of stress time, for MBE-grown GaN HEMTs. [45]

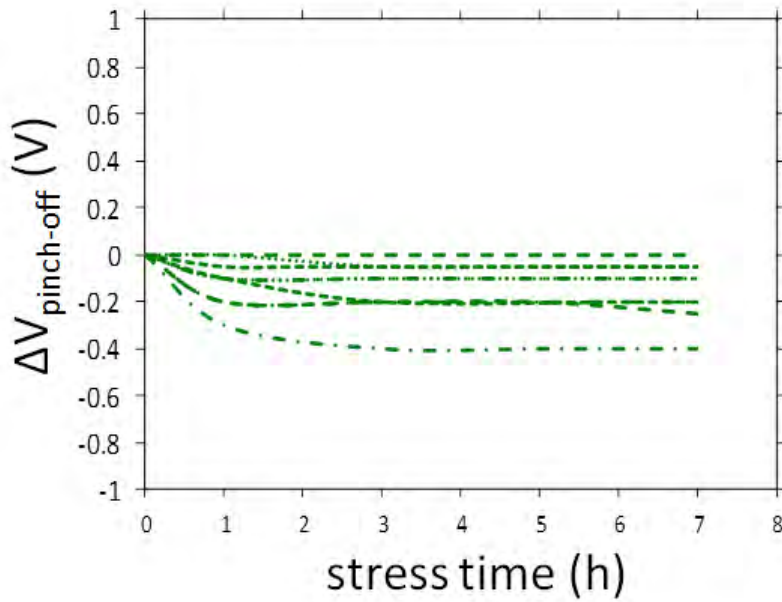


Fig. 4.3. Change in pinch-off voltage as a function of stress time for MOCVD-grown GaN HEMTs. [46]

4.3 Point defects responsible for $V_{pinch-off}$ shift

Hydrogenated native defects have a lower formation energy compared to the dehydrogenated counterparts. Hydrogen is also easily present during the fabrication process. So, a significant number of the native defects are hydrogenated. Figs. 4.4-4.7 show density functional theory calculations for the formation energy of Ga vacancies and N anti-site defects in bulk GaN and $Al_{0.3}Ga_{0.7}N$ as a function of the position of the Fermi level in the band gap of GaN and $Al_{0.3}Ga_{0.7}N$. The slopes of the lines represent the charge states of the defects. A change in slope, corresponding to the change in charge state, is the thermodynamic transition level of the defect.

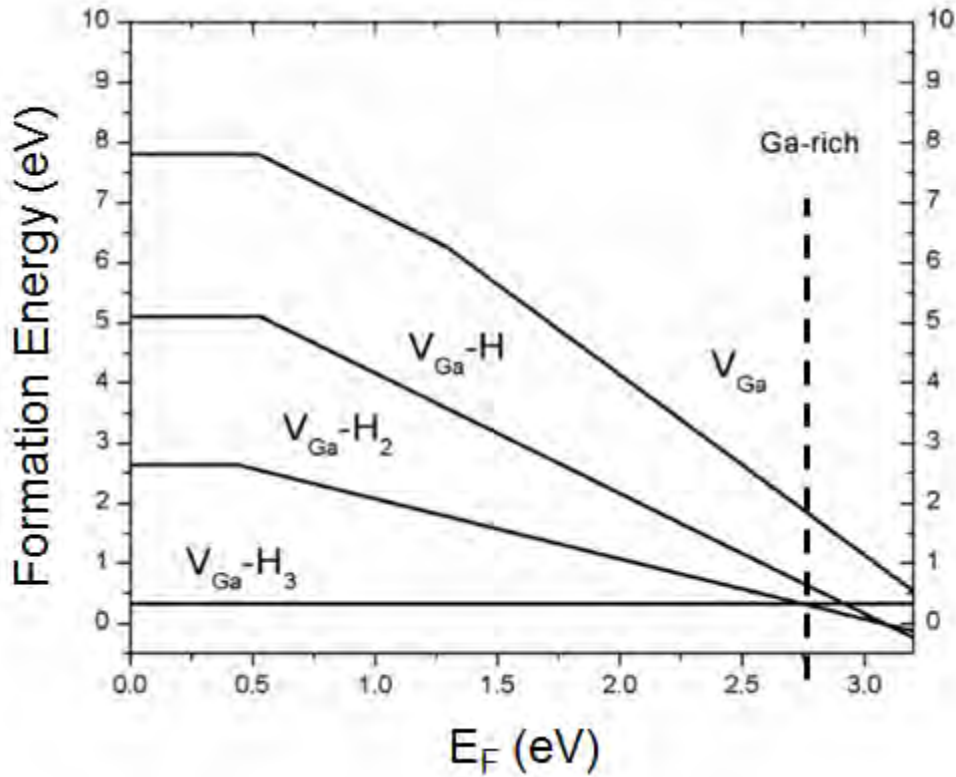


Fig. 4.4. Formation energy of hydrogenated Ga-vacancies in bulk GaN. [46]

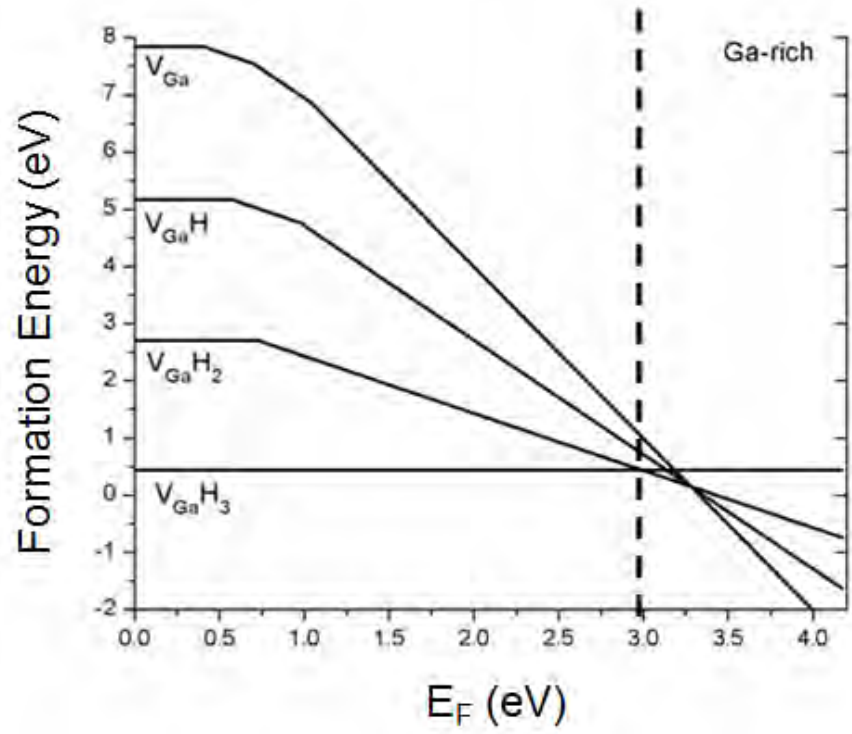


Fig. 4.5. Formation energy of hydrogenated Ga-vacancies in $\text{Al}_{0.3}\text{Ga}_{0.7}\text{N}$. [47]

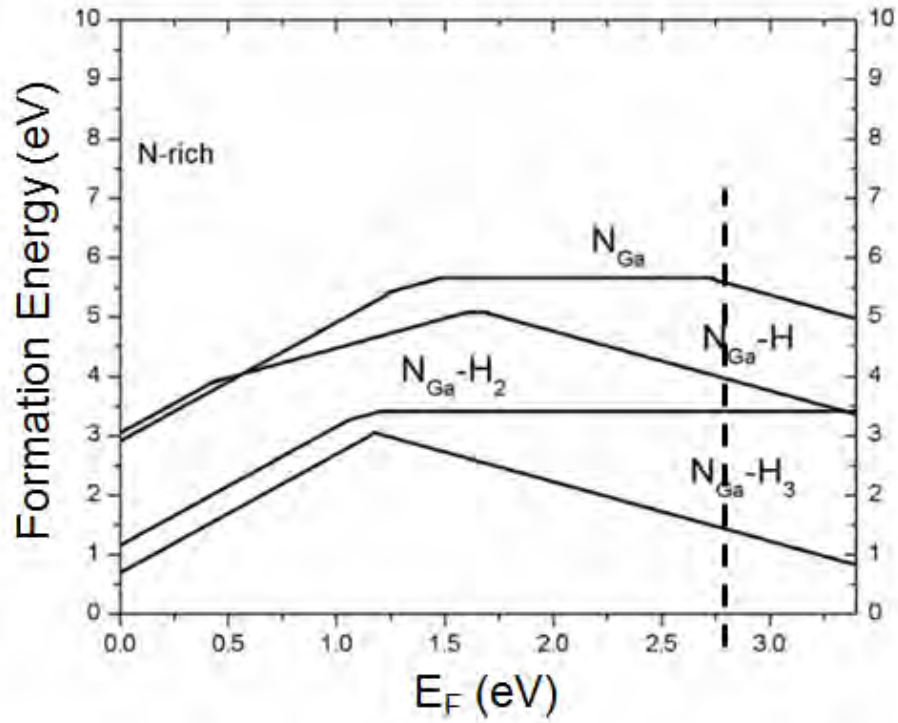


Fig. 4.6. Formation energy of hydrogenated N-anti-sites in GaN bulk. [46]

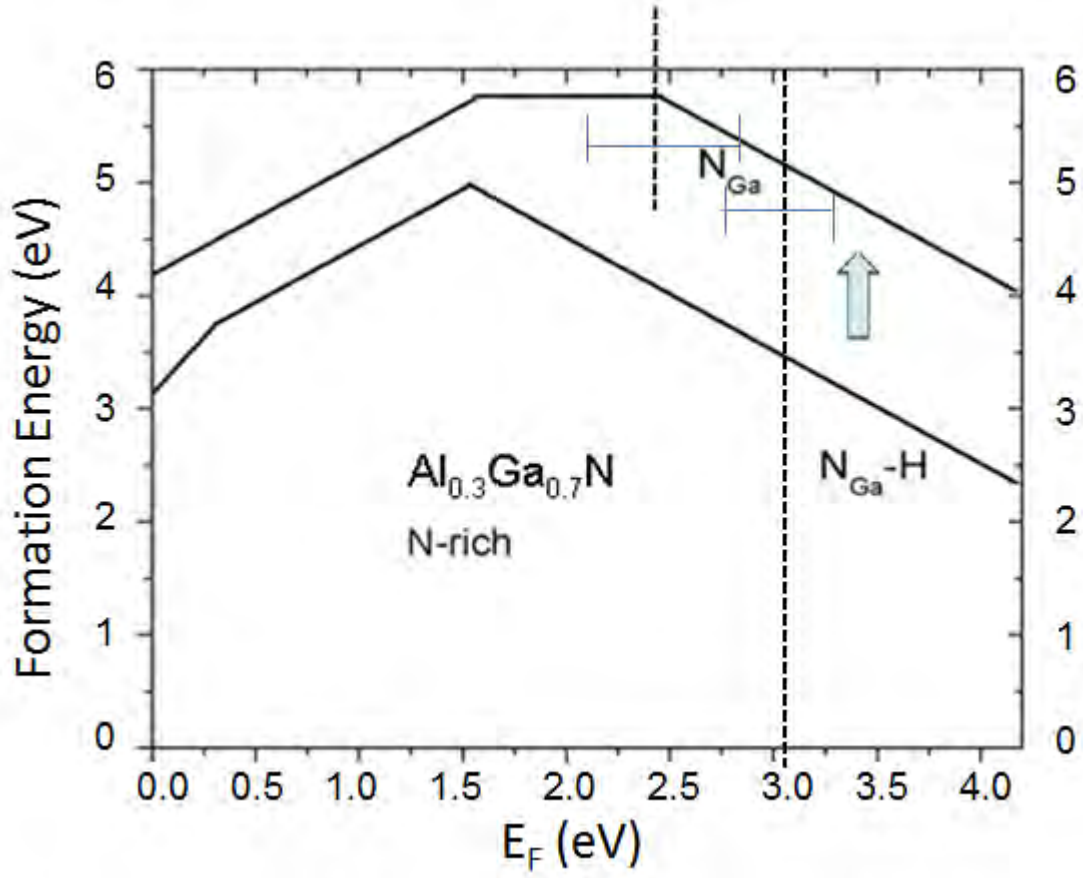


Fig. 4.7. Formation energy of hydrogenated N-anti-sites in $\text{Al}_{0.3}\text{Ga}_{0.7}\text{N}$. [47]

During stress, $E_c - E_F = \sim 1$ eV in the AlGaIn barrier (Fig. 4.8). Two-dimensional numerical simulations using the Synopsys DESSIS simulator show that the hot electrons have an average energy of 1.5 eV when the device is biased at $V_G = -5$ V and $V_{DS} = 20$ V. The high energy tail of this electron distribution lies at an energy of ~ 3 eV. The hot electrons can remove a hydrogen atom from a doubly hydrogenated Ga vacancy, which has a charge state of “-1”. The resultant singly hydrogenated Ga vacancy has a charge state of “-2”. The negative charge causes the pinch-off voltage to shift positively after stress. Moreover, because the singly-hydrogenated vacancy is doubly negatively charged, it naturally exhibits a larger Coulomb scattering tail than the doubly hydrogenated defect. This leads to reduced mobility, causing the peak g_m to decrease,

as shown in Fig. 4.1. In ammonia-rich devices, a hot electron can knock off a hydrogen atom from a triply hydrogenated N-anti-site, which has a charge state of “-1”, to form a doubly hydrogenated complex having a charge state of “0”. This change in charge state from “-1” to “0” reduces the acceptor-like nature of the traps, shifting the pinch-off voltage negatively in ammonia-rich devices. Also, the charge state of the hydrogenated anti-site formed during electrical stress is lower than its initial charge state. The lower Coulomb scattering causes the peak g_m degradation to be lower in the NH_3 -rich case compared to the N-rich case.

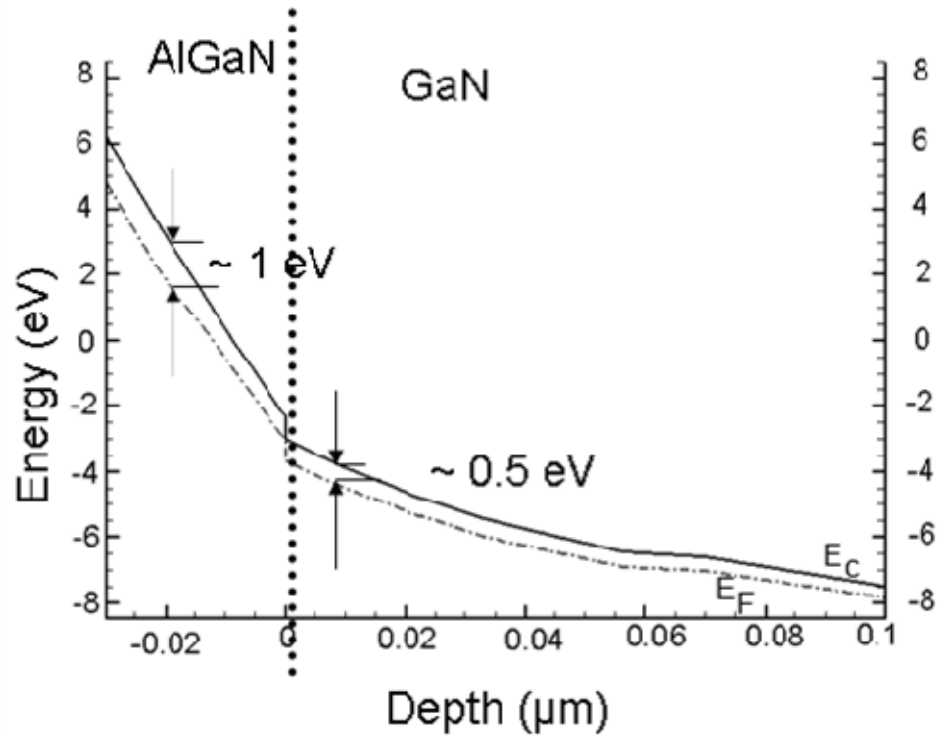


Fig. 4.8. Energy band diagram showing E_c and E_f in the AlGaIn barrier and the GaN bulk during stress conditions. [47]

4.4 Conclusion

The nature of hot electron degradation in AlGaIn/GaN HEMTs is different for samples grown under Ga-rich, N-rich, and NH_3 -rich conditions. The devices grown under Ga-rich conditions degrade the least after hot electron stress. The pinch-off voltages of devices grown in NH_3 -rich conditions shift more after stress than those of devices grown under N-rich and Ga-rich conditions. We have performed a theoretical analysis that shows that hydrogenated Ga-vacancies and hydrogenated N-anti-sites play key, process-dependent roles in determining the amount of hot electron degradation in AlGaIn/GaN HEMTs. These experimental and theoretical results show that different defects are dominant in AlGaIn/GaN HEMTs grown in Ga- and N-rich conditions and in GaN grown in NH_3 -rich conditions.

CHAPTER 5

RF STRESS INDUCED DEGRADATION IN GaN HEMTs

GaN HEMTs are often used as power amplifiers. The analysis of the small signal and large signal characteristics of the devices are of paramount importance. The Ga-rich, N-rich, and NH_3 -rich devices are first characterized in terms of their small signal and large signal performance parameters. Then they are subjected to RF stress and their DC and RF performances are compared with the pre-stress characteristics which were detailed in Chapter 3. The experiments were carried out at Cornell University.

5.1 Experiments

The devices grown under Ga-rich, N-rich, and NH_3 -rich conditions were subjected to RF stress at a frequency of 10 GHz. The input power P_{in} was set to 3dB compression point. The quiescent point was set differently for the Ga-rich, N-rich, and NH_3 -rich cases. The quiescent point was chosen around the gate voltage at which peak unity gain frequency f_T was obtained. The small signal measurements for S-parameters for f_T extraction were done before and after stress. Load pull measurements were also done before and after stress.

5.2 DC and small signal performance

Figs. 5.1-5.3 show the DC performance characteristics of Ga-rich devices before and after stress. During stress, the device was biased at $V_G = -4.5$ V and $V_D = 20$ V. The I_D - V_D , I_D - V_G

and I_G - V_G characteristics show that there has been minimal change in pinch-off voltage and saturation current after stress. However, the gate current decreases slightly after stress.

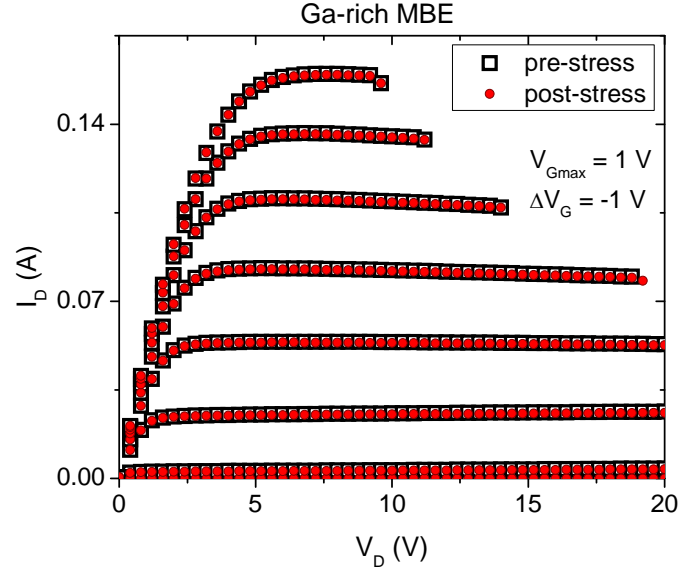


Fig. 5.1. I_D - V_D curves for a Ga-rich HEMT, before and after RF stress.

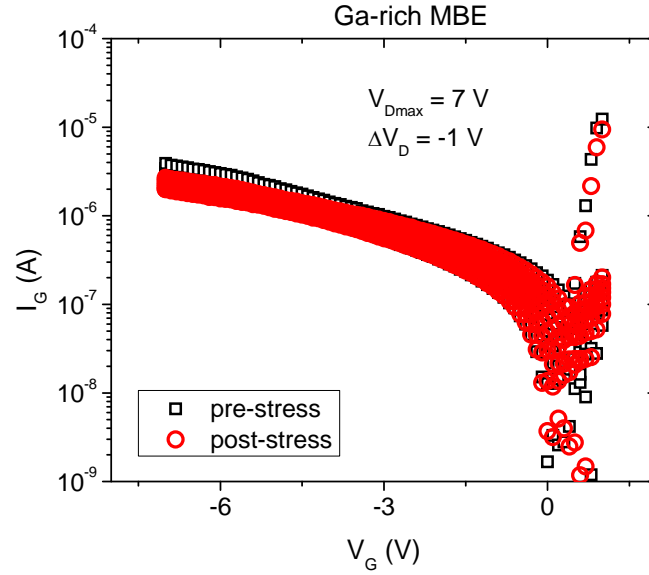


Fig. 5.2. I_G - V_G curves for a Ga-rich HEMT, before and after RF stress.

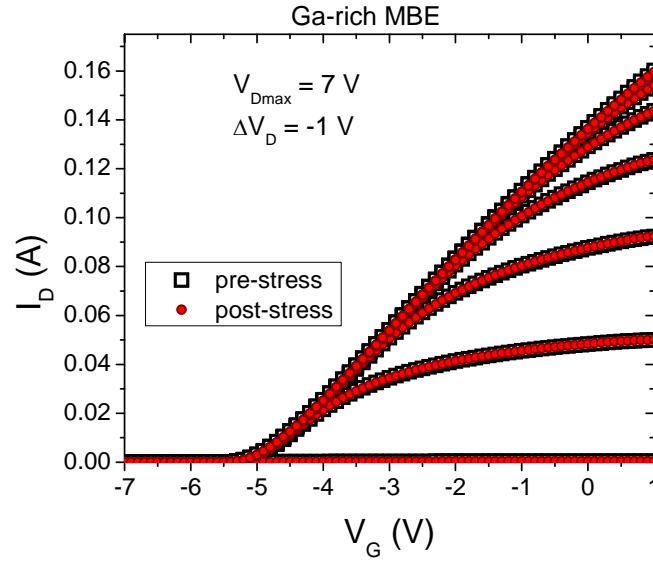


Fig. 5.3. I_D - V_G curves for a Ga-rich HEMT, before and after RF stress.

Fig. 5.4 shows the unity gain frequency f_T and maximum oscillation frequency f_{MAX} for Ga-rich devices before and after RF stress. Although there is a tangible degradation in f_T and f_{MAX} , it is not substantial (only $\sim 2\%$ change).

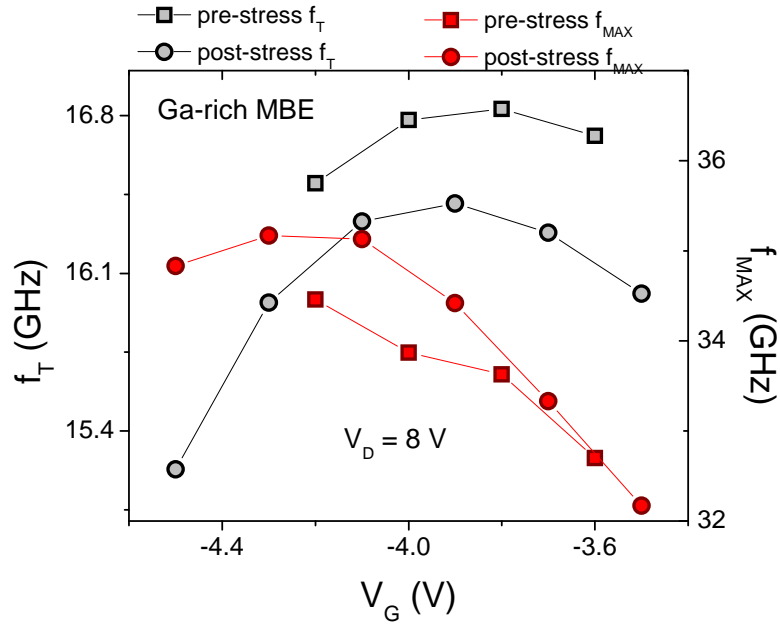


Fig. 5.4. f_T and f_{MAX} for a Ga-rich device.

Fig. 5.5-5.7 shows the DC characteristics of a N-rich device. The device was stressed at $V_G = -1.5$ V and $V_D = 20$ V. There is a slight negative shift in pinch-off voltage after stress. The gate current doubles after stress.

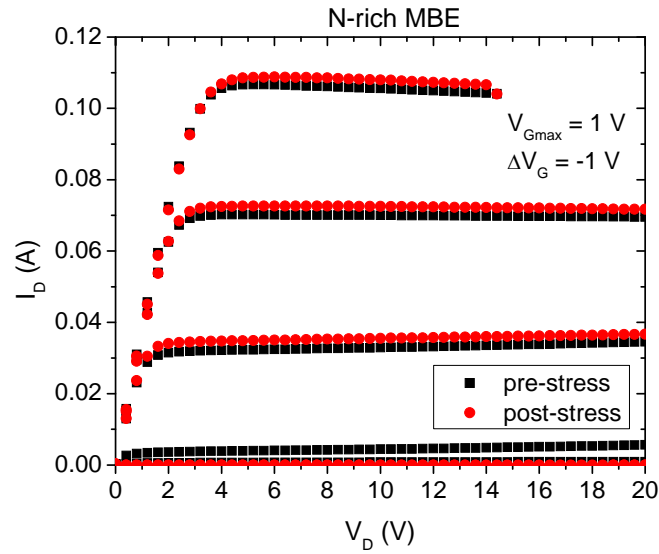


Fig. 5.5. I_D - V_D curves for a N-rich HEMT, before and after RF stress.

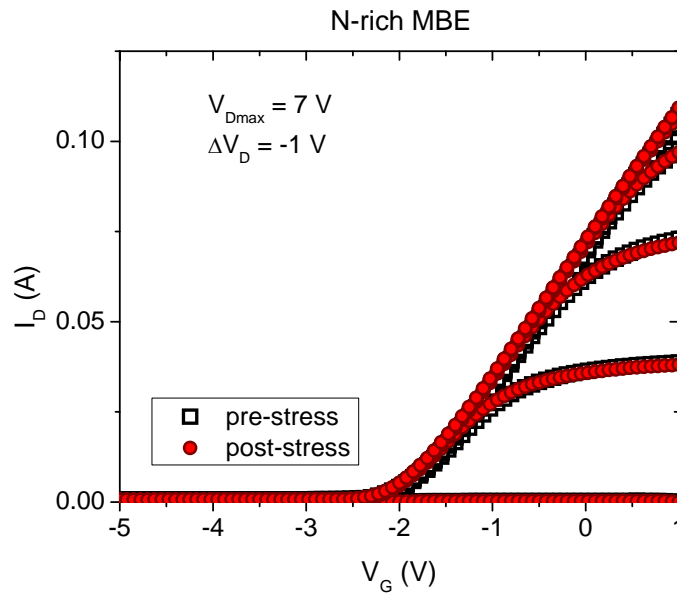


Fig. 5.6. I_D - V_G curves for a N-rich HEMT, before and after RF stress.

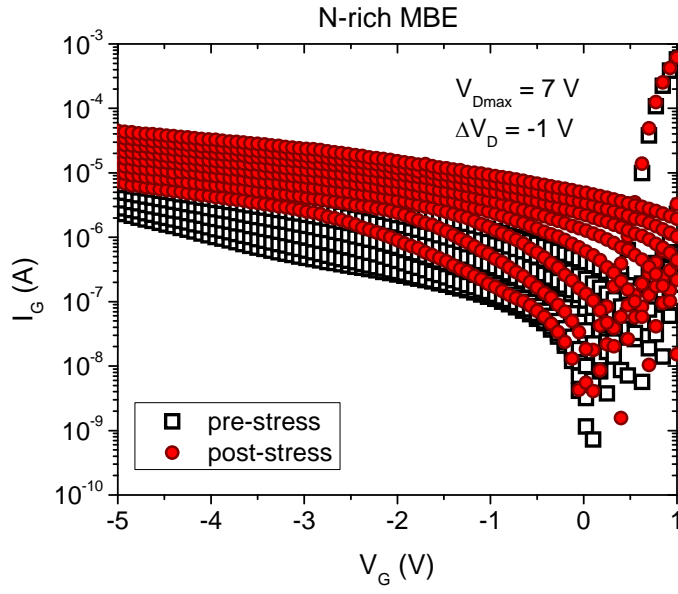


Fig. 5.7. I_G - V_G curves for a N-rich HEMT, before and after RF stress.

Fig. 5.8 shows the peak f_T and f_{MAX} of the N-rich device. The f_T and f_{MAX} shift negatively, mostly due to the threshold shift. The f_T degrades by $\sim 2\%$, and f_{MAX} increases by 3% after stress.

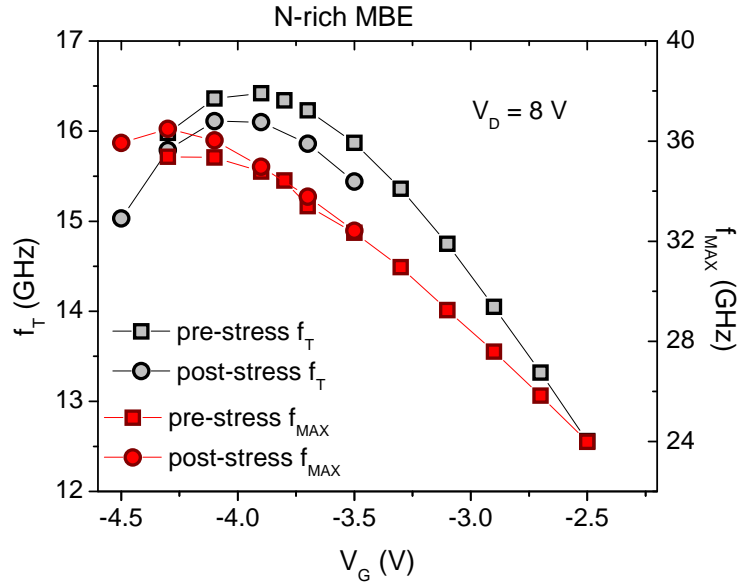


Fig. 5.8. f_T and f_{MAX} for a N-rich device.

Fig. 5.9-5.11 shows the DC characteristics of the NH_3 -rich device. The device was stressed at a gate voltage $V_G = -0.6$ V and $V_D = 20$ V. Again, there is no shift in pinch-off voltage and saturation current, but the gate current increases substantially after stress.

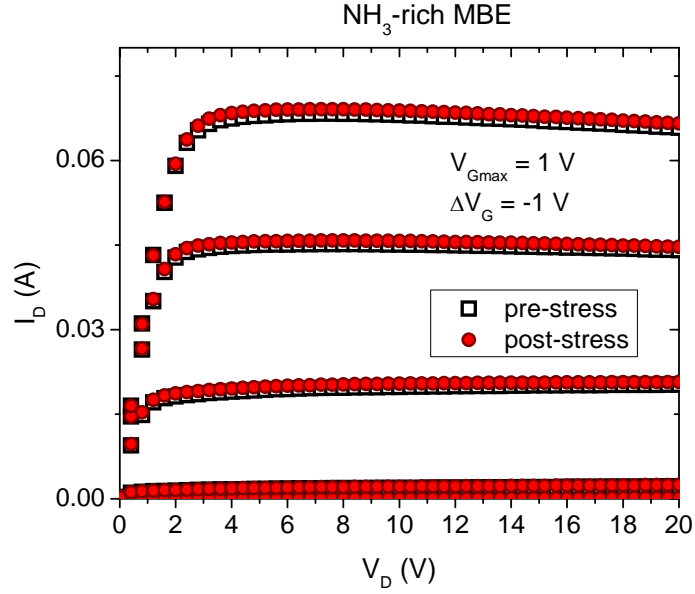


Fig. 5.9. I_D - V_D curves for an NH_3 -rich HEMT, before and after RF stress.

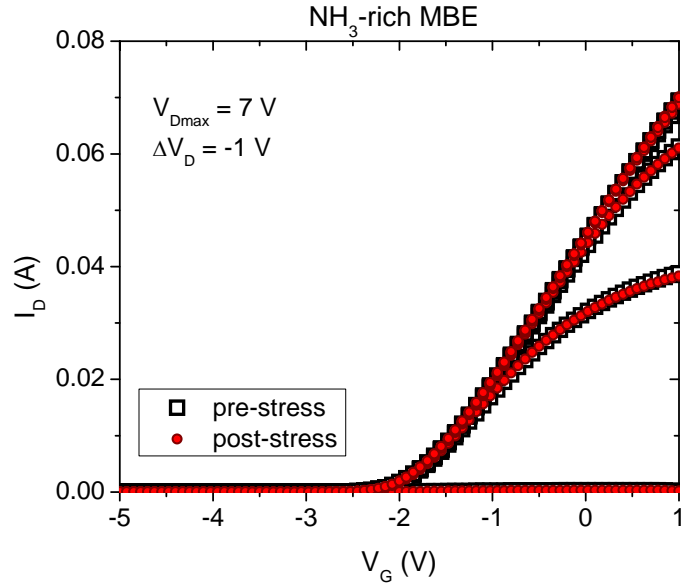


Fig. 5.10. I_D - V_G curves for an NH_3 -rich HEMT, before and after RF stress.

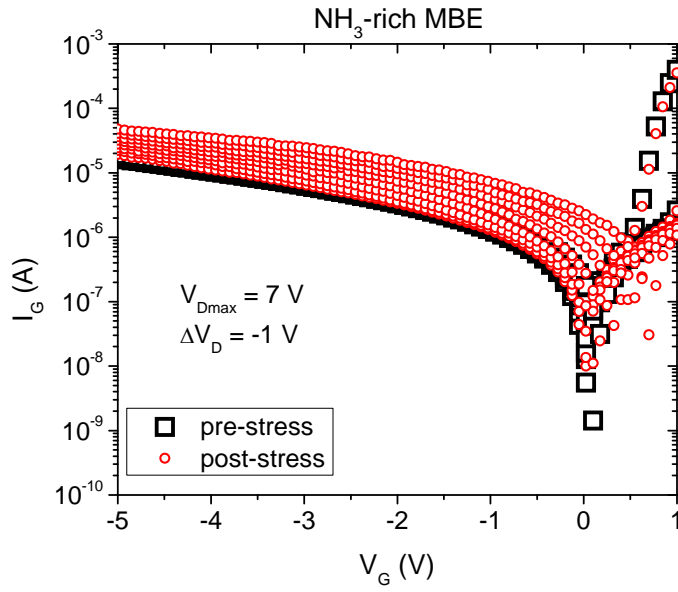


Fig. 5.11. I_G - V_G curves for an NH_3 -rich HEMT, before and after RF stress.

Fig. 5.12 shows the f_T and f_{max} of the NH_3 -rich device before and after stress. f_T increases by 2.5%, while f_{MAX} increases by ~5%. Thus, ammonia-rich devices show the greatest amount of degradation due to RF stress among the three kinds of devices studied here.

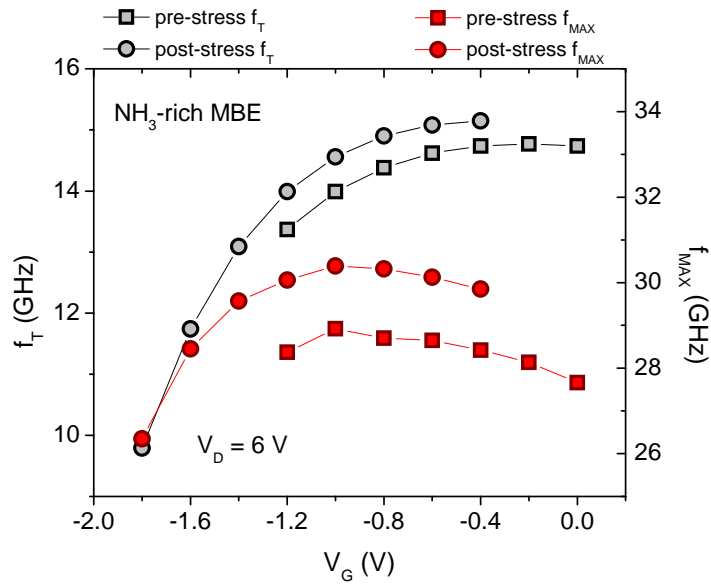


Fig. 5.12. f_T and f_{MAX} for an NH_3 -rich device.

5.3 DC vs. RF transconductance degradation

We compare the drop-off in transconductance when the HEMT is operated at high frequencies, before and after RF stress. In Chapter 3, we observed considerable g_m drop-off when the transistor is operated at 10 GHz, owing to trapping behavior. In Figs. 5.13-5.15, we observe that the drop-off in transconductance decreases after RF stress. The decrease in peak transconductance when the device is operated at high frequencies from DC is lower after subjecting the device to RF stress than under pre-stress conditions. This behavior has not been reported in the previous literature. It has been seen that RF stress induces new degradation modes in GaN HEMTs [1]. RF stress can cause impact ionization of carriers, and lower the RF transconductance drop-off after stress [1,49]. The increase in gate leakage current (Figs. 5.7, 5.11) can also be related to the impact ionization of carriers induced by RF stress. However, the data shown here are obtained over only two samples per device type, and further investigation needs to be done to understand the mechanisms responsible.

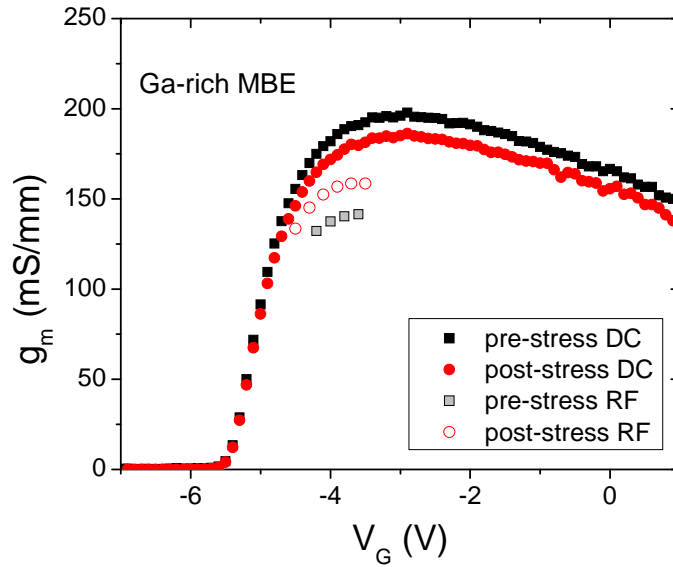


Fig. 5.13. g_m drop-off before and after RF stress for Ga-rich device.

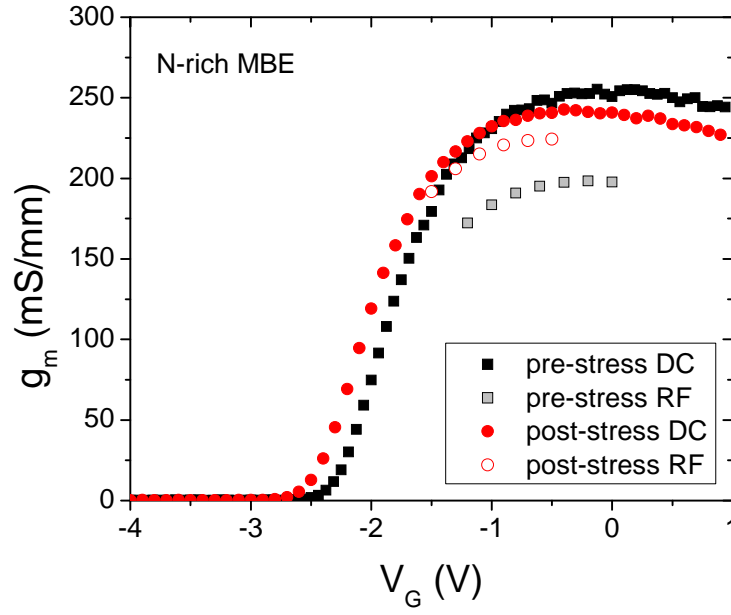


Fig. 5.14. g_m drop-off before and after RF stress for N-rich device.

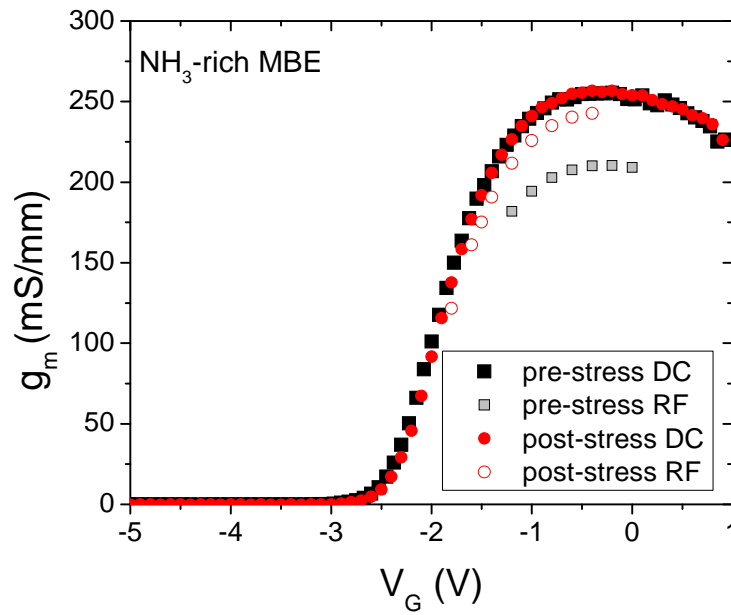


Fig. 5.15. g_m drop-off before and after RF stress for NH₃-rich device.

5.4 Large signal performance

Figs. 5.16-5.18 show the results of the load pull measurements, as described in Chapter 3, before and after stress. The quiescent drain voltage was fixed at 20 V during the large signal measurements. The quiescent gate voltage was -4.5 V, -1.5 V and -0.6 V for Ga-rich, N-rich, and NH_3 -rich devices, respectively. The frequency is 10 GHz. The input power P_{in} was swept till a gain compression of 4.5 dB was observed in the output power P_{out} . The power added efficiency (PAE) decreases slightly in all three cases after stress. The devices have a pre-stress PAE of $\sim 20\%$. Ga-rich devices show a much lower PAE of $\sim 10\%$ before stress. No apparent trapping phenomena were seen through hysteresis measurements, which could account for the low PAE.

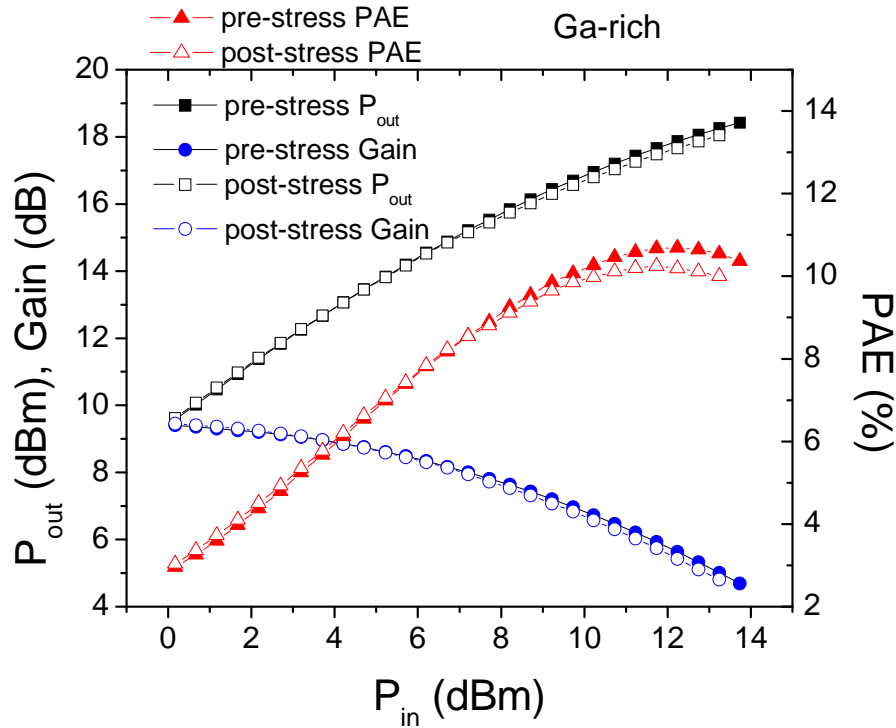


Fig. 5.16. Load-pull measurement results on Ga-rich HEMT before and after stress.

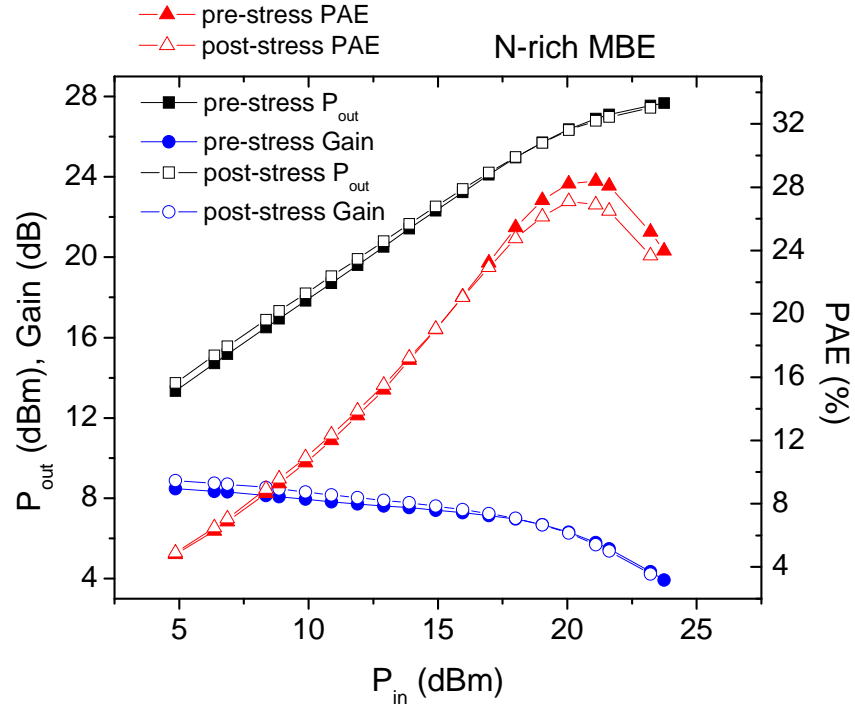


Fig. 5.17. Load-pull measurement results on N-rich HEMT before and after stress.

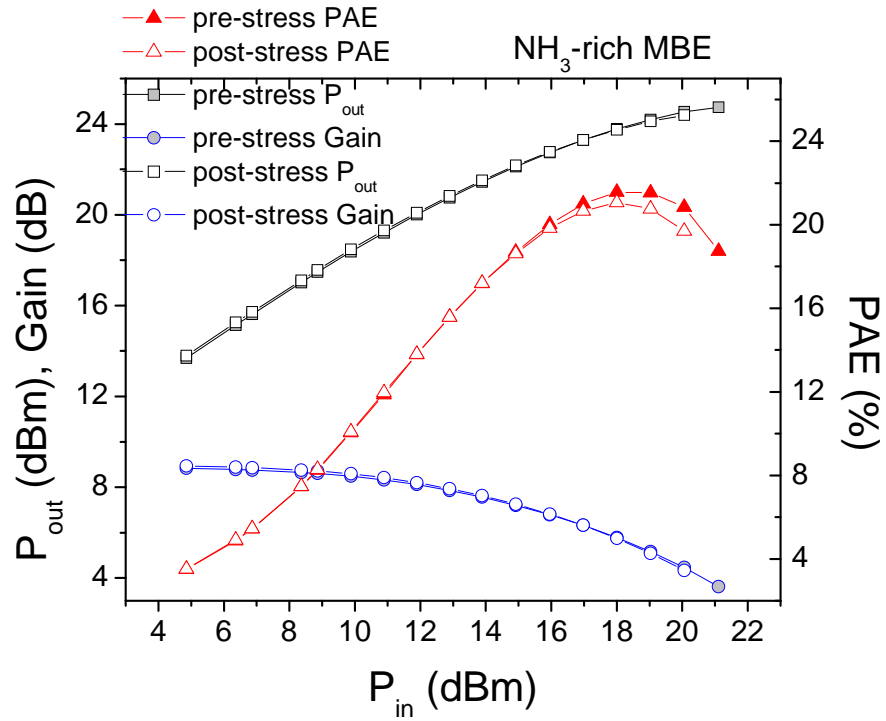


Fig. 5.18. Load-pull measurement results on NH₃-rich HEMT before and after stress.

5.5 Conclusions

The Ga-rich, N-rich, and NH_3 -rich devices show good RF reliability. The devices show minimal degradation after subjecting them to RF stress for more than 4 hours. The slight increase in leakage current, and the decrease in transconductance drop-off after RF stress indicates the impact ionization of carriers caused by RF stress, emphasizing that RF stress creates new degradation modes in GaN HEMTs compared to DC stress.

CHAPTER 6

LOW FREQUENCY $1/f$ NOISE AT ROOM TEMPERATURE

6.1 Introduction

Three mechanisms are responsible for noise in the intrinsic HEMT, which are associated with velocity fluctuation, gate leakage and traps. Scattering of electrons from the heterojunction, the lattice (phonon), and impurities cause the velocity fluctuation or diffusion noise. If the Einstein relation holds, as it does in most cases, this diffusion noise corresponds to thermal or Johnson noise [50]. Deviations occur when Einstein's equation might not hold at high field conditions near saturation, when mobility is field dependent, and even if it holds, the electron temperature is not the same as the lattice temperature. The bandwidth of this process is proportional to the inverse of the scattering time. The gate leakage noise process is associated with electron injection into the channel over the gate Schottky barrier. This noise is ideally frequency independent. The noise process due to trapping of electrons in surface states (near the gate) and/or AlGaIn/GaN interface traps (near the channel) has a $1/f^\alpha$ dependence [51]. In this work we illustrate how noise measurements can help to understand the nature of defects present in the AlGaIn/GaN HEMT [47].

6.2 Experiments

Low frequency $1/f$ noise is measured for the GaN/AlGaIn HEMTs grown using MBE under Ga-rich, N-rich, and NH_3 -rich conditions, before and after stress. The noise spectrum is obtained using a SR760 FFT Spectrum Analyzer, across a frequency range of ~ 6 Hz to ~ 400

Hz. The gate voltage is adjusted so that the noise originates from the gated portion of the channel, as will be explained in the following section. The drain voltage is maintained at 0.02 V.

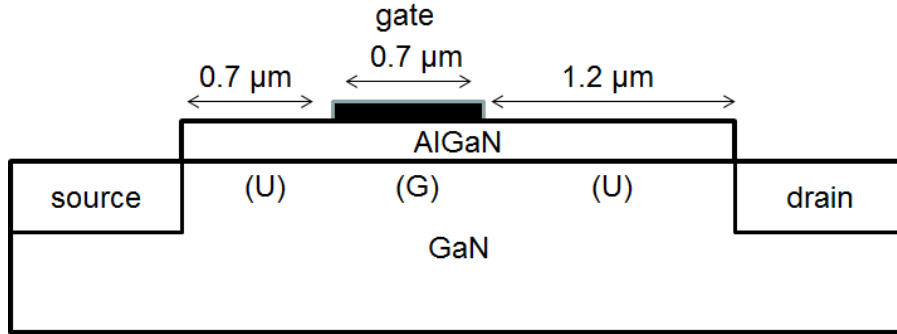


Fig. 6.1 Cross-section of a GaN HEMT, showing the gated and ungated portion of the channel.

6.3 Gate voltage dependence of S_{vd}

The low frequency noise of HEMTs originates in both the gated (G) and ungated (U) portions of the channel, as shown in Fig. 6.1. The channel resistance R_{total} comprises the resistance of the gated and the ungated portions (access regions) [52],[53]:

$$R_{total} = R_G + R_U = \frac{L_{gate} V_{off}}{Wq\mu n_{ch}(V_{GS} - V_{off})} + R_U \quad (6.1)$$

Here μ is the channel mobility, and n_{ch} is the carrier density. From the empirical relationship given in [54], we have:

$$\frac{S_V}{V^2} = \frac{S_I}{I^2} = \frac{S_R}{R^2} = \frac{\alpha}{fN} \quad (6.2)$$

Here S_{vd} is the excess drain-voltage noise power spectral density, N is the total number of carriers in the channel, f is the frequency, and α is an empirical factor often used to compare the noise of different kinds of microelectronic devices [54]. The total noise from the channel is given by:

$$S_{R_{total}} = S_{R_G} + S_{R_U} = \frac{\alpha_{ch} R_{ch}^2}{N_{ch} f} + S_{R_U} \quad (6.3)$$

When V_G is very close to the pinch-off voltage, with only a few electrons in the channel, the resistance of the gated region is greater than that of the ungated region. In such conditions, when the noise originates in the gated region, the noise in an AlGaIn/GaN HEMT is often found empirically to be proportional to $(V_G - V_{off})^{-1}$ [52]-[54]:

$$\frac{S_v}{V^2} = \frac{\alpha}{fN_{ch}}; \text{ i.e., } S_{vd} = \frac{\alpha}{fN_{ch}} V_d^2 \propto (V_G - V_{off})^{-1} \quad (6.4)$$

At slightly higher gate voltages, the electron density in the channel is sufficiently high that the resistance of the gated region is less than that of the access regions.

$$\frac{S_v}{V^2} = \frac{S_{R_{total}}}{R_{total}^2} = \frac{S_{R_G}}{R_U^2} = \frac{\alpha}{R_U^2} \frac{R_G^2}{N_{ch}f} \propto (V_G - V_{off})^{-3} \quad (6.5)$$

In the results reported here, the gate voltages are in the range such that the noise power spectral density $\propto (V_G - V_{off})^{-3}$ [52]-[54]. This ensures that the noise originates in the channel, where additional defects are created most efficiently by hot-electron stress. Figure 6.2 shows the gate voltage dependence of noise in GaN HEMTs grown under N-rich conditions. The noise was measured for $V_{DS} = 0.02$ V; $f = 10$ Hz; $S_{vd} \propto (V_G - V_{off})^{-3}$ for 0.1 V $< V_G - V_{off} < 1$ V.

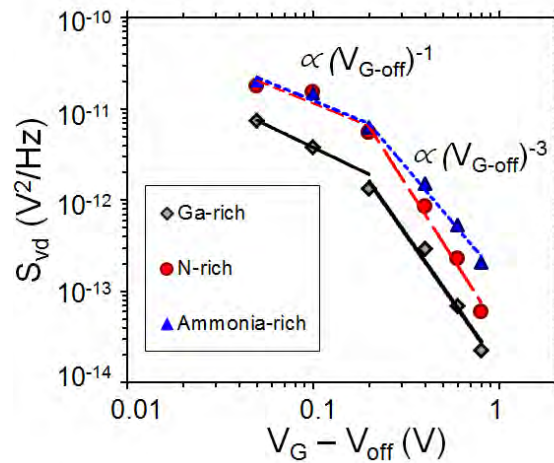


Fig. 6.2. Gate voltage dependence of excess drain voltage low frequency noise in GaN HEMTs. The noise originates from the channel. [47]

6.4. S_{vd} vs. gate leakage

Figs. 6.3-6.4 show the excess drain voltage power spectral density as a function of gate leakage in Ga-rich, N-rich, and NH_3 -rich HEMTs. Both pre-stress and post-stress measurements are shown. There is no distinct trend that separates the three kinds of devices from each other.

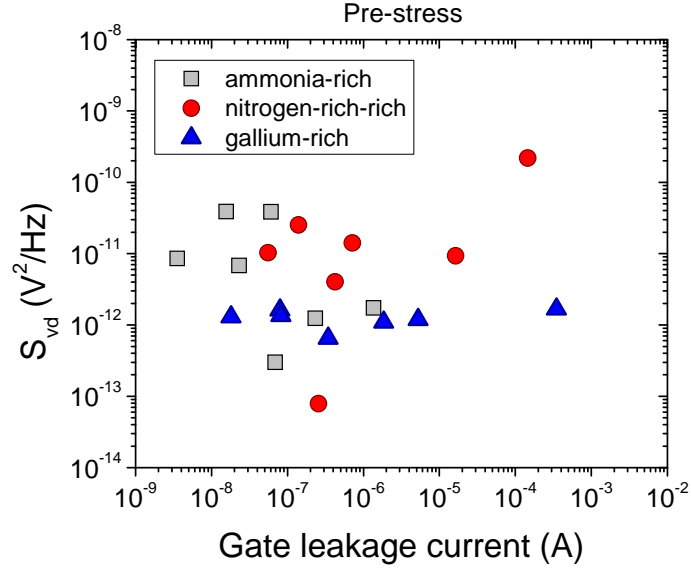


Fig. 6.3. S_{vd} vs. leakage current for Ga-rich, N-rich, and NH_3 -rich devices before stress. [47]

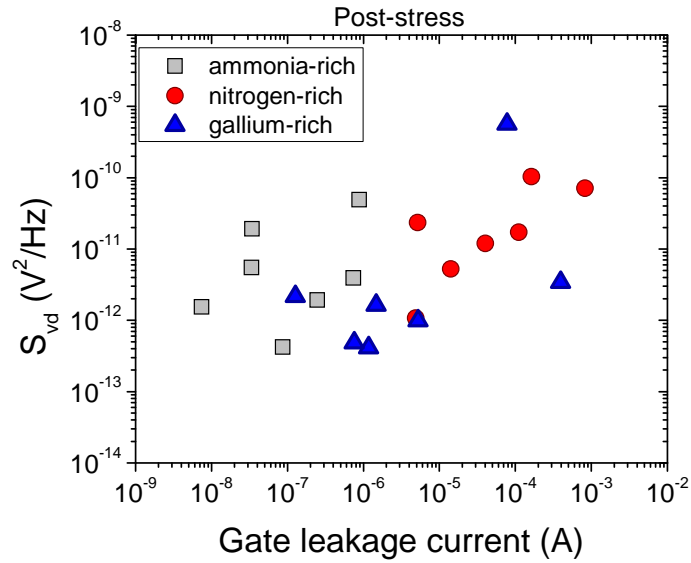


Fig. 6.4. S_{vd} vs. leakage current for Ga-rich, N-rich, and NH_3 -rich devices after stress. [47]

The noise increases with increasing leakage current after stress for all three device types, as shown in Fig. 6.5. The increase in noise with increasing gate leakage suggests that the traps contributing to noise are present in the AlGa_N barrier [55]. The electric field is the highest in the AlGa_N barrier during the stress conditions. The energy band diagram in Fig. 4.8 shows that the Fermi level is ~ 1 eV below E_c in the AlGa_N during stress, while it is only ~ 0.5 eV below E_c in the bulk GaN. Thus, defect levels in the AlGa_N that lie approximately 1 eV below E_c can contribute to the noise generated in the channel of these devices. However, we also cannot rule out a surface origin for the defects that cause the $1/f$ noise in these devices. Indeed, it is quite possible that both surface and bulk defects [56] may contribute to the noise before and/or after stress.

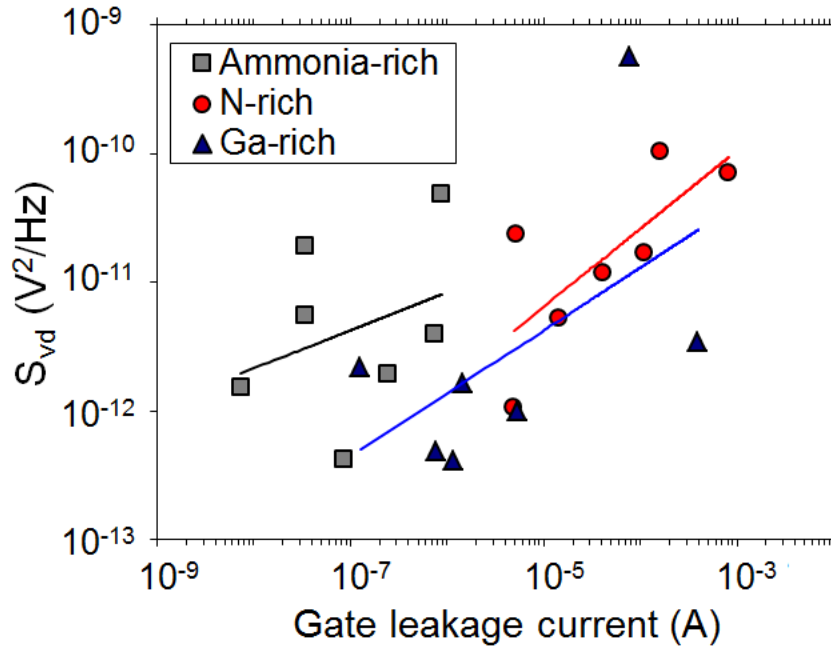


Fig. 6.5. Excess drain-voltage low-frequency noise-power spectral density as a function of gate leakage, after stress. The increase in noise with increasing leakage current shows that traps formed in AlGa_N barrier are responsible for the noise. [47]

6.5 S_{vd} vs. frequency

Fig. 6.6 shows the comparison of post-stress noise with pre-stress noise. There is not much correlation between the stress-related increase or decrease of noise with the growth condition of the devices.

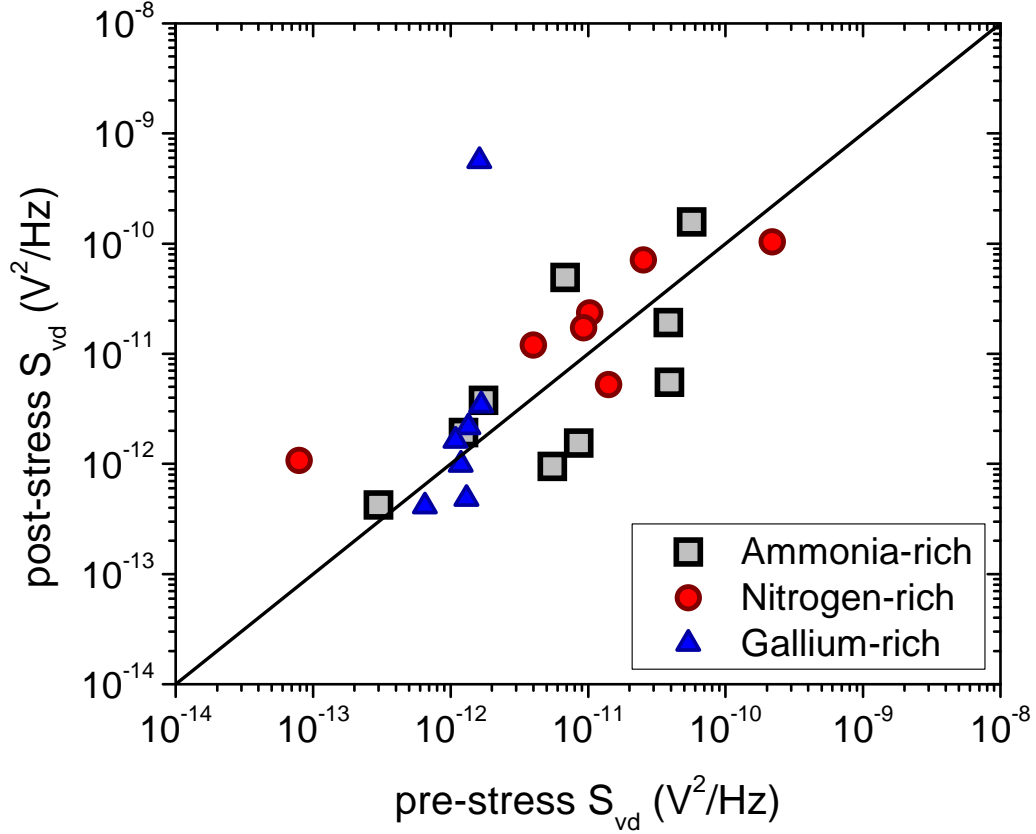


Fig. 6.6. Post-stress vs. pre-stress noise for Ga-rich, N-rich, and NH_3 -rich devices, $f = 10$ Hz. Noise measurements are performed at $V_G - V_{off} = 0.2$ V, $V_{DS} = 0.02$ V.

Fig. 6.7 shows the excess drain voltage noise power spectral density as a function of frequency before and after stress, for devices grown under Ga-rich, N-rich, and NH_3 -rich conditions. The measurements were taken for $V_G - V_{off} = 0.2$ V, and $V_{DS} = 0.02$ V. The noise in the Ga-rich and N-rich devices typically increases slightly after stress. For some ammonia-rich

devices (Fig 6.7 (c)), there is an increase in noise after stress, while in others (Fig. 6.7 (d)), there is a decrease in post-stress noise.

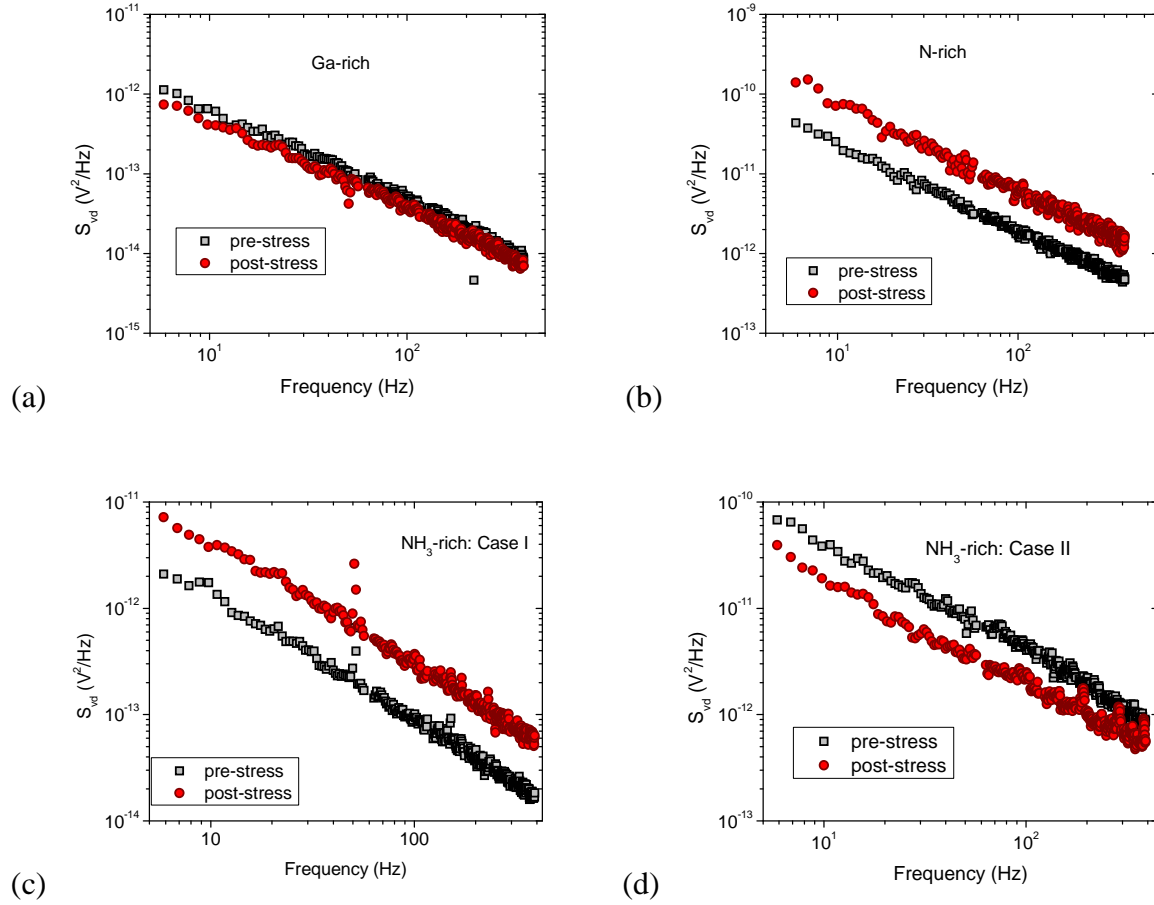


Fig.6.7 S_{vd} vs. frequency for (a) Ga-rich, (b) N-rich, and (c) and (d) NH_3 -rich HEMTs. [47]

6.6 Point defects responsible for $1/f$ noise

During the noise measurements, the gate voltage is varied from $V_{off} + 0.2$ V to $V_{off} + 0.8$ V. $E_c - E_f \sim 1$ eV close to pinch-off in the AlGa N barrier, and 0.5 eV in the Ga N barrier. DFT calculations show that there are no thermodynamic transition levels related to the hydrogenated Ga vacancies near the Fermi level during the noise measurement. Thus, Ga vacancies, though

responsible for the shift in pinch-off voltage of the devices after stress [45], do not contribute significantly to changes in the $1/f$ noise magnitudes in these devices. Hydrogenated N-anti-sites have a transition level near the location of the Fermi level in the AlGaN barrier and the GaN bulk, during the noise measurements. These defects, which are responsible for the negative shift in the pinch-off voltage of ammonia-rich devices, also contribute to the increase in $1/f$ noise after stress.

Fig. 6.8 shows the formation energy of singly hydrogenated and dehydrogenated Ga-N divacancies in GaN and AlGaN. These defects also have a transition level close to the location of the Fermi level in AlGaN. The hydrogenated divacancy contributes to noise before stress. After stress, the hydrogen can be removed, and the dehydrogenated divacancy can still contribute to the noise. Bare nitrogen vacancies also have a transition level close to the Fermi level during noise measurements. However, the formation energy of a hydrogenated nitrogen vacancy is higher than the bare nitrogen vacancy [46]. The bare nitrogen vacancy can contribute to noise before and after stress.

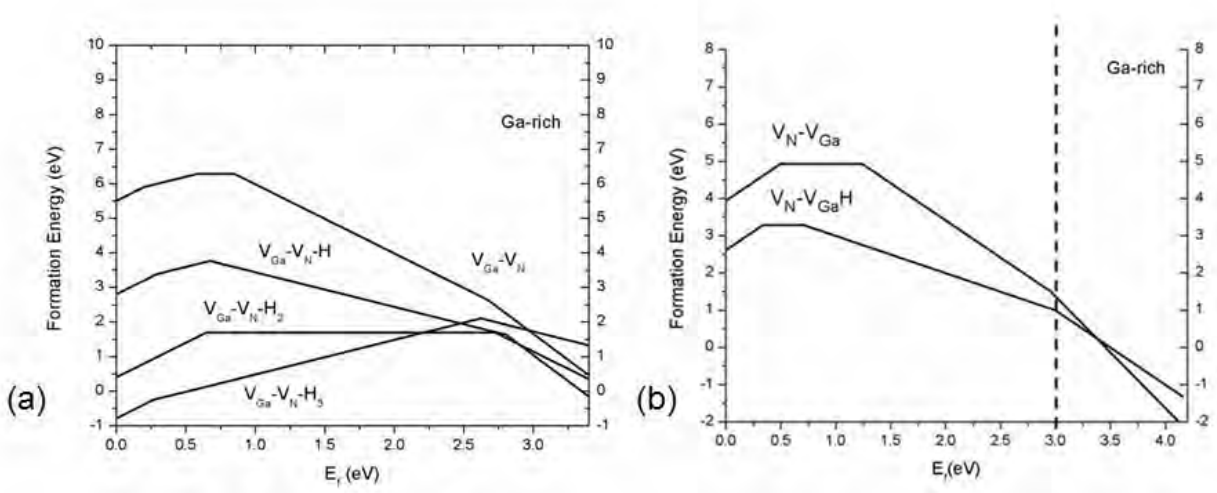


Fig. 6.8. Formation energy of hydrogenated Ga-N-divacancies in (a) GaN, and (b) $Al_{0.3}Ga_{0.7}N$. [47]

The decrease in noise noticed in some devices can be attributed to the dehydrogenation of substitutional carbon impurities at nitrogen sites. Hydrogenated C on an N site shows a change in charge state ~ 1.0 eV below the conduction band, as shown by the change of slope of the defect formation energy curve in Fig. 6.9. During the low-frequency noise measurements, the gate voltage is close to $V_{pinch-off}$, and E_f is ~ 1.0 eV below E_c . After hydrogen is removed during electrical stress by hot electrons, the substitutional C does not change its charge state near E_f during the measurement. Therefore, the noise can decrease after stress. So, whether the noise increases or decreases with stress can be a strong function of the dominant defect type present in the region of the channel in which defects form during hot carrier stress.

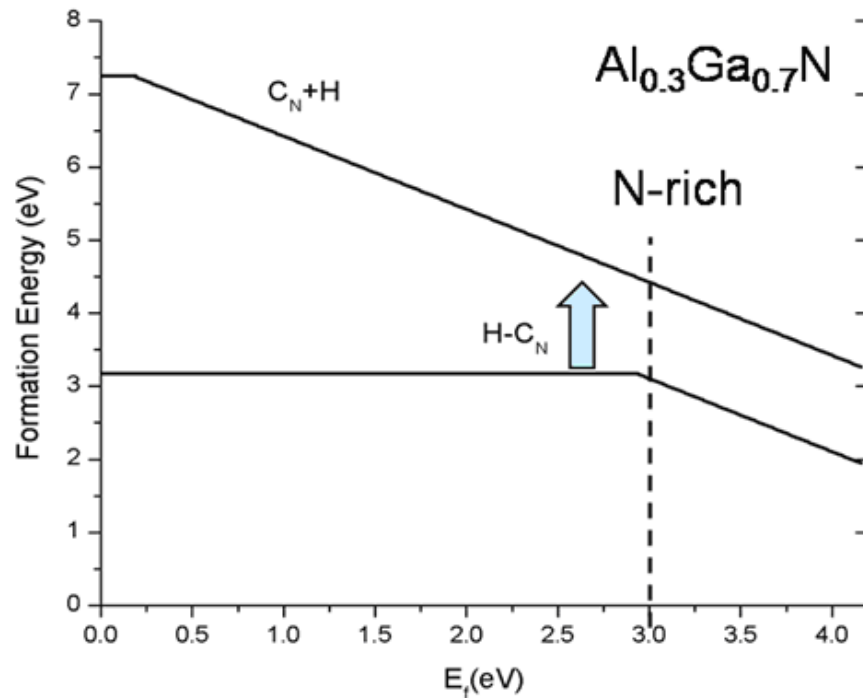


Fig. 6.9. Formation energy of substitutional carbon in N-site as a function of Fermi energy in AlGaIn. The dashed line shows the position of the Fermi level in the AlGaIn barrier during the stress and during noise measurement. [57]

6.7 Conclusion

Noise originating in the channel increases after stress for some devices grown under Ga-rich, N-rich, and NH_3 -rich conditions, but decreases in others because of the dehydrogenation of different defects present in the AlGaIn layer. The increase in $1/f$ noise with increasing leakage current confirms that defects in the AlGaIn barrier contribute to the noise. The positive shift in pinch-off voltage in Ga-rich and N-rich devices after stress is caused by the dehydrogenation of hydrogenated Ga vacancies in the GaN bulk and the AlGaIn barrier. These Ga vacancies do not contribute significantly to the increase in $1/f$ noise magnitude of the devices, because they lack a thermodynamic transition level close to where the Fermi level is located in the AlGaIn barrier. The negative shift in pinch-off voltage in ammonia-rich devices is attributed to the dehydrogenation of hydrogenated N anti-sites in the GaN bulk and the AlGaIn barrier. These defects have a transition level close to the Fermi level during noise measurements, and contribute to the increase in noise after stress. Hydrogenated Ga-N divacancies before stress, and dehydrogenated divacancies after stress, can contribute to the observed $1/f$ noise. A decrease in noise magnitude observed in some devices can be attributed to the dehydrogenation of substitutional carbon impurities present in the AlGaIn barrier.

CHAPTER 7

NOISE SPECTROSCOPY ON GaN HEMTs

7.1 Introduction

Low frequency $1/f$ noise measurements have been used to help understand the nature of defects that limit the reliability of semiconductor devices [58,59]. While $1/f$ noise measurements have been performed on GaN transistors, the microstructure of the defects that lead to the noise is largely unknown [59,60]. In this work, we have performed $1/f$ noise measurements on GaN high-electron-mobility transistors (HEMTs) grown using molecular beam epitaxy (MBE) and metallorganic chemical vapor deposition (MOCVD) techniques. Temperature-dependent noise measurements show that nitrogen-rich devices exhibit a noise spectrum that differs from the noise spectrum of gallium-rich MBE-grown and MOCVD-grown devices. The noise follows the Dutta-Horn model [61] for all growth conditions, indicating that the noise is due to thermally activated random processes. Two peaks are observed in the energy distribution of the nitrogen-rich devices, derived from the temperature dependence of the noise. One is at ~ 0.2 eV, and the other is above ~ 1 eV. Only the ~ 0.2 eV peak is observed for Ga-rich-MBE and MOCVD-grown devices. First-principles calculations allow us to associate the observed 0.2 eV peak with the reconfiguration of oxygen DX-like centers from a negatively charged to a neutral state. The peak above ~ 1 eV that is observed only under N-rich growth conditions is attributed to the $-1/0$ charge state transition level and the reconfiguration energy of the nitrogen antisite.[62,46] These results suggest a broad role in $1/f$ noise for defects that reconfigure upon charge-state change.

[63]

7.2 Experiments

Noise measurements are performed on GaN HEMTs grown using MBE under Ga-rich, N-rich, and NH₃-rich conditions, and grown using MOCVD. These devices have been described in the previous chapters. The temperature is varied from 85 K to 450 K during the measurements, to obtain the energy spectrum of the defects contributing to noise. Measurements were performed under high current and low current conditions. For the high current noise measurements, the gate voltage was fixed at $>V_{\text{off}} + 1 \text{ V}$, $V_D > 0.09 \text{ V}$, and for the low current noise measurements, the gate voltage was fixed at $\leq V_{\text{off}} + 0.2 \text{ V}$, $V_D = 0.02 \text{ V}$.

The devices grown by Ga-rich, N-rich, and NH₃-rich MBE and MOCVD were subjected to stress under high field conditions, typically at $V_D = 20 \text{ V}$, and V_G slightly above the pinch-off voltage. Noise measurements are performed again after stress, across 85 K to 450 K. The noise is measured under low current conditions, at $V_G - V_{\text{pinch-off}} = 0.1 \text{ V}$, and $V_D \leq 0.05 \text{ V}$, and under high current conditions, at $V_G - V_{\text{pinch-off}} = 1.8 \text{ V}$, $V_D = 0.15 \text{ V}$.

7.3 Temperature-dependence and microscopic origin of pre-stress $1/f$ noise

Fig. 7.1 shows the temperature dependence of the drain current as a function of gate voltage for a Ga-rich MBE-grown HEMT. The pinch-off voltage does not vary significantly with temperature, indicating that the sheet charge density remains approximately constant over the range of experimental conditions employed in this study [59]. Noise originating in the channel follows a $1/f^\gamma$ dependence, as shown in Fig. 7.2, where:

$$\gamma = -\frac{\partial \ln S}{\partial \ln f} \quad (7.1)$$

with γ close to unity, as commonly observed for low-frequency noise in GaN/AlGaN HEMTs [59,60,64]. The noise power spectral density is shown at 85 K, 300 K, and 450 K. The noise magnitude does not depend strongly on the temperature.

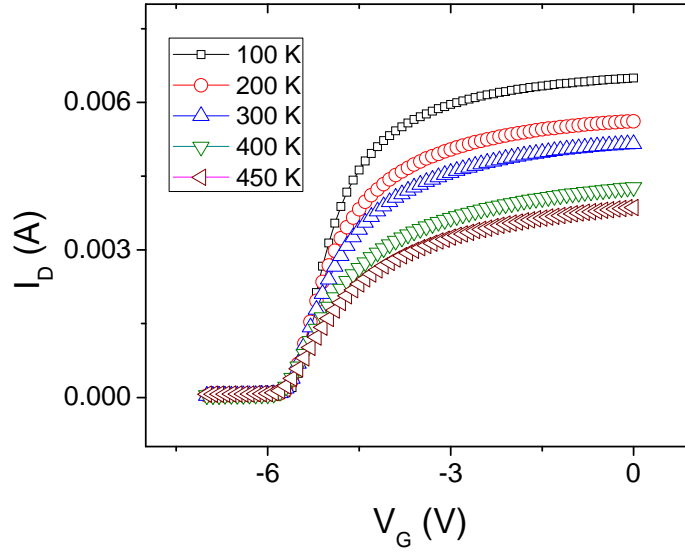


Fig.7.1. Temperature dependence of the I_D - V_G curves for a Ga-rich MBE-grown HEMT. [63]

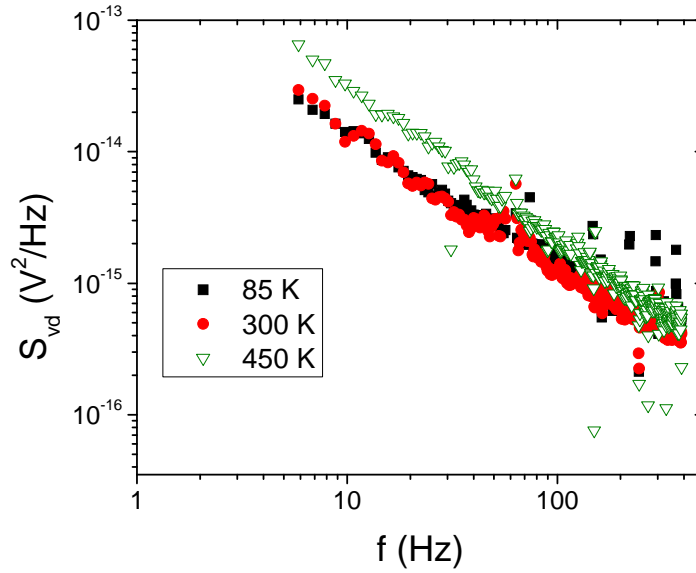


Fig. 7.2. S_{vd} vs. f for a N-rich MBE-grown HEMT. [63]

Fig. 7.3-7.5 show the frequency dependence of the noise power spectral density γ as a function of temperature for (a) N-rich, (b) Ga-rich, and (c) MOCVD-grown devices. At least 3 devices of each kind were tested with similar responses. The frequency and temperature dependence of noise are related via the following equation [61]:

$$\gamma(\omega, T) = 1 - \frac{1}{\ln(\omega\tau_0)} \left(\frac{\partial \ln S(\omega, T)}{\partial \ln T} - 1 \right) \quad (7.2)$$

This equation assumes that no new defects are created or annealed while the temperature is swept from 85 K to 450 K [61]. The calculated and experimental values of γ match closely, indicating that the noise follows the Dutta-Horn model.

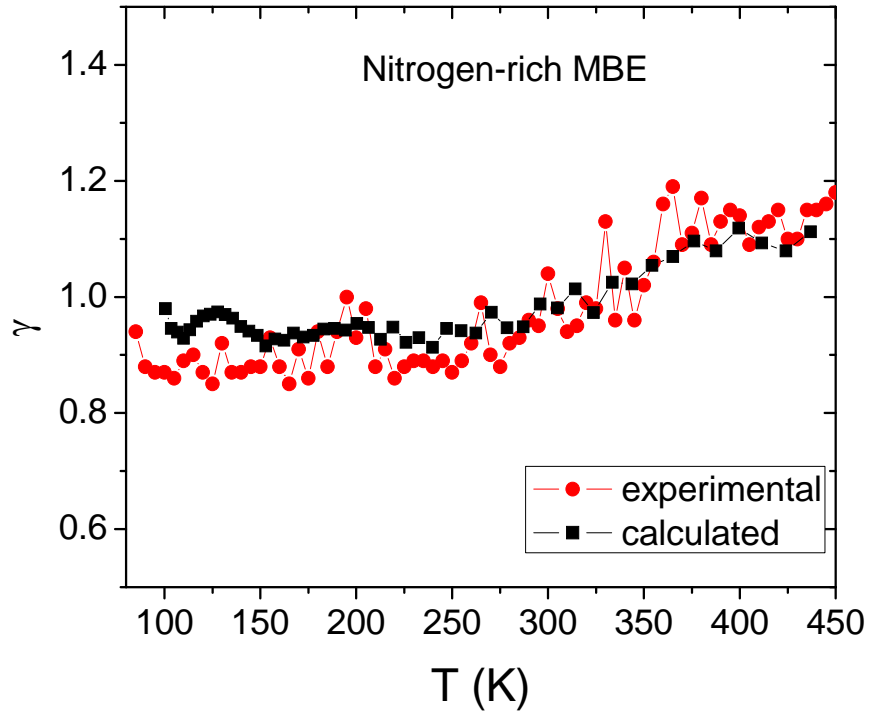


Fig. 7.3. Frequency exponent of noise power spectral density as a function of temperature for N-rich MBE-grown devices. [63]

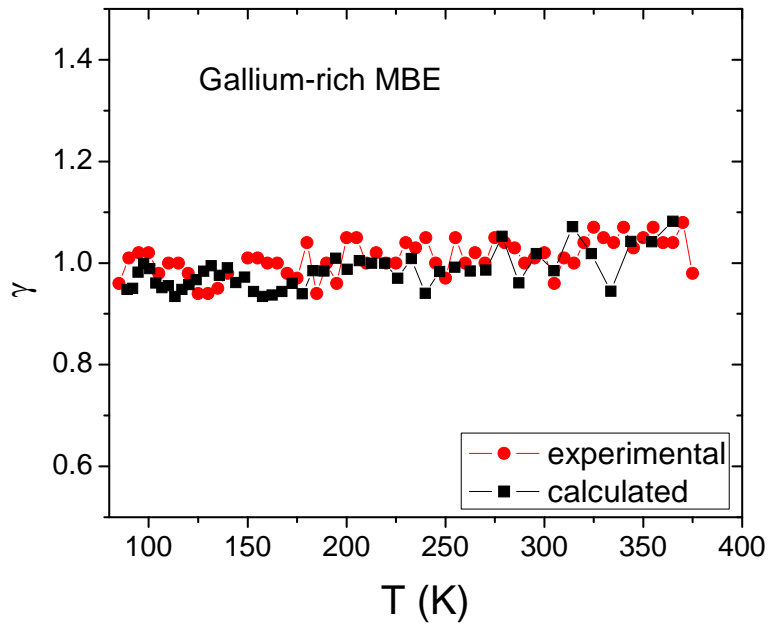


Fig. 7.4. Frequency exponent of noise power spectral density as a function of temperature for Ga-rich MBE-grown devices. [63]

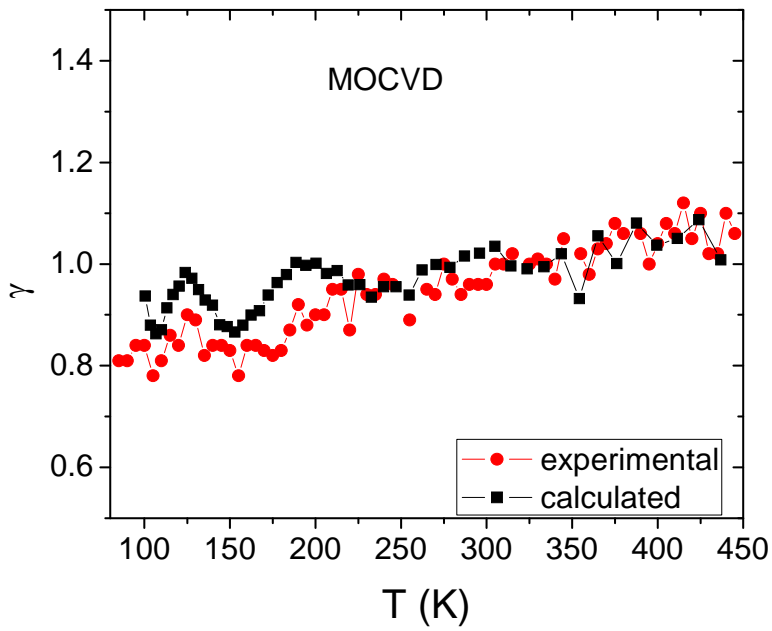


Fig. 7.5. Frequency exponent of noise power spectral density as a function of temperature for MOCVD-grown devices.[63]

The agreement between the measured noise and the Dutta-Horn model implies that noise is associated with the thermally-activated transition between states that are distributed in energy. To estimate the energy scale associated with the observed noise, we consider that noise may be observed when electron capture or emission leads to a transition between two metastable charge states of a defect, separated by an activation barrier E_0 [65], where:

$$E_0 = -k_B T \ln(\omega \tau_0) \quad (7.3)$$

and τ_0 is the attempt-to-escape frequency of a typical defect in the system.

Such a transition can be facilitated by the interaction between an electron and an optical photon, for example [65]. The rate of electron-phonon scattering is determined by electronic structure and phonon dispersion. For a hot electron, the scattering process involves emission or absorption of an optical phonon. Both electronic structure and phonon modes can be obtained using density functional theory. The scattering for an electron with energies below 2 eV is dominated by phonon emission process resulting in electron energy loss. With a defect present in the system, scattering involves the phonon modes of the present defect. Fig. 7.6 illustrates typical electron-phonon scattering rates with and without a defect in the system. Here, a Ga-vacancy and a singly hydrogenated Ga-vacancy are considered. For calculating the activation energy of the defect reconfiguration, we consider the scattering rate to be $3 \times 10^{13} \text{ s}^{-1}$ [66]. $1/f$ noise is produced as electrons from the GaN channel are captured or emitted by defect levels within a few kT of the Fermi level in the channel, which is fixed by the gate voltage at which the noise is measured.

In Fig. 7.3, the increase in γ with increasing temperature suggests that electrons from the channel can interact with defects in the AlGaIn barrier after thermal emission over the energy barrier between the GaN channel and the AlGaIn barrier layer. On the other hand, the relatively

weak dependence of γ on temperature in Fig. 7.4 may indicate that the electrons are tunneling into defects in the AlGaN barrier [67], which is a temperature-independent process.

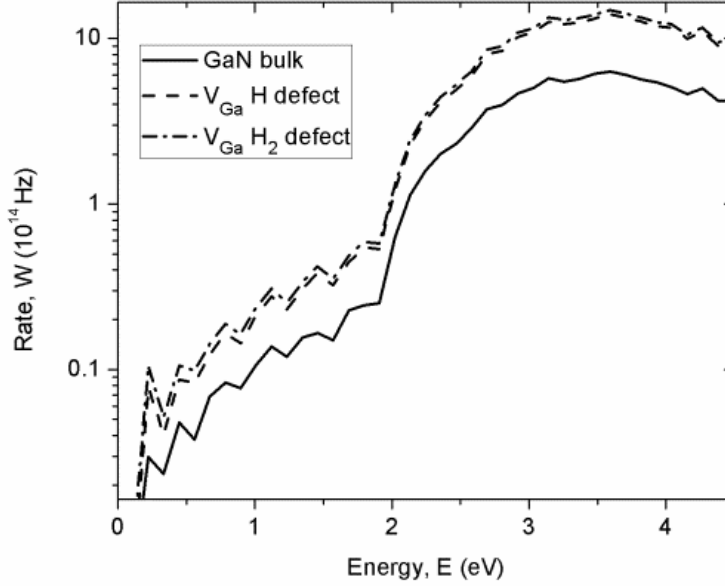


Fig. 7.6. Scattering rate of an electron is dominated by an emission of the optical phonon from a typical defect in a GaN crystal. The scattering rates correspond to phonon frequency of $f=360$ meV and $f=425$ meV for singly and doubly hydrogenated Ga vacancy (V_{Ga}) respectively. [66]

Since the noise follows the Dutta-Horn model, the activation energy distribution of defects contributing to noise in the device can be estimated as [61]:

$$D(E_0) \propto \frac{\omega}{k_B T} S(\omega, T) \quad (7.4)$$

Fig. 7.7 shows the noise power spectral density, equivalent to the activation energy distribution, as a function of temperature. The noise was measured at $V_G - V_{off} = 2.3$ V, $V_D = 0.15$ V for the N-rich device, $V_G - V_{off} = 1.8$ V, $V_D = 0.15$ V for the Ga-rich device, and $V_G - V_{off} = 1.9$ V, $V_D = 0.09$ V for the MOCVD-grown device, so that the noise originates from the gated portion of the channel. The Hooge parameter α can be calculated for these devices as follows: [54]

$$\alpha = f \frac{S_{V_d}}{V_D^2} \frac{L_{ungated}^2}{q\mu R_{ungated}} \quad (7.5)$$

where $L_{ungated}$ is the length of the access regions in the HEMT, $R_{ungated}$ is the resistance of the ungated regions, since under the given voltage conditions $R_{ungated} \gg R_{gate}$; μ is the mobility in the channel region. $\alpha \approx 10^{-5}$ ($R_{ungated} \approx 24 \Omega$) for Ga-rich device, 7×10^{-5} ($R_{ungated} \approx 55 \Omega$) for the N-rich device and 6×10^{-5} ($R_{ungated} \approx 21 \Omega$) for the MOCVD-grown device. At least 3 devices of each kind exhibited similar noise spectra, as shown in Fig. 7.7. The top x -axis corresponds to the activation energy scale calculated using (7.3). Two kinds of noise profiles are observed in the HEMTs. All devices show a peak at low temperature, at ~ 100 K, which corresponds to an activation energy of 0.2 eV.

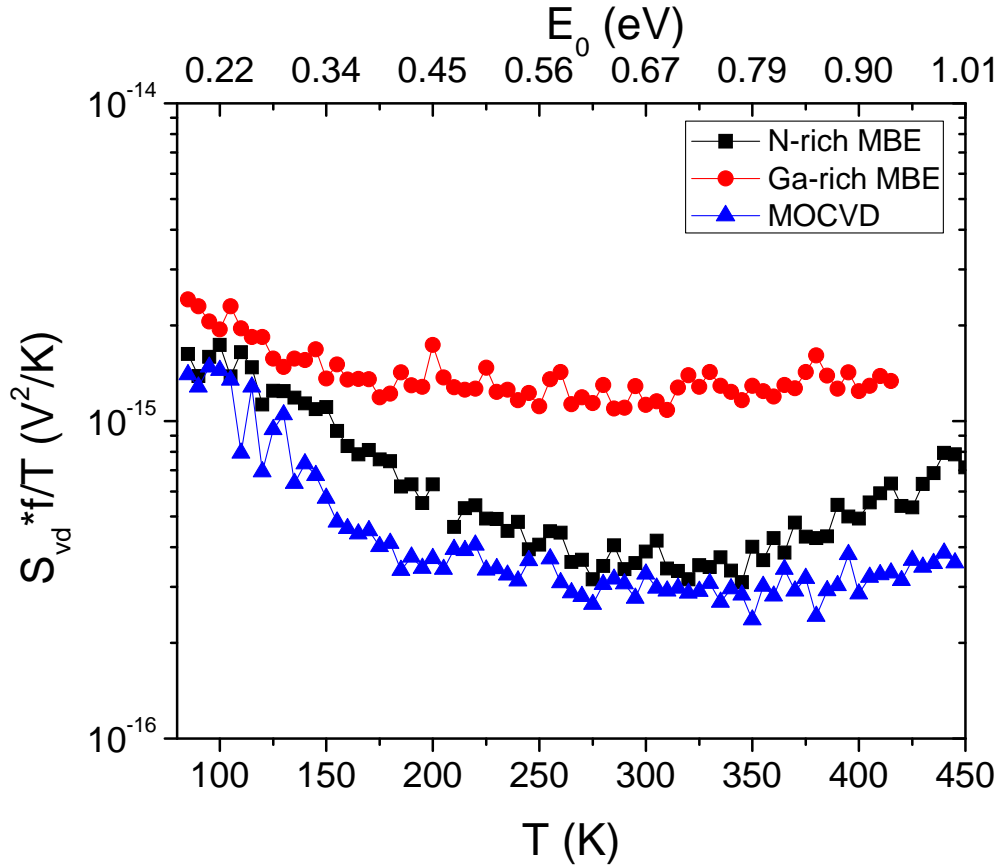


Fig. 7.7. Noise vs. temperature for N-rich and Ga-rich MBE and MOCVD-grown devices. $f = 10$ Hz. [63]

To understand the likely origin of the low-temperature peak in the noise, Fig. 7.8 shows the results of DFT calculations of defects in ternary alloy $\text{Al}_{0.30}\text{Ga}_{0.70}\text{N}$. Thermal excitation of an O_N^{-1} DX center can lead to physical reconfiguration of the defect and emission of an electron to the AlGaIn conduction band, which convert the negatively charged DX center into a neutral O_N .

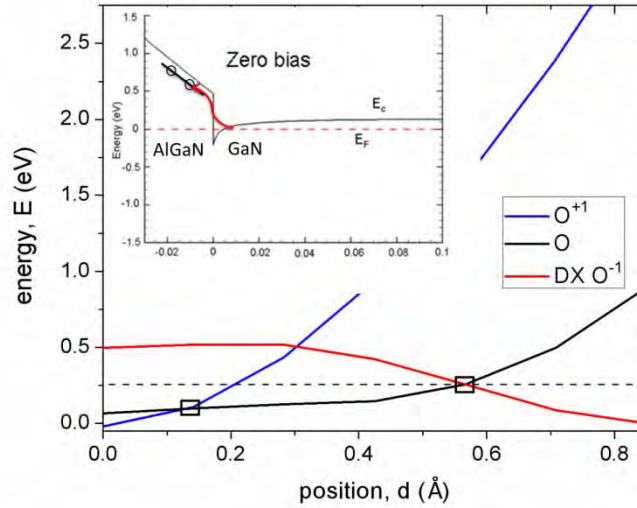


Fig. 7.8. Defect energy of substitutional O in AlGaIn as a function of the distance from the ideal lattice site, showing the existence of a DX configuration. Black squares represent transition points between the charge states of O_N during the electron emission. The dashed line shows that the energy barrier to emit one electron from a negatively charged O DX center is ~ 0.25 eV. The inset schematically illustrates the capture of one electron by the positively charged oxygen O_N^{+1} , which involves thermally excited tunneling (red arrow) of an electron from GaN Fermi level to the empty level of O_N^{+1} defect in AlGaIn. The energy level drops significantly in energy upon capture of two electrons. [63]

Further release of an electron results in a positively charged O_N^{+1} . This result is consistent with calculations of the configuration energy of an oxygen DX center in AlN and GaN by McCluskey, et al. [68]. The crossover point of the energy curve of O^{-1} with that of O^0 shows that the energy barrier for this thermal excitation is ~ 0.25 eV. The further emission of an electron from O^0 , resulting in O_N^{+1} , has essentially no energy barrier. The capture of one electron by O_N^{+1} has an energy barrier of ~ 0.3 eV at the AlGaIn/GaN interface, as shown in the inset of Fig. 7.8. This process involves an electron that is thermally excited from the Fermi level in the GaN and

tunnels to the empty level of the O^{+1} defect, which is ~ 0.1 eV below the AlGaN conduction band. The second electron capture has an energy barrier of ~ 0.35 eV, involving a thermally excited electron tunneling to the unfilled level of O^0 , which is ~ 0.05 eV below the AlGaN conduction band. The subsequent structural relaxation will result in a O_N^{-1} DX center. A qualitatively similar process of O defect reconfiguration also contributes to noise in Si MOSFETs [65].

Nitrogen-rich devices exhibit a second noise peak at temperatures well above 300 K, which cannot be completely observed in Fig. 7.7. The temperature of the noise system could not be increased beyond 450 K, owing to limitations of the device packaging materials and the measurement system. The second peak, which is greater than 1 eV, evidently corresponds to the transition between negative and neutral charge states of nitrogen antisite defects [62]. The results indicate the dominance of a different kind of defect under nitrogen-rich growth conditions, as opposed to Ga-rich or ammonia-rich growth, confirming earlier conclusions [46]. At intermediate temperatures where the defect energy distribution is largely featureless, a broad range of energy levels associated with hydrogenated N antisites, Ga-N divacancies, and C impurity defects dominate the noise [47].

7.4 Noise spectroscopy under low current conditions

On biasing the devices extremely close to pinch-off, at $V_G - V_{off} = 0.1$ V, with drain voltage less than 0.05 V, the noise does not obey the Dutta-Horn formalism, as shown in Figs. 7.9(a)-(c). Fig. 7.9(a)-(c) show the experimental and calculated values of the frequency exponent of the noise, γ , for devices grown using Ga-rich and N-rich MBE and with MOCVD. Because the devices are biased close to pinch-off, the resistance of the ungated portion of the channel is much

lower than that of the gated part, $R_{ungated} \ll R_{gate}$. The Hooge parameter α can be calculated for these devices as follows [54]:

$$\alpha = f \frac{S_{V_d}}{V_D^2} \frac{L_{gate}^2}{q\mu R_{gate}} \quad (7.6)$$

Thus, for the Ga-rich device, $\alpha \approx 2.5 \times 10^{-3}$ ($R_{gate} \approx 460 \Omega$); for the N-rich device, $\alpha \approx 1.6 \times 10^{-2}$ ($R_{gate} \approx 576 \Omega$), and for the MOCVD-grown device $\alpha \approx 2.3 \times 10^{-3}$ ($R_{gate} \approx 680 \Omega$).

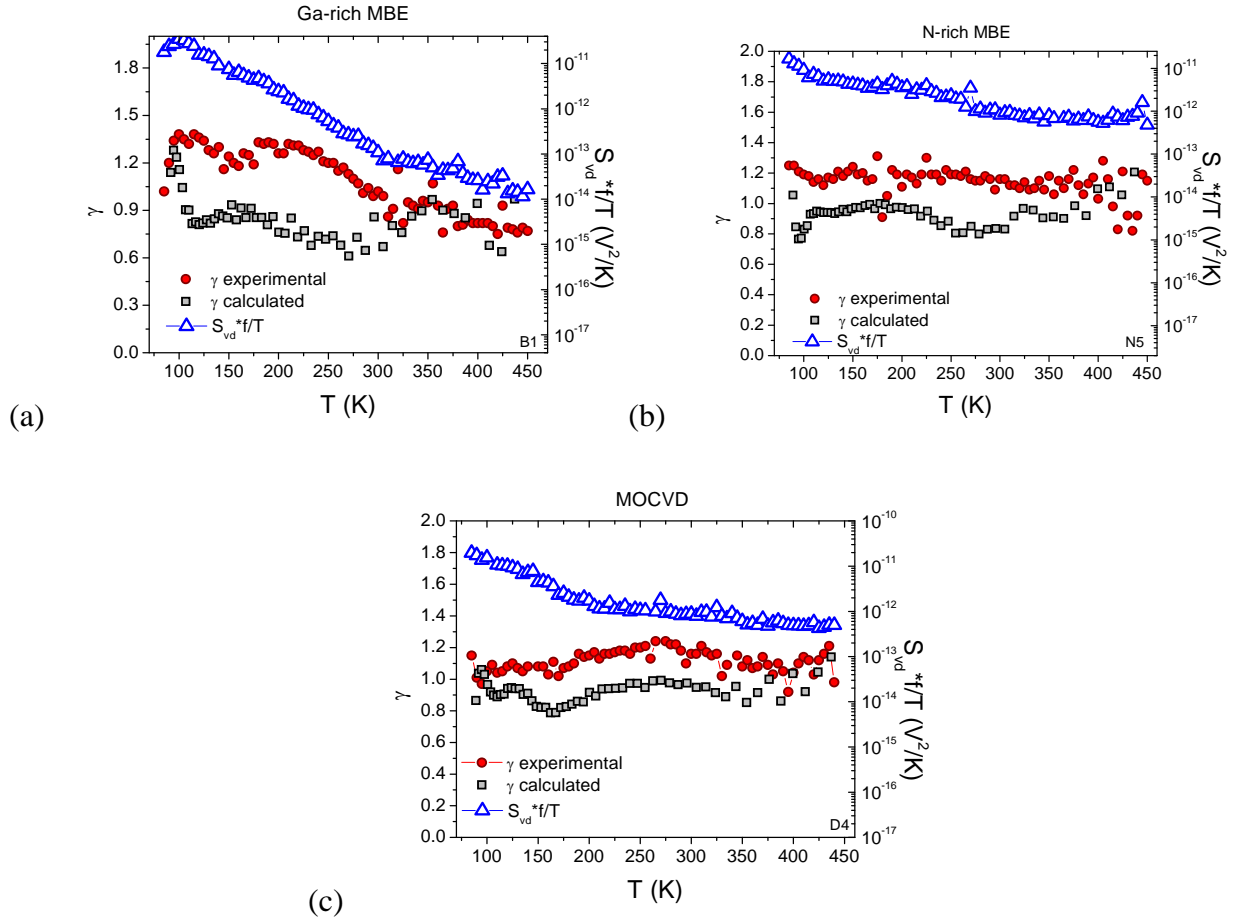


Fig. 7.9. Calculated and experimental γ , and noise power spectral density as a function of temperature for (a) Ga-rich MBE-grown, (b) N-rich MBE-grown, and (c) MOCVD-grown devices. $f = 10$ Hz.

There is no matching between the calculated and observed values of γ . The resistance of the complete channel is more than an order of magnitude higher during the low current

conditions than during the high current conditions used in this work. The effect of the temperature dependence of scattering mechanisms can be higher under the low current conditions, than during the high current conditions, causing the devices to disobey the Dutta-Horn model under the low current conditions of noise measurement. The Hooge parameters calculated for the voltage conditions where noise is measured are two orders of magnitude higher than the Hooge parameters calculated for the noise measurement at high current conditions. Also, the noise at 85 K is more than an order of magnitude higher than the noise at 450 K. Fig. 7.10 shows the noise as a function of temperature for the three kinds of devices, showing similar noise magnitudes for the three kinds.

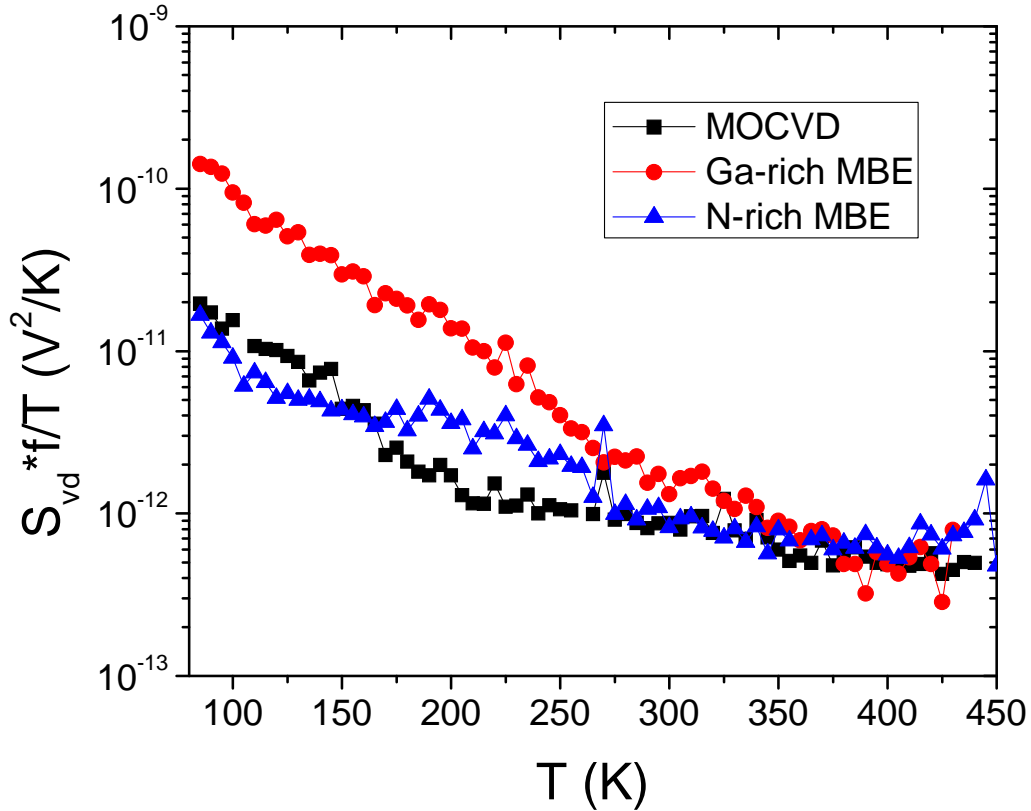


Fig. 7.10. Noise vs. temperature for Ga-rich, N-rich and MOCVD-grown samples. Noise was measured for Ga-rich and N-rich MBE-grown devices at $V_G - V_{off} = 0.1$ V, $V_D = 0.02$ V, and for MOCVD-grown device at $V_G - V_{off} = 0.1$ V, $V_D = 0.05$ V.

7.5 Post-stress noise measurements

We observed in Chapter V that some devices show a decrease in noise after stress, while some devices show an increase. Fig. 7.11 shows the decrease in noise across the entire temperature range, for two Ga-rich devices showing a positive pinch-off voltage shift of 0.1 V.

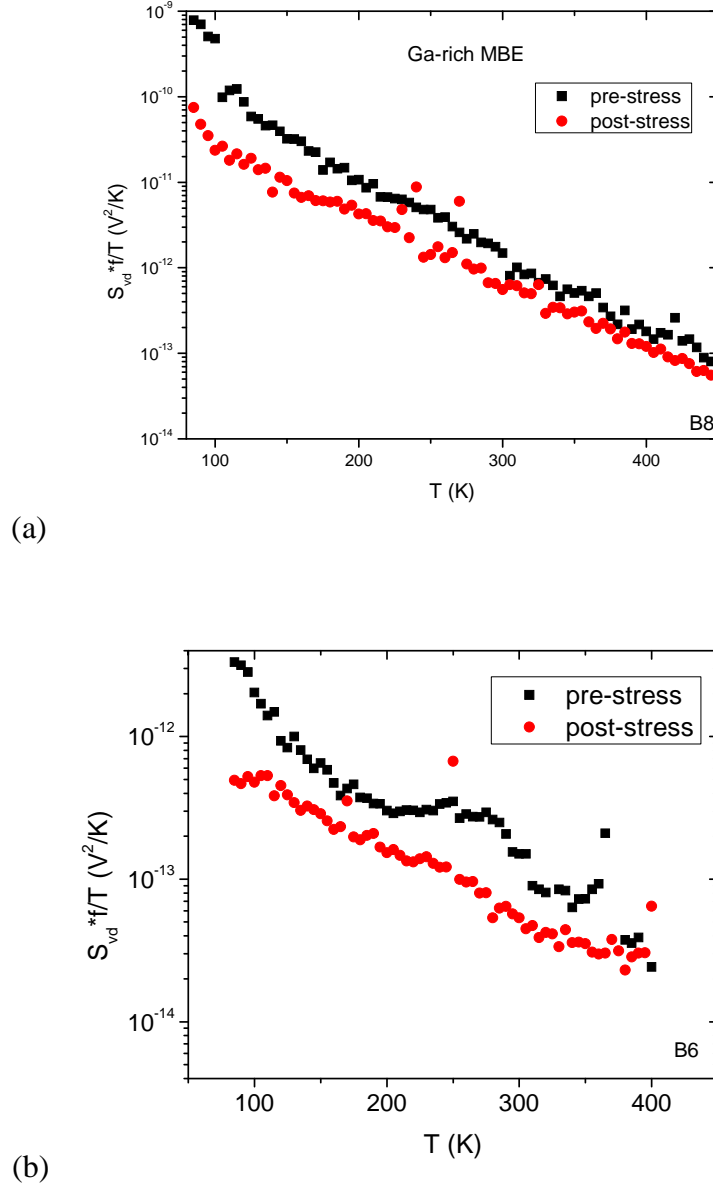


Fig. 7.11. Noise as a function of temperature for two Ga-rich MBE-grown devices; $f = 10$ Hz. Noise decreases after stress. Noise is measured at $V_G - V_{off} = 0.1$ V, and for (a) $V_D = 0.05$ V, for (b) $V_D = 0.02$ V.

Fig. 7.12 shows the comparison of the observed and calculated value of the frequency exponent, before and after stress. The theory described in Section 7.3 is used here for the calculation of the frequency exponent γ . The calculated and observed values of γ do not match, indicating that the noise does not follow the Dutta-Horn model. The Hooge parameter α is calculated using equation (7.6), for the device in 7.12(a) as 5.9×10^{-3} ($R_{gate} \approx 432 \Omega$), and for the device in 7.12(b) as 7.9×10^{-3} ($R_{gate} \approx 206 \Omega$).

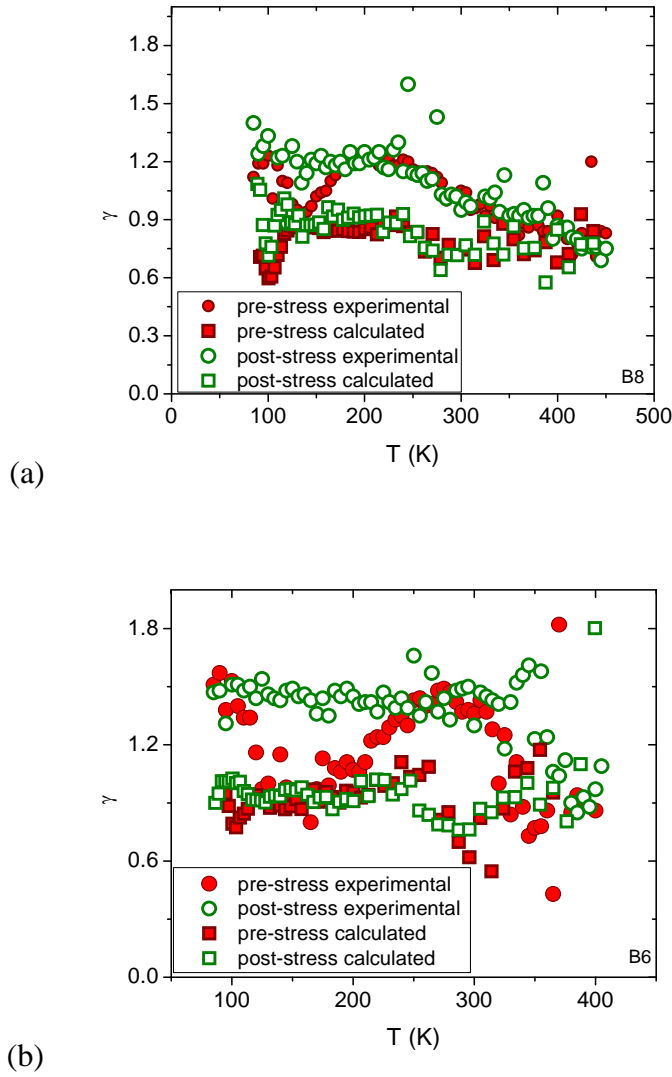


Fig. 7.12. Comparison of calculated and observed values of frequency exponent γ of $1/f^\beta$ noise, as a function of temperature for two different Ga-rich MBE-grown devices.

Fig. 7.13 shows the noise spectrum, before and after stress of an MOCVD-grown samples which show a negative shift in pinch-off after stress. This device undergoes a pinch-off voltage shift of -0.1 V after stress. The post-stress noise is greater than the pre-stress noise across the entire temperature range of 85 K to 450 K.

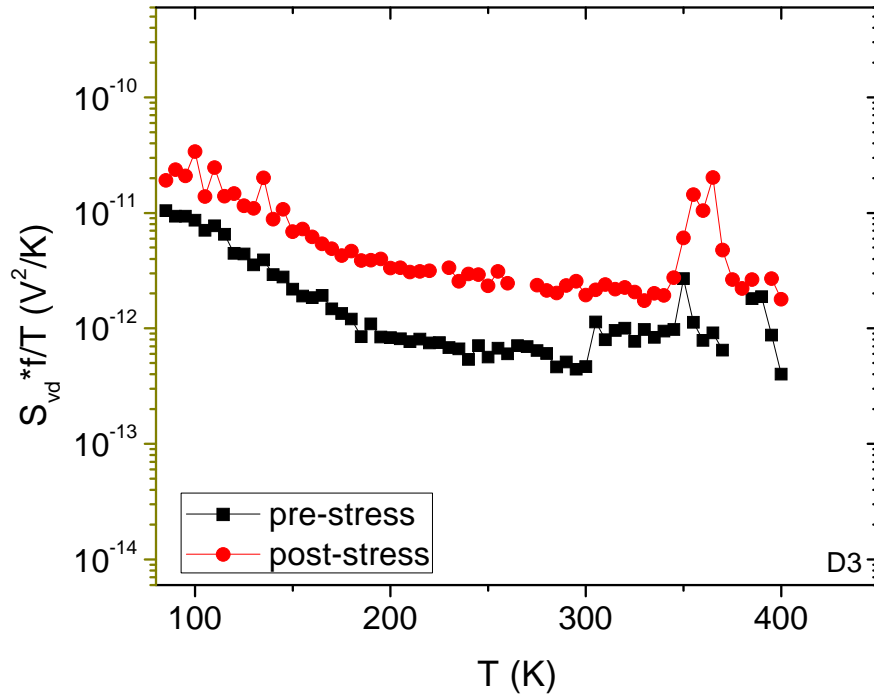


Fig. 7.13. Noise before and after stress as a function of temperature for an MOCVD-grown device; $f = 10$ Hz. After stress $\Delta V_{pinch-off} = -0.1$ V. Noise is measured at $V_G - V_{off} = 0.1$ V, $V_D = 0.05$ V.

Fig. 7.14 shows the comparison of the calculated and experimental value of γ , both before and after stress. The Hooge parameter, using equation (7.6) is calculated to be 2×10^{-3} ($R_{gate} \approx 390 \Omega$) for this device. The calculated and observed values do not match, showing that the noise, again, does not follow the Dutta-Horn formalism, possibly due to a temperature-dependence of

the effect of the transition between two energy states of the defect on the resistance of the channel [69].

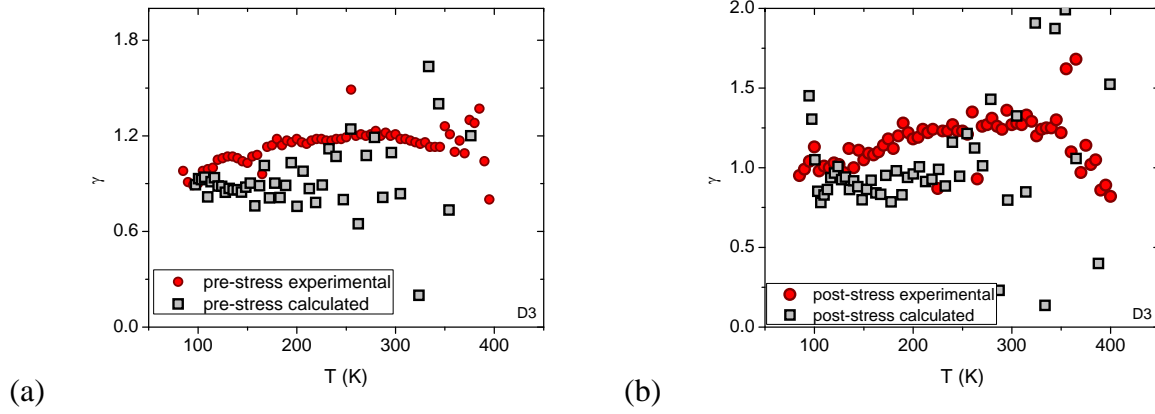


Fig. 7.14. γ vs. T , (a) before stress, and (b) after stress, for a MOCVD-grown device. Both experimental and calculated values are shown.

Fig. 7.15 shows the noise spectrum before and after stress of an ammonia-rich MBE-grown sample. This device shows a pinch-off voltage shift of -1.1 V after stress. The noise is seen to increase after stress.

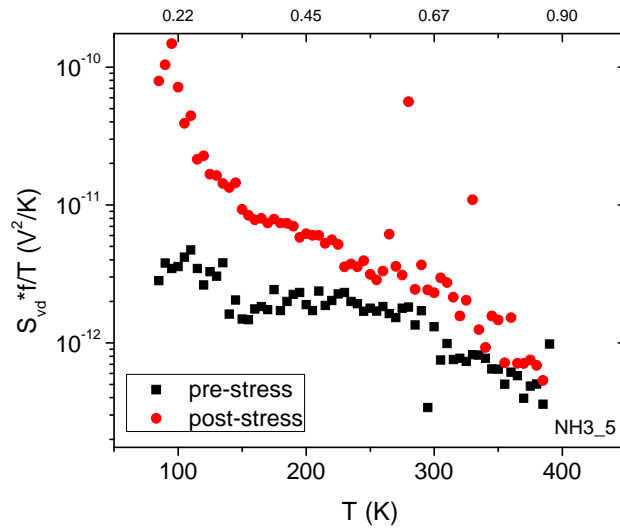


Fig. 7.15. Noise before and after stress as a function of temperature for an NH_3 -rich MBE-grown device; $f = 10$ Hz. After stress $\Delta V_{\text{pinch-off}} = -1.1$ V. The noise is measured at $V_G - V_{\text{off}} = 0.1$ V, $V_D = 0.05$ V.

Fig. 7.16 shows the dependence of the frequency exponent of $1/f$ noise γ , before and after stress. The calculated value of γ matches with the experimentally observed values, for at least the lower temperatures ($T < 300$ K). Hence, the energy scale calculated in Section 7.3 can be used for this device. A peak is observed at ~ 0.2 eV, for both the pre-stress and post-stress energy distributions. The Hooge parameter $\alpha \approx 7 \times 10^{-3}$, using equation (7.6).

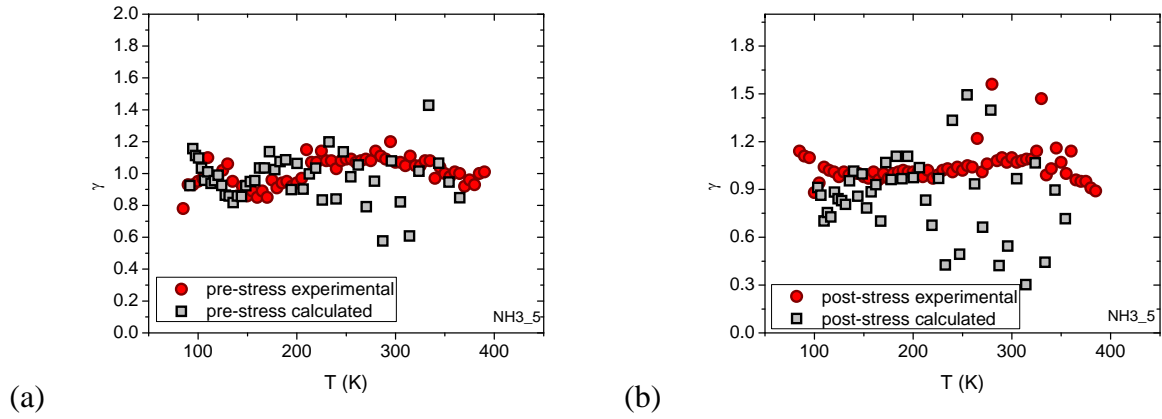


Fig. 7.16. γ vs. T , (a) before stress, and (b) after stress, for NH_3 -rich MBE-grown device. Both experimental and calculated values are shown.

Fig. 7.17 shows the pre-stress and post-stress noise for an N-rich MBE-grown device under high current conditions for the noise measurement. This device undergoes a negative shift of 0.3 V in pinch-off voltage after stress. The pre-stress noise is lower than the post-stress noise across the entire temperature range of 85 K to 450 K. Fig. 7.18 shows the comparison of the calculated and experimentally observed γ values as a function of temperature, before and after stress. For the high current conditions during the noise measurements, as seen in Section 7.3, the Dutta-Horn model is explicitly followed. Hence, the defect energy distribution in the N-rich device can be obtained before and after stress, as shown in Fig. 7.17. The Hooge parameter $\alpha \approx 2 \times 10^{-5}$ for this device, calculated using equation (7.5).

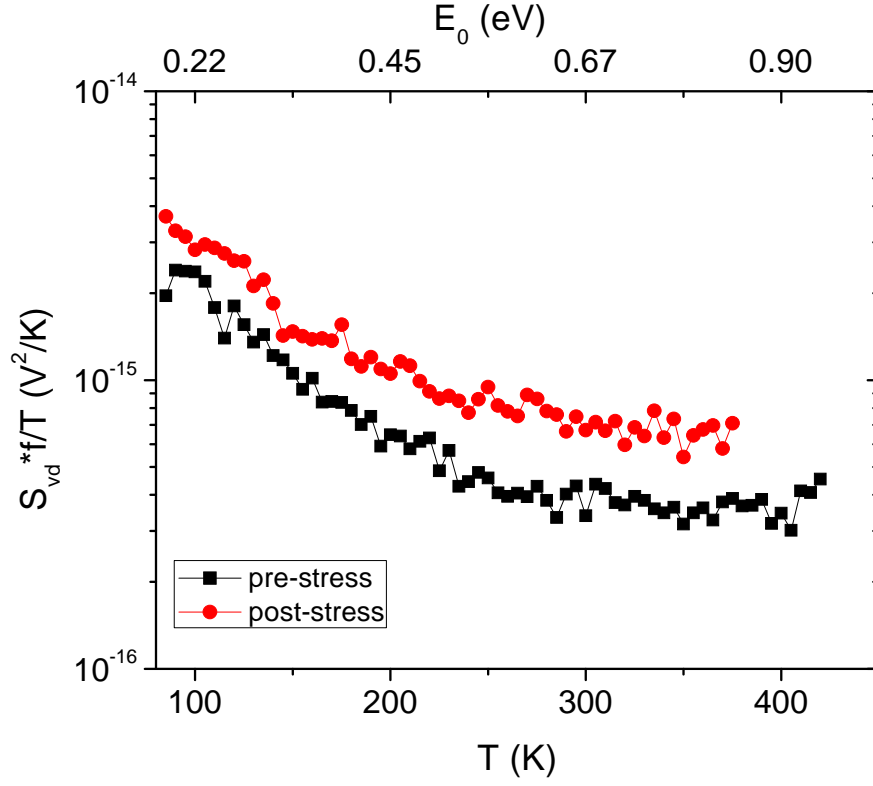
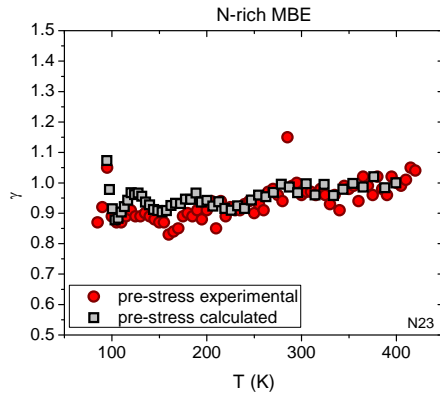
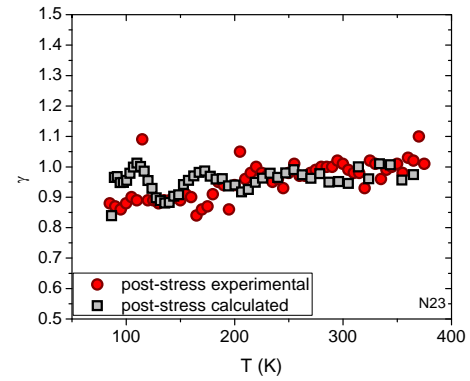


Fig. 7.17. Noise before and after stress as a function of temperature for an N-rich MBE-grown device; $f = 10$ Hz. After stress $\Delta V_{pinch-off} = -0.3$ V. The noise is measured at $V_G - V_{off} = 1.8$ V, $V_D = 0.15$ V.



(a)



(b)

Fig. 7.18. γ vs. T , (a) before stress, and (b) after stress, for a N-rich MBE-grown device. Both experimental and calculated values are shown.

Whether an increase or a decrease is observed in the post-stress noise as compared to the pre-stress noise, the spectrum across the temperature range of 85 K to 450 K does not vary much in shape. Figs. 7.11, 7.13, 7.15 and 7.17 illustrate this point. Specifically, a peak is observed in the noise spectrum at ~ 100 K, which converts to 0.2 eV on the energy scale, if the noise follows the Dutta-Horn model. Since the shape of the noise spectrum does not alter with stress, it means that no new kinds of defects are created by stress, while defects which were contributing to noise before stress are increasing in number after stress. As we have seen in Chapter IV and VI, Ga-vacancies which contribute to a positive shift in pinch-off voltage, do not contribute to noise, and hence will not change the shape of the energy distribution. The noise decreases in both Ga-rich devices shown here, possibly due to the dehydrogenation of C_N -impurities, which stop contributing to noise, and do not affect the pinch-off voltage. N-antisites, which cause a negative shift in pinch-off voltage upon dehydrogenation, also causes an increase in noise after stress, as has been seen in Figs. 7.13, 7.15 and 7.17.

7.6 Conclusions

In this chapter, we show the defect energy spectrum of GaN HEMTs grown under Ga-rich, N-rich, and NH_3 -rich conditions. Ga-rich and NH_3 -rich devices have similar defect energy spectra. All devices show a peak in defect activation energy at 0.2 eV, which corresponds to the reconfiguration energy of O DX center in AlGaN. A second peak is observed in N-rich samples at > 1 eV, which corresponds to the reconfiguration of a nitrogen antisite. When noise measurements are done very close to pinch-off, at $V_G - V_{off} = 0.1$ V, the noise does not follow the Dutta-Horn formalism. This could be because of temperature dependence of scattering mechanisms, which affect the resistance of channel under low current conditions more than

during the high current conditions. We recommend that noise measurements be done in GaN HEMTs at $V_G - V_{off} > 1$ V, for obtaining meaningful data about defect configuration energies.

In some devices, the noise increases with stress, while in others, it decreases. The noise spectrum does not change its shape with stress, indicating that no new kinds of defects are created by hot electrons produced during the stress. The noise spectrum invariably peaks at temperatures at or below ~ 100 K, which can be converted to an energy of 0.2 eV, if the noise follows Dutta-Horn model. It is observed that the pre-stress and post-stress noise follows the Dutta-Horn model when noise is measured under the high current conditions described in the chapter. The noise might not follow the Dutta-Horn model if measured under the low current conditions described.

CHAPTER 8

PROTON-INDUCED DEGRADATION IN GaN HEMTs

8.1 Introduction

Most previous studies of proton-induced degradation of GaN HEMTs suggest significant radiation tolerance. In one experiment, the dc current and transconductance degraded by 60% and 70%, respectively, for a 1.8 MeV proton fluence of 10^{14} p⁺/cm² [67], which is a fluence that is higher than that experienced in all but the most extreme space systems. For some GaN HEMTs, minimal changes in dc characteristics were reported after irradiation with 1.8 MeV protons to a fluence of 10^{14} cm⁻² [70]-[72]. In this work, GaN HEMTs grown using MOCVD and MBE under Ga-rich, N-rich, and NH₃-rich conditions were irradiated with 1.8 MeV protons. [64,73]

8.2 Experimental results

8.2.1 DC characteristics

The I_D - V_G characteristics of HEMTs grown using Ga-rich and N-rich MBE and MOCVD are shown in Fig. 8.1, before and after irradiation. While the Ga-rich and N-rich devices show positive shifts in pinch-off voltage and degradation in saturation current up to a fluence of 10^{14} cm⁻², the MOCVD-grown devices show very little change in current and pinch-off voltage. The positive shift in pinch-off voltage with increasing fluence for the devices indicates the creation of acceptor-like traps. Previous reports show that the defects causing the degradation are created in the AlGa_xN barrier. The reduction in saturation current results from mobility degradation [74,75].

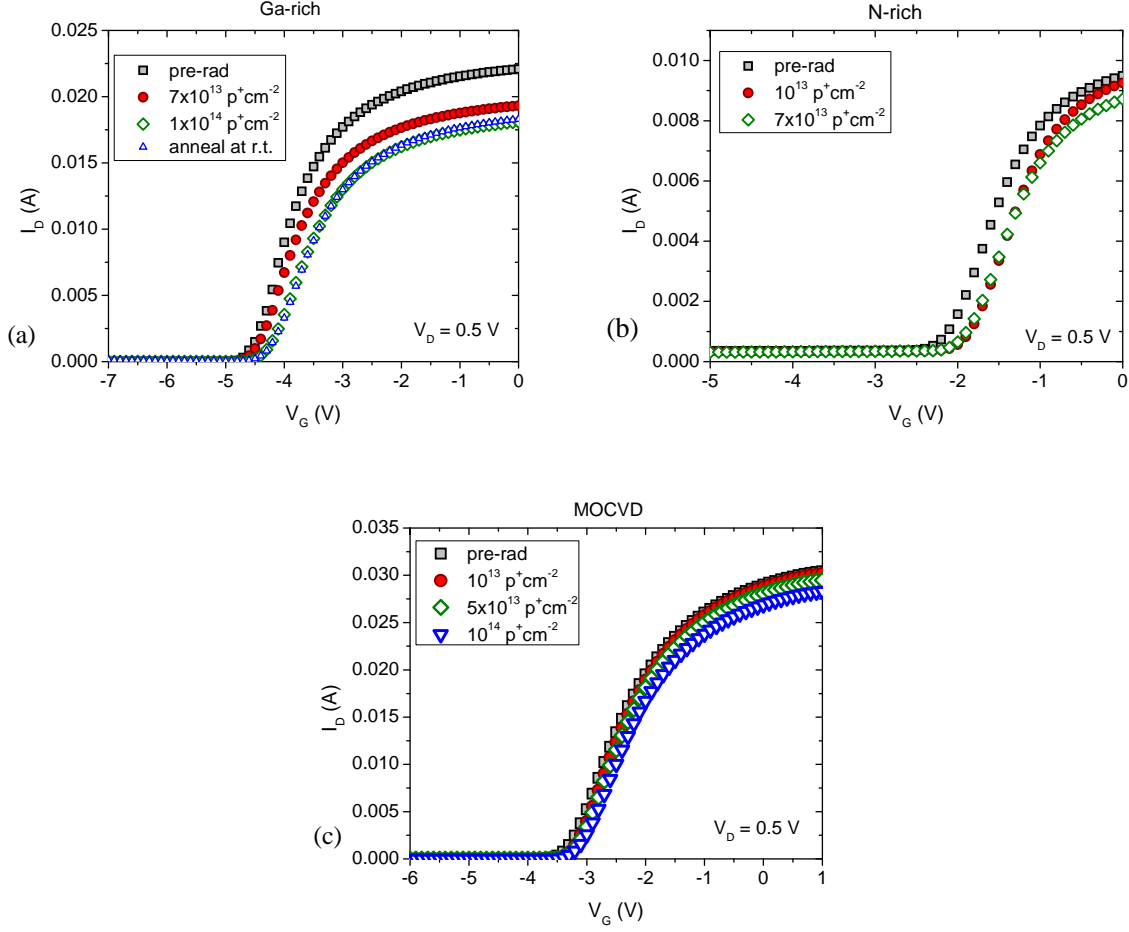


Fig. 8.1. I_D - V_G curves for devices grown using (a) Ga-rich, (b) N-rich MBE, and (c) MOCVD, before and after irradiation. The transfer characteristics after annealing for several weeks at room temperature are also shown in (a) for the Ga-rich devices. [64]

Fig. 8.2 shows the I_G - V_G characteristics of the Ga-rich, N-rich, and MOCVD-grown devices before and after irradiation. The gate leakage increases with increasing fluence. This is because of the reduction of the Schottky barrier height [72], and the creation of traps in the AlGaN barrier contributing to leakage paths. Figs. 8.1(a) and 8.2(a) show that the defects created by proton bombardment cause permanent degradation of the GaN HEMTs. After several weeks of room temperature annealing following proton irradiation of 10^{14} cm^{-2} , no change in drain, or gate current is seen in the Ga-rich devices. Annealing trends are similar in the other devices.

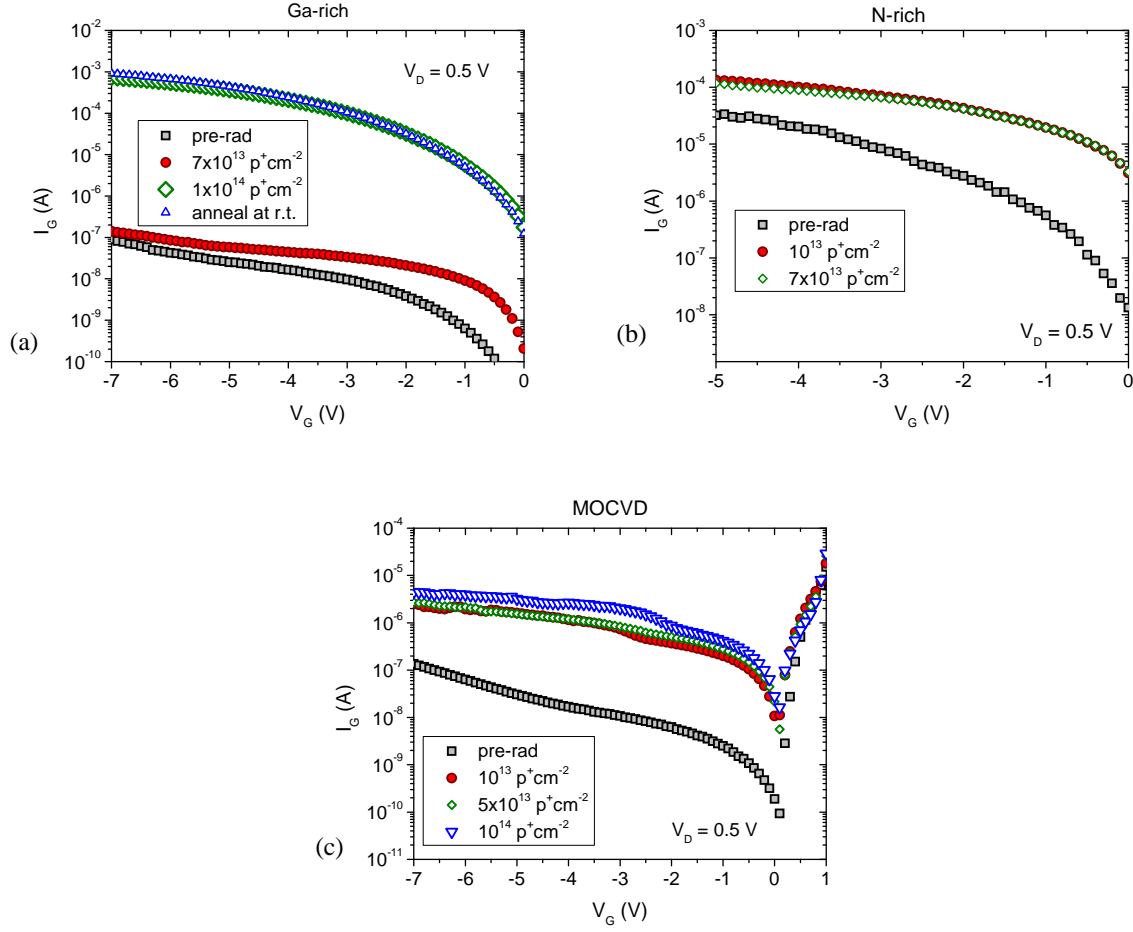


Fig.8.2. I_G - V_G curves for devices grown using (a) Ga-rich MBE, (b) N-rich MBE, and (c) MOCVD, before and after irradiation.[64]

Fig. 8.3(a) shows that that proton-irradiated Ga-rich and N-rich devices show positive shifts in threshold voltage, as do MOCVD and NH_3 -rich MBE devices, which show smaller changes in threshold voltage. Figs. 8.3(b)-(c) show the device-to-device variability of the threshold voltage shift in Ga-rich MBE and ammonia-rich MOCVD devices in greater detail. Ga-rich MBE devices show significantly larger shifts than the ammonia-rich MOCVD devices, while the variability is generally within 0.2 V in both groups of devices.

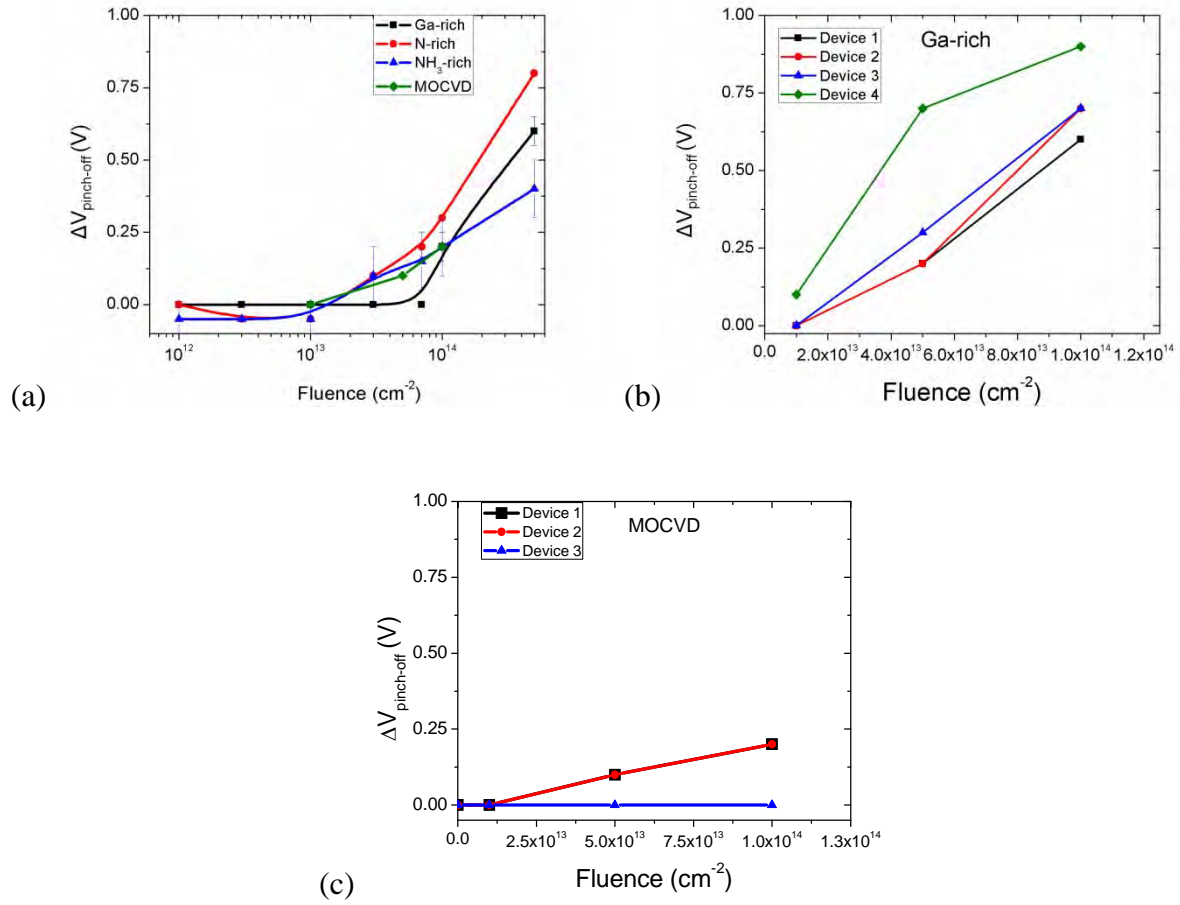


Fig. 8.3. (a) $\Delta V_{\text{pinch-off}}$ is shown as a function of 1.8 MeV proton fluence for devices grown by MBE under N-, Ga-rich, and NH_3 -rich conditions, and by MOCVD. Device to device variation in pinch-off voltage shift as a function of proton fluence for devices grown by (b) Ga-rich MBE, and (c) MOCVD. [73]

8.2.2 S_{vd} vs frequency

Fig. 8.4 shows the $1/f$ noise as a function of frequency for $V_G = V_{\text{off}} + 0.1$ V, $V_D = 20$ mV, and $f = 10$ Hz. The Ga-rich, N-rich, and NH_3 -rich devices all show an increase in noise as they are irradiated with protons up to a fluence of 7×10^{13} cm^{-2} . Proton bombardment leads to displacement damage in GaN and AlGaN, which creates new defects in these layers. The noise is most sensitive to defects in the AlGaN. The increase in noise with increasing proton fluence

suggests that new defect levels are being created close to the Fermi level during noise measurement [76,78].

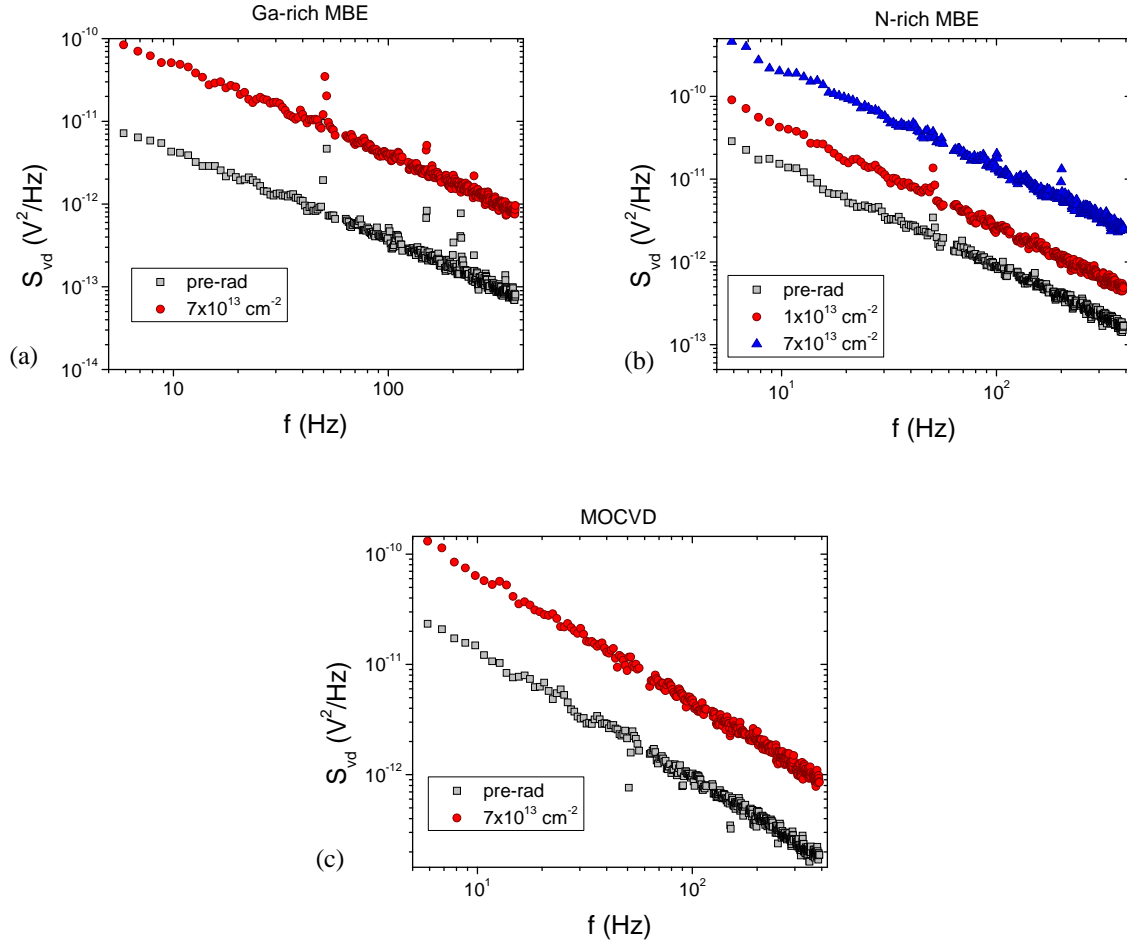


Fig. 8.4. S_{vd} vs. frequency before and after irradiation for (a) Ga-rich MBE, (b) N-rich MBE, and (c) MOCVD-grown devices. [62]

Fig. 8.5 shows the gate voltage dependence of the excess drain-voltage noise power spectral density, S_{vd} , before and after irradiation. The noise increases with increasing proton fluence for all gate voltages, in all three kinds of devices. In all measurements, before and after irradiation, S_{vd} is proportional to $(V_G - V_{off})^{-1}$ at voltages close to pinch-off and $(V_G - V_{off})^{-3}$ as the

voltage increases in magnitude, showing that in all cases the noise is coming from the channel region.

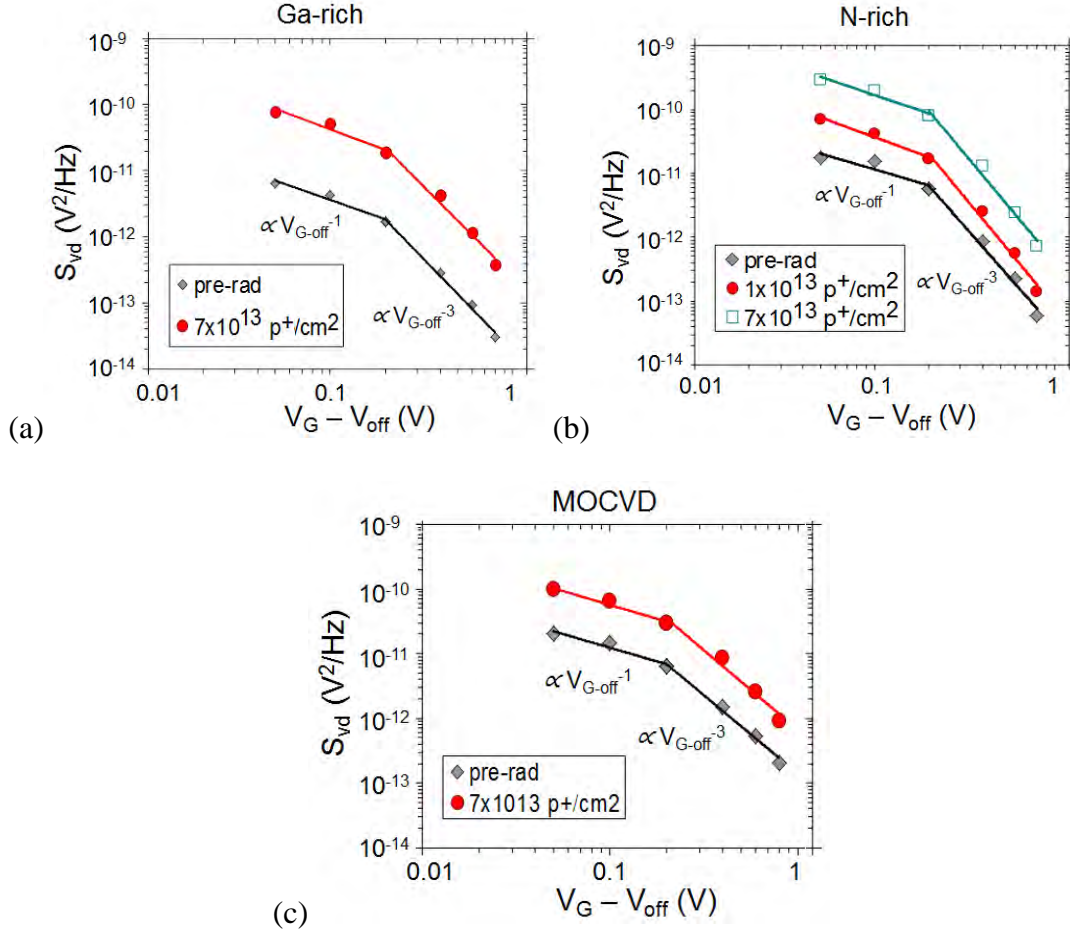


Fig. 8.5. Gate voltage dependence of S_{vd} before and after irradiation for (a) Ga-rich, (b) N-rich, and (c) MOCVD-grown devices. [64]

Hooge's parameter α can be calculated for the devices before and after irradiation, according to the relation [54]:

$$\alpha_{gate} = f \frac{S_{vd}}{V_d^2} \frac{L_{gate}^2}{q\mu R_{gate}} \quad (8.1)$$

where $R_{gate} \gg R_{ungated}$, when $V_G = V_{pinch-off} + 0.1$ V. For the typical Ga-rich, N-rich, and NH_3 -rich devices tested, the resistance of the gated region at $V_G = V_{pinch-off} + 0.1$ V is $\sim 250 \Omega$, $L_G = 0.7$

μm , and $V_D = 0.02$ V. Using S_{vd} at $f = 10$ Hz, the cumulative average Hooge parameters for all three kinds of devices is ~ 0.01 before radiation and ~ 0.08 after irradiation. These values are consistent with a broad range of experience on compound semiconductor devices subjected to defect-creating stresses (e.g., hot carriers) [53-55]. However, we note that the changes in device characteristics and low frequency noise in these devices are larger and more uniformly increasing with irradiation than those we observe after hot-carrier stress [45], in which modest electrical stress sometimes leads to an increase in noise, and at other times leads to a decrease in noise. Hydrogenation or de-hydrogenation of pre-existing defect sites (e.g., N-anti-site defects, C impurities) can account for some of these changes in the noise with hot carrier stress [45]. But these defects do not have energy levels and charge states that are consistent with the larger increases of noise observed in these proton irradiations.

8.2.3. S_{vd} vs. temperature

Low frequency $1/f$ noise was measured before and after irradiation at $V_G - V_{th} = 2.4$ V, $V_D = 0.15$ V, for the Ga-rich MBE devices, and $V_G - V_{th} = 2.7$ V, $V_D = 0.08$ V, for NH_3 -rich MOCVD devices. The gate voltage dependence of the noise power spectral density was verified to be $(V_G - V_{th})^{-3}$ for the devices investigated here, ensuring that the noise originates in the gated portion of the channel [64]. The noise was measured at temperatures from $T = 85$ K to $T = 450$ K.

The defect energy can be parameterized as a function of temperature, through the equation $E_0 = -k_B T \ln(\omega\tau_0)$ [61,65], where $\tau_0 = 3 \times 10^{-14}$ s, corresponding to the scattering rate of an electron off an optical phonon in the presence of typical defects present in GaN bulk [63].

Fig. 8.6(a) shows the noise spectrum at 85 K before and after irradiation with a fluence of

$10^{14} \text{ p}^+/\text{cm}^2$. Figs. 8.6-8.7 show $S_{vd}/V_d^2 \times f/T$ as a function of temperature for Ga-rich MBE and NH_3 -rich MOCVD devices before and after proton irradiation, for $f = 10 \text{ Hz}$; S_{vd} is the excess drain-voltage noise power spectral density.

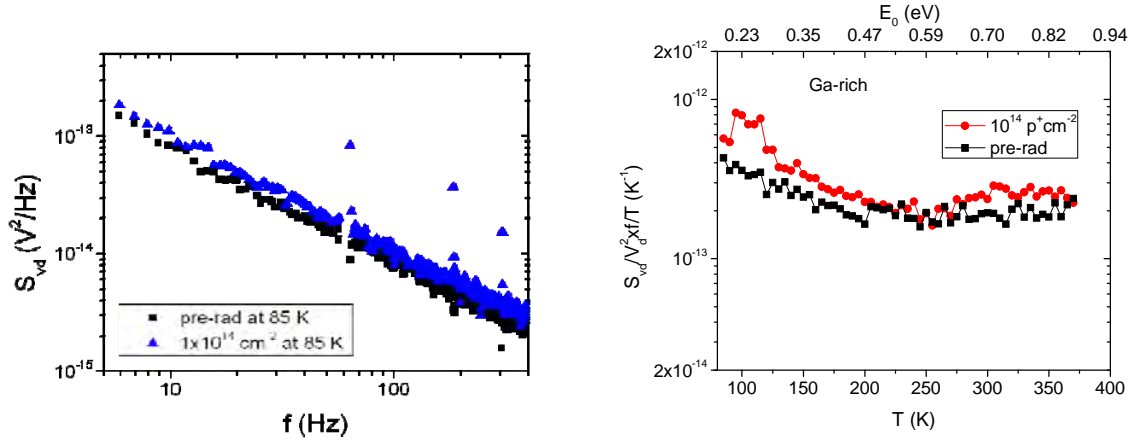


Fig. 8.6. (a) S_{vd} vs f , and (b) $S_{vd}/V_d^2 \times f/T$ vs. T for a Ga-rich MBE device before and after 1.8 MeV proton irradiation; the fluence is $1 \times 10^{14} \text{ cm}^{-2}$. [73]

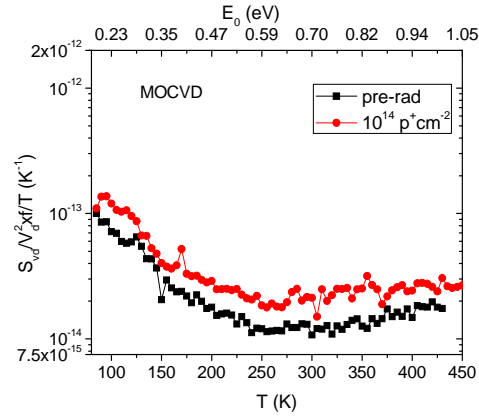


Fig. 8.7. $S_{vd}/V_d^2 \times f/T$ vs. T for a N-rich MOCVD device before and after 1.8 MeV proton irradiation; the fluence is $1 \times 10^{14} \text{ cm}^{-2}$. [73]

The noise increases after irradiation, but the defect configuration energy profile looks similar after irradiation to that observed before irradiation. This indicates that proton irradiation primarily creates new defects of the type that dominate the pre-irradiation noise. Considering the

differences in effective gate voltage and drain voltage during noise measurement, the ratio between the noise magnitude in the Ga-rich device and the MOCVD device should be as follows, in the absence of any difference in defect densities:

$$\frac{S_{vd}(Ga-rich)}{S_{vd}(MOCVD)} \propto \frac{(V_G - V_{th})_{Ga-rich}^{-3}}{(V_G - V_{th})_{MOCVD}^{-3}} \times \frac{V_{D-Ga-rich}^2}{V_{D-MOCVD}^2} \approx 5$$

The noise magnitude of the MOCVD device in Fig. 8.7 is much lower than for the Ga-rich MBE device in Fig. 8.6 over most of the temperature range, even after considering the differences in measurement voltages, indicating a significantly lower defect density for these MOCVD devices [61,64-65]. We note earlier that Ga-rich MBE devices show lower noise than N-rich and NH₃ rich MBE devices, so the MOCVD devices show the least noise of the four types of devices evaluated in this work.

8.3 Discussion

We now consider what kinds of defects may lead to the increase in noise with proton irradiation. The Fermi level in the AlGa_N barrier of these devices is $\sim E_c - 1.2$ eV at pinch-off [45]. Fig. 8.8 shows the formation energy of nitrogen vacancies and Ga-N divacancies as a function of the position of the Fermi energy, calculated using density functional theory. After irradiation, nitrogen vacancies and divacancies can be created by protons by the displacement of atoms in GaN and AlGa_N. These defects are negatively charged, acceptor-like traps, which cause the positive shift in pinch-off voltage, as seen in Fig. 8.8. When the noise is measured between $V_G = V_{pinch-off} + 0.05$ V to $V_{pinch-off} + 1$ V, the Fermi level is at $\sim E_c - 1.2$ eV in the AlGa_N barrier. At this position, there are changes in charge states associated with nitrogen vacancies and Ga-N divacancies. The charge state change for N vacancies is from -1 to -3 and for Ga-N divacancies is from -2 to -3 . Hence, these defects can take part in electron capture and release, causing the

noise to increase after irradiation. Ga vacancies, which do not have a transition level close to the location of the Fermi level, cannot contribute to the noise of these devices.

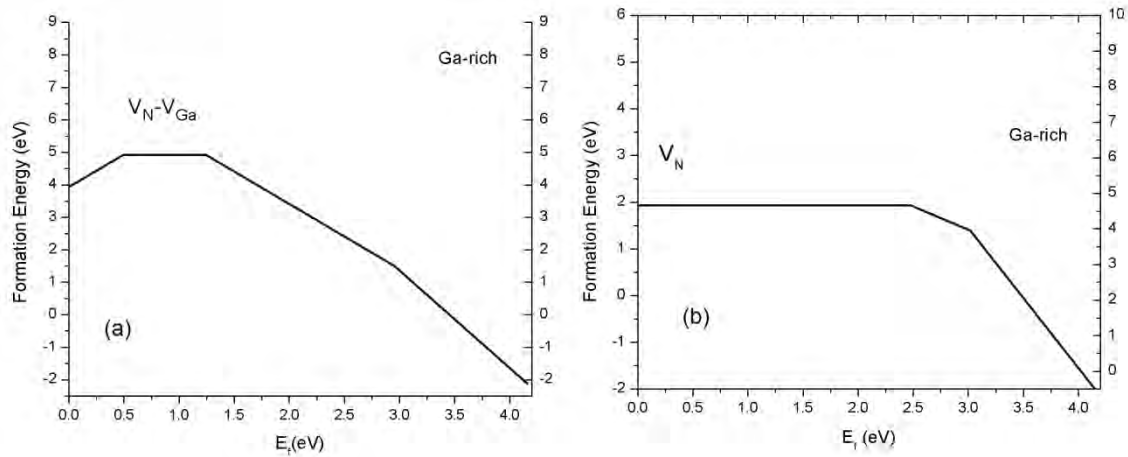


Fig. 8.8. Formation energy of (a) Ga-N divacancies and (b) N vacancies as a function of the position of the Fermi level in the band gap of $\text{Al}_{0.3}\text{Ga}_{0.7}\text{N}$. [64]

The initial concentration of the defects in GaN depends on the growth conditions. The presence of the initial defects enhances the probability of creating a stable defect due to the lower threshold displacement energy. A low-energy recoil can lead to a modification of a pre-existing defect, changing its charge state, resulting in creation of an additional acceptor. This causes a decrease in saturation drain current and a threshold voltage shift, as shown in Fig. 8.1. Higher energy recoils displace crystal atoms, creating an isolated defect, and/or resulting in the end-of-ion track clusters [78]. We showed that N vacancies may be responsible for an increase of $1/f$ noise in GaN/AlGaN HEMTs built in MBE material [64]. However, the recoil energy necessary for creating N vacancies is even higher than that required for Ga vacancies. On the other hand, the defect clusters typically have a high concentration of vacancies and vacancy complexes [79]. The concentration of such defects is statistically higher in the case of higher particle fluences. Assuming that the number of defects in clusters is proportional to the fluence, the concentration

of subsequently modified vacancies will have a non-linear dependence on the particle fluence. Therefore, the interaction of protons with atoms within defect complexes created by irradiation may contribute to the variability in the damage threshold and nonlinearities in the high fluence regime of the proton irradiation.

To illustrate this process in GaN/AlGaIn HEMTs, we start with a Ga vacancy V_{Ga} with four neighboring N atoms, which after the recoil can produce a neutral N_i and divacancy. The resulting neutral N_i will capture an electron, leading to additional acceptors, and consequently, to a positive shift in the threshold voltage, as shown below:



This is shown in Fig. 7.3, and similar to the previously observed electrical degradation in AlGaIn/GaN HEMTs, where dehydrogenation of Ga vacancies is proposed to cause the positive threshold shift [45]. The concentration of V_{Ga} is largest in the case of N-rich devices, where the observed post-irradiation shift is also the largest.

The N atom recoil at an antisite defect produces N_i and V_{Ga} , which subsequently capture three electrons, two by V_{Ga} and one by N_i .



These additional acceptors cause the threshold to shift in the positive direction, unlike the case of electron-stress induced degradation, where antisite dehydrogenation leads to a negative threshold shift [45]. There is only one atom, namely the N_{Ga} , which is prone to low-energy recoil displacement; therefore, the probability of energy transfer to N_{Ga} is four times smaller than in the case of V_{Ga} . This implies a smaller threshold voltage shift, consistent with the results of Fig. 8.2.

We note that proton beams can also remove H from hydrogenated defects either directly or via beam-generated hot electrons, through a process similar to that described in [45] for electrical stress. This effect, however, would cause a threshold shift that is opposite to what is observed in the NH_3 -rich MBE and MOCVD devices. This demonstrates that dehydrogenation plays at most a secondary role in the nonlinear portion of the proton-beam degradation, compared with N displacements at defects.

While there is no change in charge state near the conduction band for V_{Ga} , the divacancy has a -2 to -3 charge-state change, as shown in Fig. 9, contributing to the $1/f$ noise [64]. Therefore, displacement damage that results in the transformation of a V_{Ga} to a Ga-N divacancy can cause positive shifts in threshold voltage and contribute to the increase in the $1/f$ noise magnitude. This reinforces the significance of Ga-N divacancy defects in proton-irradiated GaN/AlGaN HEMTs.

8.4 Summary and Conclusions

We have characterized the radiation response of GaN/AlGaN HEMTs up to a 1.8-MeV proton fluence of 10^{14} cm^{-2} . Devices grown under ammonia-rich MBE are more susceptible to proton-induced degradation, as compared to devices grown under Ga-rich and N-rich MBE. The nature of the degradation of these devices by proton irradiation is different from the degradation caused by hot-electron-stress. While hot-electron-stress causes a positive shift in pinch-off voltage in Ga-rich and N-rich devices, and causes a negative shift in pinch-off voltage for ammonia-rich devices, proton irradiation causes positive shifts in pinch-off voltage for all three kinds of devices. The $1/f$ noise increases with increasing proton fluence up to $7 \times 10^{13} \text{ cm}^{-2}$. Ga-

N divacancies, which are acceptor-like in nature, are created by proton irradiation, and evidently are responsible for much of the increase in noise for the irradiated devices.

CHAPTER 9

CONCLUSIONS

We have performed reliability experiments on GaN HEMTs grown by both MBE and MOCVD. The MBE-grown HEMTs were grown under three different conditions – Ga-rich, N-rich, and NH₃-rich. Thus, we were able to study the defects which dominate under a particular growth condition. We have used low frequency $1/f$ noise as a diagnostic tool to have further insight into the defects. Density functional theory calculations for formation energy of defects present in the GaN and AlGa_N crystal help us correlate the degradation observed experimentally with the defects that might be responsible for the degradation. Our methodology involves subjecting devices to stress for a period of time, measuring the electrical characteristics and $1/f$ noise of the devices before and after stress, and using density functional theory calculations to identify the defects responsible for the electrical degradation of the devices. We have subjected the GaN HEMTs to DC stress under high field conditions, RF stress, and radiation stress using 1.8 MeV protons.

When GaN HEMTs grown using Ga-rich, N-rich, and NH₃-rich MBE and MOCVD are subjected to DC stress, with high field under the gate, Ga-rich and N-rich devices show a positive shift in pinch-off voltage, while the NH₃-rich MBE-grown and MOCVD-grown devices show a negative shift. Hot electrons during the high-field stress do not have enough energy to create new defects, but can change the charge state of the pre-existing defects. Since hydrogen easily permeates into the material system during fabrication, the native defects present in the system can become hydrogenated, owing to the low formation energy of the hydrogenated

counterparts of the native defects. Hot electrons can easily remove a hydrogen atom from these defects, resulting in a dehydrogenated defect with a different charge state. Hydrogenated Ga-vacancies present under Ga-rich and N-rich conditions can get dehydrogenated, to form a more negative defect than the pre-existing one. This causes a positive shift in pinch-off voltage observed in Ga-rich and N-rich devices. On the other hand, the dehydrogenation of N-antisites results in a charge state change of “0” from “-1”. Thus, NH_3 -rich devices show a negative shift in pinch-off voltage, and so do MOCVD-grown devices. Since MOCVD involves ammonia, MOCVD-grown devices have defects similar to NH_3 -rich MBE-grown devices.

RF stress results on GaN HEMTs indicate that the devices are robust, and not more than 5% change in small signal parameters is obtained after 4 hours of stress. There is a substantial drop-off of transconductance as the device is operated at high frequencies from DC, indicating a lot of traps to be present in the device. However, after RF stress, the g_m drop-off is seen to decrease.

Low frequency $1/f$ noise measurements performed before and after DC stress show that some devices exhibit a post-stress decrease in noise, while others show an increase. The change in noise after stress does not show much correlation with the growth conditions of the HEMTs. The increase in leakage current with increasing noise after stress indicates that defects, created in the AlGaIn barrier during the stress, contribute to the noise. We can identify the defects contributing to $1/f$ noise using density functional theory calculation results. The position in the band gap, where a change in charge state of the defect occurs, corresponds to a trap level. If this trap level is located within a few kT of the Fermi level location during the noise measurement, the defect should contribute to the noise. We find that Ga-vacancies do not contribute to noise. The hydrogenated N-antisite does not have a trap level close to the position of the Fermi level

during the noise measurement, but when dehydrogenated, shows a change in charge state close to the position of the Fermi level. Thus, this defect can cause an increase in noise after stress. Hydrogenated carbon impurities in N-site does show a change in charge state close the E_F location before stress. After stress, the dehydrogenated carbon impurity does not show a trap level close to E_F , which evidently accounts for the decrease in noise seen in some devices.

We have also shown that noise in GaN HEMTs conforms with the Dutta-Horn noise model when the noise is measured at gate voltages away from the pinch-off voltage so that the resistance of the gated portion of the channel is lower than the resistance of the ungated portion, but making sure that the noise still originates from the gated portion of the channel. Thus, the noise spectrum obtained as a function of temperature gives the distribution of the activation energy of processes that contribute to the noise. As electrons are captured or emitted by two metastable states of a defect, which may be only slightly separated in energy, noise is produced. The transition between the two states of the defect is facilitated by an electron-phonon interaction in the presence of the defect. We calculate a scattering rate of $3 \times 10^{13} \text{ s}^{-1}$ for an electron scattering off an optical phonon in the presence of Ga-vacancies. The activation energy distribution of the defects which contribute to noise can be calculated using the scattering rate and the temperature at which noise is measured. We observe a prominent peak in the defect energy distribution at 0.2 eV for all kinds of devices. This peak is shown to correspond to the reconfiguration of an oxygen DX center in AlGaN. A second peak at $> 1 \text{ eV}$ is observed in N-rich devices. This peak corresponds to the reconfiguration of an N-antisite. The defect energy distribution does not change its shape after DC stress, indicating that no new defects are created during the stress.

We have evaluated the 1.8-MeV-proton-induced degradation in the four kinds of HEMTs. All devices show a positive shift in pinch-off voltage after stress. Ga-N divacancies are created by protons, which cause the noise to increase after stress, and also cause the positive shift in pinch-off. There are a larger number of divacancies in Ga-rich devices, causing a higher positive shift in these devices compared to ammonia-rich and MOCVD-grown devices.

Thus, we have used DC stress, RF stress, and radiation stress to understand the mechanisms that cause degradation of GaN/AlGaIn HEMTs. The defects that limit the reliability of these devices have been identified using low frequency $1/f$ noise and density functional theory calculations.

REFERENCES

- [1] J. Joh and J. A. del Alamo, "RF power degradation of GaN high electron mobility transistors", *IEEE International Electron Devices Meeting*, pp. 20.2.1-4, San Francisco, CA, 2010.
- [2] J. Joh and J. A. del Alamo, "Critical voltage for electrical degradation of GaN high-electron mobility transistors", *IEEE Electron Dev. Lett.*, vol. 29, no. 4, pp. 287-289, 2008.
- [3] N. G. Weimann, M. J. Manfra, S. Chakraborty, and D. M. Tennant, "Submicron AlGaIn/GaN HEMTs with very high drain current density grown by plasma-assisted MBE on 6H-SiC", *IEEE Electron Dev. Lett.*, vol. 23, no. 12, pp. 691-693, 2002.
- [4] K. Matsushita, H. Sakurai, H. Kawasaki, Y. Takada, T. Sasaki, and K. Tsuda, "Gate leakage current of AlGaIn/GaN HEMT's device influenced by substrate defects", *Proceedings of the International Conference on GaAs Manufacturing Technology*, New Orleans, 2005, p. 4.2.
- [5] C. Poblenz, P. Waltereit, S. Rajan, S. Heikman, U. Mishra, and J. Speck, "Effect of carbon doping on buffer leakage in AlGaIn/GaN high electron mobility transistors", *J. Vacuum Sci. Tech. B*, vol. 22, no. 3, pp. 1145-1149, 2004.
- [6] H. Tang and J. B. Webb, "Growth of high mobility GaN by ammonia-molecular beam epitaxy", *Appl. Phys. Lett.*, vol. 74, no. 16, pp. 2373-2375, 1999.
- [7] A. E. Wickenden, D. D. Koleske, R. L. Henry, R. J. Gorman, J. C. Cubbertson, and M. E. Twigg, "The impact of nitridation and nucleation layer process conditions on morphology and electron transport in GaN epitaxial films", *J. Electron Mater.*, vol. 28, no. 3, pp. 301-307, 1999.
- [8] A. E. Wickenden, D. D. Koleske, R. L. Henry, R. J. Gorman, M. E. Twigg, M. Fatemi, J. A. Freitas, and W. J. Moore, "The influence of OMVPE growth pressure on the morphology, compensation, and doping of GaN and related alloys", *J. Electron Mater.*, vol. 29, no. 1, pp. 21-26, 2000.
- [9] S. Keller, Y. F. Wu, G. Parish, N. Ziang, J. J. Xu, B. P. Keller, S. P. DenBaars, and U. K. Mishra, "Gallium nitride based high power heterojunction field effect transistors: Process development and present status at UCSB", *IEEE Trans. Electron. Dev.*, vol. 48, no. 3, pp. 552-559, 2001.
- [10] J. A. Smart, A. T. Schremer, N. G. Weimann, O. Ambacher, L. F. Eastman, and J. R. Shealy, "AlGaIn/GaN heterostructures on insulating AlGaIn nucleation layers", *Appl. Phys. Lett.*, vol. 75, no. 3, pp. 388-390, 1999.

- [11] D. D. Koleske, R. L. Henry, M. E. Twigg, J. C. Culbertson, S. C. Binari, A. E. Wickenden and M. Fatemi, "Influence of AlN nucleation layer temperature on GaN electronic properties grown on SiC", *Appl. Phys. Lett.*, vol. 80, no. 23, pp. 4372-4374, 2002.
- [12] M. Rudzinski, P. R. Hageman, A. P. Grzegorzczak, L. Macht, T. C. Rödle, H. F. Jos, and P. K. Larsen, "Influence of the misorientation of 4H-SiC substrates on the morphology and crack formation in hetero epitaxial MOCVD grown GaN epilayers", *Phys. Stat. Sol. C*, vol. 2, no. 7, pp 2141-2144, 2005.
- [13] E. Tengborn, M. Rummukainen, F. Tuomisto, K. Saarinen, M. Rudzinski, P. R. Hageman, P. K. Larsen, and A. Nordlund, "Effect of the misorientation of the 4H-SiC substrate on the open volume defects in GaN grown by metal-organic chemical vapor deposition", *Appl. Phys. Lett.*, vol. 89, no. 9, pp. 091905-7, 2006.
- [14] L. F. Eastman, V. Tilak, J. Smart, B. M. Green, E. M. Chumbes, R. Dimitrov, H. Kim, O. S. Ambacher, N. Weimann, T. Prunty, M. Murphy, W. J. Schaff, and J. R. Shealy, "Undoped AlGaIn/GaN HEMTs for microwave power amplification", *IEEE Trans. Electron Dev.*, vol. 48, no. 3, pp. 479-485, 2001.
- [15] S. Müller, K. Köhler, R. Kiefer, R. Quay, M. Baeumber, and L. Kirste, "Growth of AlGaIn/GaN based electronic device structures with semi-insulating GaN buffer and AlN interlayer", *Phys. Stat. Sol. C*, vol. 2, no. 7, pp. 2639-2642, 2005.
- [16] M. Micovic, A. Kurdoghlian, P. Janke, D. W. S. Wong, J. S. Moon, L. McCray, and C. Nguyen, "AlGaIn/GaN heterojunction field effect transistors grown by nitrogen plasma assisted molecular beam epitaxy", *IEEE Trans. Electron Dev.*, vol. 48, no. 3, pp. 591-596, 2001.
- [17] Y. C. Choi, M. Pophristic, H. Y. Cha, B. Peres, M. G. Spencer, and L. F. Eastman, "The effect of an Fe-doped GaN buffer on off-state breakdown characteristics in AlGaIn/GaN HEMTs on Si substrate", *IEEE Trans. Electron. Dev.*, vol. 53, no. 12, pp. 2926-2931, 2006.
- [18] A. Armstrong, A. R. Arehart, B. Moran, S. P. DenBaars, U. K. Mishra, J. S. Speck, and S. A. Ringel, "Impact of carbon on trap states in n-type GaN grown by metalorganic chemical vapor deposition", *Appl. Phys. Lett.*, vol. 84, no. 3, pp. 374-376, 2004.
- [19] D. S. Katzer, D. F. Storm, S. C. Binari, J. A. Roussos, B. V. Shanabrook, and E. R. Glaser, "Molecular beam epitaxy of beryllium-doped GaN buffer layers for AlGaIn/GaN HEMTs", *J. Crystal Growth*, vol. 251, pp. 481-486, 2003.
- [20] M. J. Manfra, N. G. Weimann, O. Mitrofanov, T. Wächtler, and D. M. Tennant, "High power GaN/AlGaIn/GaN HEMTs operating at 2 to 25 GHz grown by plasma-assisted MBE", *Phys. Stat. Sol. A*, vol. 200, no. 1, pp. 175-178, 2003.

- [21] J. A. Bardwell, Y. Liu, H. Tang, J. B. Webb, S. J. Rolfe, and J. Lapointe, "AlGa_N/Ga_N HFET devices on SiC grown by ammonia-MBE with high f_T and f_{MAX} ", *Electron. Lett.*, vol. 39, no. 6, pp. 564-565, 2003.
- [22] J. B. Webb, H. Tang, J. A. Bardwell, and P. Coleridge, "Growth of high mobility AlGa_N/Ga_N heterostructures by ammonia-molecular beam epitaxy", *Phys. Stat. Sol. A*, vol. 176, no. 1, pp. 243-246, 1999.
- [23] B. Heying, I. Smorchkova, C. Poblenz, C. Elsass, P. Fini, S. P. DenBaars, U. K. Mishra, and J. Speck, "Optimization of the surface morphologies and electron mobilities in Ga_N grown by plasma-assisted molecular beam epitaxy", *Appl. Phys. Lett.*, vol. 77, no. 18, pp. 2885-2887, 2000.
- [24] A. Hierro, A. R. Arehart, B. Heying, M. Hansen, U. K. Mishra, S. P. DenBaars, J. S. Speck, and S. A. Ringel, "Impact of Ga/N flux ratio on trap states in n-Ga_N grown by plasma-assisted molecular-beam epitaxy", *Appl. Phys. Lett.*, vol. 80, no. 5, pp. 805-807, 2002.
- [25] D. S. Katzer, S. C. Binari, D. F. Storm, J. A. Roussos, B. V. Shanabrook, and E. R. Glaser, "MBE growth of AlGa_N/Ga_N HEMTs with high power density", *Electron. Lett.*, vol. 38, no. 25, pp. 1740-1741, 2002.
- [26] C. R. Elsass, T. Mates, B. Heying, C. Poblenz, P. Fini, P. M. Petroff, S. P. DenBaars, and J. S. Speck, "Effects of growth conditions on the incorporation of oxygen in AlGa_N layers grown by plasma assisted molecular beam epitaxy", *Appl. Phys. Lett.*, vol. 77, no. 20, pp. 3167-3169, 2000.
- [27] A. J. Ptak, L. J. Holbert, L. Ting, C. H. Schwartz, M. Moldovan, N. C. Giles, T. H. Myers, P. Van Lierde, C. Tian, R. A. Hockett, S. Mitha, A. E. Wickenden, D. D. Koleske, and R. L. Henry, "Controlled oxygen doping of Ga_N using plasma assisted molecular-beam epitaxy", *Appl. Phys. Lett.*, vol. 79, no. 17, pp. 2740-2742, 2001.
- [28] J. B. Webb, H. Tang, J. A. Bardwell, and P. Coleridge, "Growth of high mobility Ga_N and AlGa_N/Ga_N high electron mobility transistor structures on 4H-SiC by ammonia molecular-beam epitaxy", *Appl. Phys. Lett.*, vol. 78, no. 24, pp. 3845-3847, 2001.
- [29] O. Brandt, R. Muralidharan, P. Waltereit, A. Thamm, A. Trambert, H. von Kiedrowski, and K. H. Ploog, "Critical issues for the growth of high-quality (Al,Ga)_N/Ga_N and Ga_N/(In,Ga)_N heterostructures on SiC(0001) by molecular-beam epitaxy", *Appl. Phys. Lett.*, vol. 75, no. 25, pp. 4019-4021, 1999.
- [30] E. J. Miller, D. M. Schaadt, E. T. Yu, X. L. Sun, L. J. Brillson, P. Waltereit, and J. S. Speck, "Origin and microscopic mechanism for suppression of leakage currents in Schottky contacts to Ga_N grown by molecular-beam epitaxy", *J. Appl. Phys.*, vol. 94, no. 12, pp. 7611-7615, 2003.

- [31] E. J. Miller, E. T. Yu, P. Waltereit, and J. Speck, "Analysis of reverse-bias leakage current mechanisms in GaN grown by molecular-beam epitaxy", *Appl. Phys. Lett.*, vol. 84, no. 4, pp. 535-537, 2004.
- [32] B. S. Simpkins, E. T. Yu, P. Waltereit and J. S. Speck, "Correlated scanning Kelvin probe and conductive atomic force microscopy studies of dislocations in gallium nitride", *J. Appl. Phys.*, vol. 94, no. 3, pp. 1448-1453, 2003.
- [33] A. Minko, V. Hoel, S. Lepilliet, G. Dambrine, J. DeJaeger, Y. Cordier, F. Semond, F. Natali, and J. Massies, "High microwave and noise performance of 0.17- μ m AlGaIn-GaN HEMTs on high-resistivity silicon substrates", *IEEE Electron Dev. Lett.*, vol. 25, no. 4, pp. 167-169, 2004.
- [34] S. Rajan, P. Waltereit, C. Poblenz, S. J. Heikman, D. S. Green, J. S. Speck, and U. K. Mishra, "Power performance of AlGaIn/GaN HEMTs grown on SiC by plasma-assisted MBE", *Electron Dev. Lett.*, vol. 25, pp. 247-289, 2004.
- [35] P. Waltereit, C. Poblenz, S. Rajan, F. Wu, U. K. Mishra, and J. S. Speck, "Structural properties of GaN buffer layers on 4H-SiC (0 0 0 1) grown by plasma-assisted molecular beam epitaxy for high electron mobility transistors", *Japan. J. Appl. Phys.*, vol. 43, pp. L1520-3, 2004.
- [36] A. L. Corrion, C. Poblenz, F. Wu, and J. S. Speck, "Structural and morphological properties of GaN buffer layers grown by ammonia molecular beam epitaxy on SiC substrates for AlGaIn/GaN high electron mobility transistors", *J. Appl. Phys.*, vol. 103, article 093529, 2008.
- [37] Y. Pei, C. Poblenz, A. L. Corrion, R. Chu, L. Shen, J. S. Speck, and U. K. Mishra, "X- and Ka-band power performance of AlGaIn/GaN HEMTs grown by ammonia-MBE", *Electron. Lett.*, vol. 44, pp. 598-599, 2008.
- [38] J. W. Chung, T. Kim, and T. Palacios, "Advanced gate technologies for state-of-the-art f_T in AlGaIn/GaN HEMTs", *IEEE International Electron Devices Meeting*, pp. 30.2.1-4, San Francisco, CA, December 2010.
- [39] R. Vetury, N. Q. Zhang, S. Keller, and U. K. Mishra, "The impact of surface states on the DC and RF characteristics of AlGaIn/GaN HFETs", *IEEE Trans. Electron Dev.*, vol. 48, pp. 560-566, 2001.
- [40] P. C. Chao, M. Y. Kao, K. Nordheden, and A. W. Swanson, "HEMT degradation in hydrogen gas", *IEEE Electron Dev. Lett.*, vol. 15, pp. 151-153, 1994.
- [41] S. J. Pearton, J. C. Zolper, R. J. Shul, and F. Ren, "GaN: Processing, defects, and devices", *J. Appl. Phys.*, vol. 86, pp. 1-78, 1999.

- [42] C. G. Van de Walle and J. Neugebauer, "First-principles calculations for defects and impurities: Applications to III-nitrides", *J. Appl. Phys.*, vol. 95, pp.3851-3879, 2004.
- [43] A. Hierro, S. A. Ringel, M. Hansen, J. S. Speck, U. K. Mishra, and S. P. DenBaars, "Hydrogen passivation of deep levels in n-GaN", *Appl. Phys. Lett.*, vol. 77, pp. 1499-1501, 2000.
- [44] A. R. Arehart, A. Corrión, C. Poblenz, J. S. Speck, U. K. Mishra, and S. A. Ringel, "Deep level optical and thermal spectroscopy of traps in n-GaN grown by ammonia molecular beam epitaxy", *Appl. Phys. Lett.*, vol. 93, pp. 112101-3, 2008.
- [45] T. Roy, Y. S. Puzyrev, B. R. Tuttle, D. M. Fleetwood, R. D. Schrimpf, D. F. Brown, U. K. Mishra, and S. T. Pantelides, "Electrical-stress-induced degradation in AlGaIn/GaN high electron mobility transistors grown under gallium-rich, nitrogen-rich, and ammonia-rich conditions", *Appl. Phys. Lett.*, vol. 96, no. 13, pp. 133503-5, 2010.
- [46] Y. S. Puzyrev, T. Roy, M. Beck, B. R. Tuttle, R. D. Schrimpf, D. M. Fleetwood, and S. T. Pantelides, "Hydrogenation of defects in GaN and hot-electron degradation in high-electron-mobility transistors", vol. 109, pp. 034501-034508, 2011.
- [47] T. Roy, Y. S. Puzyrev, E. X. Zhang, S. DasGupta, S. A. Francis, D. M. Fleetwood, R. D. Schrimpf, U. K. Mishra, J. S. Speck and S. T. Pantelides, "1/f noise in GaN HEMTs grown under Ga-rich, N-rich, and NH₃-rich conditions", *Microelectron. Reliab.*, vol. 51, pp. 212-216, 2011.
- [48] H. Kim, A. Vertiatchikh, R. M. Thompson, V. Tilak, T. R. Prunty, J. R. Shealy, and L. F. Eastman, "Hot electron induced degradation of undoped AlGaIn/GaN HFETs," *Microelectron. Reliab.*, 2003, vol. 43, no. 6, pp. 823-827.
- [49] R. Reuter, T. Breder, U. Auer, S. Van Waasen, M. Agethen, and F. J. Tegude, "On the temperature dependence of the impact ionization in HFET and the corresponding RF- and noise performance", *IEEE Eighth Intl. Conf. on Indium Phosphide and Related Mater.*, pp. 654-657, 1996.
- [50] A. van der Ziel, "Noise in solid state devices and lasers", *Proc. IEEE*, vol. 58, pp. 1178-1206, 1970.
- [51] S. Lee, K. J. Webb, V. Tilak, and L. F. Eastman, "Intrinsic noise equivalent-circuit parameters for AlGaIn/GaN HEMTs", *IEEE Trans. Microwave Theory and Techniques*, vol. 51, pp. 1567-1577, 2003.
- [52] J. Peransin, P. Vignaud, D. Rigaud, and L. K. J. Vandamme, "1/f noise in MODFET's at low drain bias", *IEEE Trans. Electron Dev.*, vol. 37, no. 10, pp. 2250-2253, 1990.
- [53] A. Balandin, "Gate-voltage dependence of low-frequency noise in GaN/AlGaIn heterostructure field-effect transistors", *Electron. Lett.*, vol. 36, no. 10, pp. 912-913, 2000.

- [54] F. N. Hooge, T. G. M. Kleinpenning, and L. K. J. Vandamme, "Experimental studies on $1/f$ noise," *Rep. Prog. Phys.*, vol. 44, pp. 479-532, 1981.
- [55] A. V. Vertiatchikh and L. F. Eastman, "Effect of the surface and barrier defects on the AlGaIn/GaN HEMT low-frequency noise performance", *IEEE Electron Dev. Lett.*, vol. 24, no. 9, pp. 535-539, 2003.
- [56] A. Kalavagunta, M. Silvestri, M. J. Beck, S. K. Dixit, R. D. Schrimpf, R. A. Reed, D. M. Fleetwood, L. Shen, and U. K. Mishra, "Impact of proton irradiation-induced bulk defects on gate-lag in GaN HEMTs," *IEEE Trans. Nucl. Sci.*, vol. 56, no. 6, pp. 3192-3195, 2009.
- [57] T. Roy, Y. S. Puzyrev, E. X. Zhang, D. M. Fleetwood, R. D. Schrimpf and S. T. Pantelides, "Reliability-limiting defects in AlGaIn/GaN HEMTs", *IEEE International Reliability Physics Symposium*, pp. 4E.4.1-4, Monterey, CA, April 2011.
- [58] L. K. J. Vandamme, "Noise as a diagnostic tool for quality and reliability of electronic devices", *IEEE Trans. Electron Dev.*, vol. 41, pp. 2176-2187, 1994.
- [59] M. E. Levinstein, S. L. Rumyantsev, R. Gaska, J. W. Wang, and M. S. Shur, "AlGaIn/GaN high electron mobility field effect transistors with low $1/f$ noise", *Appl. Phys. Lett.*, vol. 73, pp. 1089-91, 1998.
- [60] S. L. Rumyantsev, Y. Deng, E. Borovitskaya, A. Dmitriev, W. Knap, N. Pala, M. S. Shur, M. E. Levinstein, M. Asif Khan, G. Simin, J. Yang, and X. Hu, "Low-frequency noise in GaN/AlGaIn heterostructure field-effect transistors at cryogenic temperatures", *J. Appl. Phys.*, vol. 92, pp. 4726-4730, 2002.
- [61] P. Dutta and P. M. Horn, "Low-frequency fluctuations in solids: $1/f$ noise", *Rev. Mod. Phys.*, vol. 53, pp. 497-516, 1981.
- [62] T. Mattila, A. P. Seitsonen, and R. M. Nieminen, "Large atomic displacements associated with nitrogen antisite in GaN", *Phys. Rev. B*, vol. 54, pp. 1474-1477, 1996.
- [63] T. Roy, E. X. Zhang, Y. S. Puzyrev, X. Shen, D. M. Fleetwood, R. D. Schrimpf, J. S. Speck, U. K. Mishra, and S. T. Pantelides, "Temperature dependence and microscopic origin of low frequency $1/f$ noise in GaN/AlGaIn high electron mobility transistors", submitted to *Appl. Phys. Lett.*
- [64] T. Roy, E. X. Zhang, Y. S. Puzyrev, D. M. Fleetwood, R. D. Schrimpf, B. K. Choi, A. B. Hmelo, and S. T. Pantelides, "Process dependence of proton-induced degradation in GaN HEMTs", *IEEE Trans. Nucl. Sci.*, vol. 57, pp. 3060-3065, 2010.
- [65] D. M. Fleetwood, H. D. Xiong, Z.-Y. Lu, C. J. Nicklaw, J. A. Felix, R. D. Schrimpf, and S. T. Pantelides, "Unified model of hole trapping, $1/f$ noise, and thermally stimulated current in MOS devices", *IEEE Trans. Nucl. Sci.*, vol. 49, pp. 2674-2883, 2002.

- [66] Y. S. Puzyrev, and S. T. Pantelides, unpublished.
- [67] J. H. Scofield, N. Borland, and D. M. Fleetwood, "Temperature-independent switching rates for a random telegraph signal in a silicon metal–oxide–semiconductor field-effect transistor at low temperatures", *Appl. Phys. Lett.*, vol. 76, pp. 3248-3250, 2000.
- [68] M. D. McCluskey, N. M. Johnson, C. G. Van de Walle, D. P. Bour, and M. Kneissl, "Metastability of Oxygen Donors in AlGa_N", *Phys. Rev. Lett.*, vol. 80, pp. 4008-4011, 1998.
- [69] M. B. Weissman, "1/f noise and other slow, non-exponential kinetics in condensed matter", *Rev. Mod. Phys.*, vol. 60, pp. 537-571, 1988.
- [70] M. Chen, Y. F. Zhao, R. D. Schrimpf, J. C. Keay, and K. F. Galloway, "Annealing behavior of a proton irradiated Al_xGa_{1-x}N/GaN high electron mobility transistor grown by MBE," *IEEE Trans. Electron Dev.*, vol. 47, pp. 304–307, Feb. 2000.
- [71] B. D. White, M. Bataiev, L. J. Brillson, B. K. Choi, D. M. Fleetwood, R. D. Schrimpf, S. T. Pantelides, R. W. Dettmer, W. J. Schaff, J. G. Champlain, and U. K. Mishra, "Characterization of 1.8 MeV proton irradiated AlGa_N/Ga_N field-effect transistor structures by nanoscale depth-resolved luminescence spectroscopy," *IEEE Trans. Nucl. Sci.*, vol. 49, pp. 2695–2701, Dec. 2002.
- [72] X. Hu, A. P. Karmarkar, B. Jun, D. M. Fleetwood, R. D. Schrimpf, R. D. Geil, R. A. Weller, B. D. White, M. Bataiev, L. J. Brillson, and U. K. Mishra, "Proton-irradiation effects on AlGa_N/Al/Ga_N high electron mobility transistors," *IEEE Trans. Nucl. Sci.*, vol. 50, pp. 1801–1806, Dec. 2003.
- [73] Y. S. Puzyrev, T. Roy, E. X. Zhang, D. M. Fleetwood, R. D. Schrimpf and S. T. Pantelides, "Radiation-induced defect evolution and electrical degradation of AlGa_N/Ga_N high-electron-mobility transistors", submitted to *IEEE Trans. Nucl. Sci.*
- [74] B. D. White, M. Bataiev, S. H. Goss, X. Hu, A. Karmarkar, D. M. Fleetwood, R. D. Schrimpf, W. J. Schaff, and L. J. Brillson, "Electrical, spectral, and chemical properties of 1.8 MeV proton irradiated Al-Ga_N/Ga_N HEMT structures as a function of proton fluence", *IEEE Trans. Nucl. Sci.*, vol. 50, no. 6, pp. 1934-1941, Dec. 2003.
- [75] A. Kalavagunta, A. Touboul, L. Shen, R. D. Schrimpf, R. A. Reed, D. M. Fleetwood, R. K. Jain, and U. K. Mishra, "Electrostatic mechanisms responsible for device degradation in proton irradiated AlGa_N/Al_N/Ga_N HEMTs," *IEEE Trans. Nucl. Sci.*, vol. 55, no. 4, pt. 1, pp. 2106–2112, Aug. 2008.
- [76] A. van der Ziel, "Flicker noise in electronic devices," in *Advances in Electronics and Electron Physics*, Vol. 49, edited by Martin and Martin (Academic Press, New York, 1979), pp. 225-297.

- [77] J. H. Scofield and D. M. Fleetwood, "Physical basis for nondestructive tests of MOS radiation hardness," *IEEE Trans. Nucl. Sci.*, vol. 38, no. 6, pp. 1567-1577, Dec. 1991.
- [78] M. J. Beck, R. Hatcher, R. D. Schrimpf, D. M. Fleetwood, and S. T. Pantelides, "Quantum mechanical description of displacement damage formation," *IEEE Trans. Nucl. Sci.*, vol. 54, pp. 1906-1912, 2007.
- [79] J. Nord, K. Nordlund, and J. Keinonen, "Molecular dynamics study of damage accumulation in GaN during ion beam irradiation," *Phys. Rev. B*, vol. 68, pp. 184104 1-7, 2003.